Influencia del Océano Índico en la evolución del ENSO

Juan Diego Mantilla Quintero

Universidad Nacional de Colombia
Facultad de Minas - Departamento de Geociencias y Medio Ambiente
Medellín, Colombia
2022

On the role of the Indian Ocean as a precursor of ENSO

Juan Diego Mantilla Quintero

Thesis submitted as partial fulfilment of the requirements towards the degree of:
Master of Science: Engineering in Water Resources.

Director:
Carlos David Hoyos Ortiz PhD

Discipline:
Earth Sciences

Universidad Nacional de Colombia
Facultad de Minas - Departamento de Geociencias y Medio Ambiente
Medellín, Colombia
2022

Como me explicó un amigo arahuaco, Jaison Pérez Villafaña, cuando bajé con él y un grupo de veinte hombres y mujeres de la montaña al mar: "Nosotros no llamamos a la Sierra Nevada el Corazón del Mundo porque sea un capricho nuestro, sino porque los ríos que bajan de las montañas se unen con los demás ríos para refrescar el mar. Cada animal que hay en el bosque, en la montaña, en la tierra, existe en parte gracias al mar. Todo se nutre de todo y ese equilibrio es el que conocemos y respetamos. Todo es parte de un balance perfecto. El aire se vuelve viento, el viento se condensa en nubes, la lluvia cae de las nubes y fluye por la tierra a través de los ríos hacia el mar, donde vuelve a ascender en las alas del viento".

As Jaison Pérez Villafaña, a close Arhuaco friend, explained when I once accompanied him and a party of twenty or more men and women from the mountains to the sea, "We do not call the Sierra Nevada the Heart of the World simply because it occurs to us, but because the rivers that come from the mountains join with all the different rivers to bring cold to the sea. Every animal that lives in the forest, on the mountain, on the earth also lives because of the sea. One feeds on the other, and that balance is the one we know and respect. Everything in balance. The air becomes winds, the wind condenses into clouds, the rain falls from the clouds and runs over the earth through the rivers to the sea, where it arises again, carried by the wind."

— Wade Davis,
Magdalena. Historias de Colombia

Acknowledgments

I would like to acknowledge the enormous help I received in constructing this investigation. First, I wish to thank my advisor, professor Carlos David Hoyos for his support, patience, and guidance. His thoughtful and constructive comments guided me during this long journey and helped me set a life dedicated to science. His classes about atmospheric science caught my attention and curiosity, making me follow this path. I thank him for all the opportunities he gave me; I do not know where I would be if I had not taken his classes.

I am incredibly grateful and humbled by professor Alejandro Jaramillo, a person I contacted online when I had trouble implementing the Wheeler-Kiladis filter. He not only shared with me his implementation of the filter; but also offered himself to discuss my investigation. His thoughtful comments and discussions were critical to completing my thesis over the last few months. I thank him for his sincere concern about my advances in my Master's and for offering me a hand when I needed it. Furthermore, I truly appreciate the valuable time he invested in my investigation.

My most sincere thanks to Sara Jane Pancerella and her family, who always support me. Sara was a blessing in my life who taught me what is truly important, and because of her, I know what *love* really means. She helped me when I wasn't feeling myself during a dark period of my life. She truly has a golden heart, and I will always be in debt to her. Also, the Pancerella family was incredibly kind to me. They made me part of them and made me feel at home when I visited them. In addition, they gave me a laptop that was essential to complete this research after mine was stolen.

I thank all readers and commentators of this thesis in its various drafts and versions for their input, suggestions, and feedback- particularly to professor Alejandro Jaramillo, Jorge Echeverri, Julián Sepúlveda, Juan Sebastián Valbuena, and my work team at SIATA.

I am also grateful to the department professors, especially Oscar Mesa, Janet Barco, Luis Fernando Carvajal, and Mauricio Toro. The guidance given by professor Oscar Mesa was critical for finishing the last chapter of this document. Additionally, I would like to thank Santiago Henao, Santiago Figueroa, and Harold Díaz for their help in setting up the conceptual model used in the last chapter.

I would also like to thank all the friends who came to my rescue whenever chunks of this investigation fell apart and whenever I doubted myself. Mainly to José Lozano, Alejandra and Sebastían Rojas, Oscar Sánchez, Dubán Marín, Katherin Corrales, Isabel Acero, Carlos Valenzuela, Valentina Ramírez, Vanessa Bustamante, Juan Sebastián Valbuena, David Agudelo, and Manuela Velásquez.

I would like to thank the jurors of this thesis, Professors Paul Roundy and Oscar Mesa. Their comments and appreciations were essential to make this thesis more complete.

And, as always, my appreciation to my mother, Adriana Lucía Quintero, who often believes

in me more than I do myself. This thesis is dedicated to her, the bravest person I know.

Resumen

Aunque los aspectos principales que dan lugar a El Niño-Oscilación del Sur (ENSO), el modo dominante de variabilidad climática en la escala de tiempo interanual, se comprenden razonablemente bien, predecir el estado de ENSO antes de la primavera boreal continúa representando un desafío. Investigaciones recientes sugiriere que la variabilidad interanual de la temperature superficial del mar sobre el Océano Índico puede influir en desarrollo del ENSO del año siguiente como también en sus transiciones de fase, representando una posible fuente adicional de predictibilidad. Esta investigación tiene como objetivo analizar la interacción acoplada entre los océanos Índico y Pacífico que podría proporcionar información más allá de la barrera de predictibilidad de primaveral. En primer lugar, se utiliza un enfoque empírico para estudiar la covariabilidad de la temperatura del subsuperficie en los dos océanos para evaluar el papel del Océano Índico como precursor del ENSO. Además, se investigan dos posibles mecanismos acoplados. Luego, evaluamos la representación de las simulaciones históricas del CMIP6 de la covariabilidad entre los dos océanos y comparamos el rendimiento con las métricas compresivas del CLIVAR ENSO. Finalmente, usando un modelo conceptual simple, investigamos las repercusiones del Océano Índico sobre el comportamiento dinámico de ENSO, representado por la adición de un parámetro idealizado del forzamiento de la MJO (Madden-Julian Oscillation) sobre el Pacífico Occidental. Los resultados resaltan el papel del acoplamiento de la subsuperficien entre las dos cuencas para favorer el cambio de fase del ENSO, y respaldan la opinión de que la variabilidad climática del Indo-Pacífico tropical debe estudiarse como un todo en lugar de modos de variabilidad separados.

Palabras clave: El Niño-Oscilación del Sur (ENSO); Interacción entre cuencas; Indo-Pacífico tropical; Dipolo del Océano Índico (IOD); Indian Ocean basin-wide Mode (IOBM); Oscilación de Madden-Julian (MJO); Variabilidad intraestacional (ISV); Variabilidad interanual; CMIP6; Funciones ortogonales empíricas extendidas (EEOF); Caos determinístico.

Abstract

Although the major aspects that give rise to El Niño-Southern Oscillation (ENSO), the dominant mode of climate variability on the interannual time scale, are reasonably well understood, predicting the state of ENSO before the preceding boreal spring has proved to be challenging. Recent investigations suggested that interannual SST variability over the Indian Ocean can influence the following year's ENSO and its phase transition, thus representing a potential additional source of predictability. This research aims to analyze the coupled interaction between the Indian and Pacific oceans that could provide information beyond the spring predictability barrier. Firstly, an empirical approach is used to study the subsurface temperature covariability across the two oceans to assess the role of the Indian Ocean as a precursor of the ENSO. Furthermore, two possible coupling mechanisms are investigated. Then, we assessed the representation of the CMIP6's historical simulation of the subsurface covariability between the two oceans and compared the performance with the compressive CLIVAR ENSO metrics. Finally, using a simple conceptual model, we investigate the repercussions of the Indian Ocean over ENSO's dynamical behavior, represented by the addition of an idealized MJO-forcing parameter over the Western Pacific. Overall, the results highlighted the role of the interbasin subsurface coupling in favoring the ENSO phase transitions and support the view that tropical Indo-Pacific climate variability should be studied as a whole rather than as separated basin modes.

Keywords: El Niño-Southern Oscillation (ENSO); Inter-basin Interaction; Tropical Indo-Pacific; Indian Ocean Dipole (IOD); Indian Ocean basin-wide Mode (IOBM); Madden-Julian Oscillation (MJO); Intraseasonal variability (ISV); Interannual variability; CMIP6; Extended Empirical Orthogonal Function (EEOF); Deterministic Chaos.

Abbreviations

BPF	Band-pass filter
CGCM	Coupled Global Circulation Model
CMIP	Coupled Model Intercomparison Project
DJF	December, January, Februar
DJFMAM	December, January, Februar, March, April, May
EEOF	Extended Empirical Orthogonal Function
ENSO	El Niño-Southern Oscillation
IOBM	Indian Ocean Basin Mode
IOD	Indian Ocean Dipole
ISV	Intraseasonal Variability
JJA	June, July, August
LE	Lyapunov Exponent
LPF	Low-pass filter
MAM	March, April, May
MJO	The Madden-Julian Oscillation
Niño-3.4	Central Pacific region (5°N-5°S, 170°W-120°W)
OLR	Outgoing Longwave Radiation at top of atmosphere
PC	Principal Component
SON	September, October, November
SST	Sea Surface Temperature
SubEIO	Subsurface temperature between 50-150m for the region 10°N-10°S, 80°E-97°E
WEI	Wind Event Index
WWE	Westerly Wind Event
WWV	Warm Water Volume

List of Figures

List of Tables

Contents

1. Introduction

The El Niño-Southern Oscillation (ENSO) is the most prominent mode of climate variability at season to interannual time scales occurring approximately every 2-7 years (McPhaden et al., 2006a). El Niño events are characterized by an anomalous surface warming of the tropical Pacific Ocean and weakening of equatorial trade winds. Meanwhile, the anomalous cooling of the Pacific Ocean and an intensification of the trade winds distinguished La Niña.

The foundations for the understanding of ENSO are grounded on the work of Bjerknes (1969), Wyrtki (1985), and Cane and Zebiak (1985), who set the notion that ENSO originates from an oscillatory coupled ocean-atmosphere instability. For instance, Bjerknes (1969) hypothesized that the El Niño arises through positive feedback between variations in the surface winds and sea surface temperature (SST). Then, Wyrtki (1985) postulated that the El Niño events were the result of the redistribution of the heat content driven by the strengthening of the trade winds in the central Pacific and followed by their sudden collapse. This sequence of wind variations forces a downwelling equatorial Kelvin Wave that propagates to the eastern coast, increasing the SST and prompting a warm ENSO event through Bjerknes' positive feedback. Meanwhile, Cane and Zebiak (1985) created the first coupled ENSO model, which included the above hypothesis. Furthermore, it was the first dynamical model that produced a successful prediction of El Niño (Cane et al., 1986). Overall, all this work shaped the view of ENSO as a coupled ocean-atmosphere phenomenon with its essential elements contained within the tropical Pacific (Zebiak and Cane, 1987) and allowed the following advancements in its theory, modeling, and prediction. Although these theories provide a substantial basis for ENSO understanding, short-time scale processes such as the Westerly Wind Events (WWEs, Harrison and Schopf, 1984; McPhaden et al., 1988; McPhaden, 1992, 1999; Lengaigne et al., 2002) and the Madden-Julian Oscillation (MJO, Madden and Julian, 1971, 1972; Zhang, 2005) have proven to exert an important influence over the ENSO development creating a stochastic component into ENSO variability (Timmermann et al., 2018).

Although ENSO arises in the tropical Pacific, it has a global influence through atmospheric and oceanic teleconnections that affect weather variability worldwide (Yeh et al., 2018, and references therein), leading to droughts, floods, heatwaves, and other extreme weather events across the planet (McPhaden et al., 2006a). For example, the 1997-98 El Niño event, one of the strongest on record, indirectly caused an estimated 23,000 fatalities worldwide (Changnon, 2000). In addition, ENSO also produces an economic toll on countries' economies as energy and non-fuel commodity prices increases in the short term,

although the overall response is considerably heterogeneous for different countries to El Niño shocks (Cashin et al., 2017). Furthermore, the ENSO has also been linked with episodes of human clashes. According to Hsiang et al. (2011), the ENSO may have had a role in 21% of all civil conflicts since 1950. Thus, a skillful ENSO prediction allows decision-makers to anticipate climate anomalies, potentially reducing the societal and economic impacts (Tang et al., 2018).

Nonetheless, ENSO predictions had been limited by an apparent predictability barrier; that is, forecasts produced before the preceding boreal spring, about two months before the onset and nine months before the mature phase of the El Niño event, typically show minimal skill (Webster and Yang, 1992; Webster, 1995; Latif et al., 1998). The spring barrier is phase-locked with the annual cycle and occurs when the ocean-atmosphere coupling is at its frailest state, being more sensitive to random variability. That is, the SST gradient across the Pacific is minimal, and the Walker Circulation is weakest (Webster, 2020).

Despite the ENSO influence being felt around the globe, regions outside the tropical Pacific can, in turn, influence the evolution of ENSO. For example, previous studies indicate that the Indian Ocean and the tropical Atlantic can affect the development of the ENSO through changes in the Walker Circulation and convection center location (Cai et al., 2019, and references therein). In that respect, it has been suggested that interannual SST variability in the Indian Ocean (Clarke and Van Gorder, 2003; Kug and Kang, 2006; Kug et al., 2006b; Ohba and Ueda, 2007; Izumo et al., 2010b, 2014; Luo et al., 2010; Webster and Hoyos, 2010; Okumura et al., 2011; Ohba and Watanabe, 2012; Jourdain et al., 2016; Wieners et al., 2016, 2017; Cai et al., 2019) can influence the development of ENSO and its phase transition, thus representing a potential additional source of predictability.

Another way the Indian Ocean might influence ENSO is by modulating the Intraseasonal Variability (hereafter ISV). Since the 1997-98 strong El Niño event, numerous studies have indicated that high-frequency ocean and atmospheric variability (ISV) play a significant role in ENSO dynamics and predictability (Moore and Kleeman, 1999; Kessler and Kleeman, 2000; Zavala-Garay et al., 2005; Boulanger et al., 2004; McPhaden et al., 2006b; Shi et al., 2009; Wang et al., 2011; Chen et al., 2016). Furthermore, a significant fraction of the ISV over the tropics is controlled by the Madden-Julian Oscillation (MJO, Madden and Julian, 1971, 1972; Zhang, 2005), suggesting a possible bridge between the ocean in the intraseasonal time scale.

In the following document, the influence of the Indian Ocean in the development of ENSO is approached from three individual but complementary studies. First, in Chapter 2 we study the coevolution of the Pacific and the Indian Ocean by analyzing the covariability of the ocean temperature profile in the tropical region. The main goal is to identify linkages between the Indian and Pacific oceans concerning the leading process in the oceans' subsurface variability that can be exploited to improve seasonal climate predictions. We identified two potential mechanisms: an atmospheric bridge and a modulation of the MJO (Madden-Julian Oscillation) related intraseasonal variability over the Indo-Pacific region. Moreover,

both processes may co-occur and influence each other. In Chapter 3, we then analyzed the performances of the state-of-the-art Coupled General Circulation Model (CGCMs) in simulating the subsurface coevolution of the Indian and Pacific oceans. Here, we contrast the historical simulation of the CGCMs with the observational data in representing the leading modes of interannual variability of the subsurface temperature analyzed in the previous chapter. Finally, in Chapter 4, we examine the influence of the MJO over ENSO's irregularity by analyzing the quasi-periodicity route to chaos using a seasonally forced delayed oscillator model for the ENSO. The thesis concludes in Chapter 5 with a summary and discussion of the general results.

2. Leading interannual modes of subsurface climate variability

Abstract

In recent years, it has been suggested that the SST variability over the Indian Ocean modulates the Western Pacific wind variability, which in turn can influence the ENSO phase transition and ENSO's state with lead times up to 14 months, potentially exceeding past the spring predictability barrier. This study analyzes the ocean subsurface temperature profile in the tropical band to assess the role of the Indian Ocean as a precursor of the ENSO. Both a composite analysis and lead-lagged correlation of the subsurface temperature profile indicated an eastward propagating structure from the Indian Ocean into the Wester Pacific previous to the development of an El Niño event. Furthermore, the leading empirical modes of subsurface interannual variability highlight the interbasin interactions' role in the ocean wave dynamics responsible for the ENSO oscillation and phase transition. Finally, we investigate the response of the atmospheric counterpart concerning the leading modes of subsurface interannual variability, seeking a coupled connection that could provide information beyond the spring predictability barrier. We identified two potential mechanisms: the modulation of the zonal wind variability over the Indo-Pacific region and an enhancement of the MJO-induced wind variability over the Western Pacific during the development of the El Niño events. Although the empirical ocean modes are coupled to an atmospheric interaction, they are only relevant for some El Niño events, in particular, the strongest ones (i.e., 1968-69, 1972-73, 1982-83, 1987-88, 1997-98, and 2015-16). Moreover, the mechanisms are not entirely independent from ENSO, they could interact with each other, contributing to the influence of the Indian Ocean over the ENSO. Furthermore, this study coincides with the notion that tropical Indo-Pacific climate variability should be studied as a whole rather than as separated basin modes.

Keywords

El Niño-Southern Oscillation (ENSO); Inter-basin Interaction; Tropical Indo-Pacific; Indian Ocean Dipole (IOD); Indian Ocean basin-wide Mode (IOBM); Madden-Julian Oscillation (MJO); Intraseasonal variability (ISV); Interannual variability; Time-Extended Empirical Orthogonal Function (EEOF).

2.1. Introduction

The El Niño-Southern Oscillation (ENSO) is the strongest dominant mode of interannual variability in the tropical Pacific (Weare et al., 1976; Harrison and Larkin, 1998; Vecchi and Harrison, 2000). Nonetheless, its impacts extend through atmospheric and ocean circulation changes that affect the global climate, land and sea ecosystems, and many countries' economies (Trenberth et al., 1998; Wang et al., 2000; Alexander et al., 2002; McPhaden et al., 2006a; Timmermann et al., 2018). Therefore, a better understanding of the variability and formation of the ENSO is necessary for improving its prediction, considering that its modeling and forecasting remain a challenge (Barnston et al., 2012; Vecchi and Wittenberg, 2010; Guilyardi et al., 2012; Capotondi et al., 2015).

ENSO is a coupled atmosphere-ocean oscillation governed by equatorial oceanic processes and fluctuations in the atmospheric circulation (Bjerknes, 1969). The ENSO swings through a neutral phase between warm (El Niño) and cold (La Niña) extremes. Understanding the mechanisms of the phenomena sets the ground for its predictability. El Niño events develop through positive feedback (Bjerknes' feedback), which allows for the growth of an initial perturbation via atmosphere-ocean interaction. On the other hand, the ocean adjustment due to equatorial wave processes provides a delayed negative feedback (Suarez and Schopf, 1988; Neelin et al., 1998; Jin, 1997a) which is crucial for creating a mechanism for both its termination and oscillatory behavior. Under the recharge-oscillatory framework (i.e. Jin, 1997a), sufficient Pacific Warm Water Volume (WWV, the volume of water warmer than 20°C or equivalently upper ocean heat content) is a robust precursor for the El Niño (Meinen and McPhaden, 2000). Nevertheless, there have been cases when the El Niño failed to develop even though the oceanic conditions were favorable for a warm event (e.g., McPhaden, 2004; Menkes et al., 2014).

Different authors have suggested that the tropical Atlantic and Indian oceans may have an active, rather than a passive (Klein et al., 1999; Alexander et al., 2002; Cai et al., 2019), role in their interaction with ENSO, thus, potentially improving its predictability. For instance, an Atlantic El Niño (Merle, 1980; Zebiak, 1993) favors the development of a Pacific La Niña and vice versa (Dommenget et al., 2006; Wang, 2006; Rodríguez-Fonseca et al., 2009; Losada et al., 2010; Martín-Rey et al., 2012; Ding et al., 2012; Ham et al., 2013; Polo et al., 2015; Cai et al., 2019). Specifically, the Atlantic Mode affects the Walker Circulation by inducing subsidence over the Pacific and the subsequent enhancement of the trade winds (Rodríguez-Fonseca et al., 2009; Losada et al., 2010; Ding et al., 2012; Polo et al., 2015). The latter triggers a coupled response and the development of a La Niña event (Martín-Rey et al., 2012; Ham et al., 2013). Moreover, some authors suggested that the relationship of the Atlantic and the ENSO may undergo a decadal modulation (Martín-Rey et al., 2014) and even a weakening in response to the projected greenhouse warming (Jia et al., 2019).

In the case of the Indian Ocean, it was initially thought to only have a passive response to ENSO (Latif et al., 1995) characterized by the basinwide warming of the ocean (i.e., Indian

Ocean Basin Mode, hereafter IOBM) lagging one season the El Niño mature phase (Klein et al., 1999; Murtugudde and Busalacchi, 1999; Lau and Nath, 2000, 2003; Alexander et al., 2002; Wu and Kirtman, 2004; Ohba and Ueda, 2005; Kug and Kang, 2006; Kug et al., 2006a,b; Xie et al., 2009, 2016; Cai et al., 2019). Additionally, the IOBM evidences an amplitude asymmetry, with a more significant basinwide warming than the corresponding cooling (Hong et al., 2010). Moreover, numerous studies revealed that the Indian Ocean exhibits its own coupled mode of interannual variability (i.e., the Indian Ocean Dipole, hereafter IOD; Saji et al., 1999; Webster et al., 1999; Annamalai et al., 2003; Saji and Yamagata, 2003; Luo et al., 2008; Yuan et al., 2008a), which tends to have a biennial frequency (Saji et al., 1999; Rao et al., 2002; Feng and Meyers, 2003; Behera et al., 2006). A positive IOD event is characterized by the anomalous westward wind in the central Indian Ocean, cold SSTA along the Sumatra-Java coast, and weak warming over the western Indian Ocean. Furthermore, similar to the Pacific Ocean an air-sea coupling enhances the initial anomalies in a positive feedback (Webster et al., 1999). However, Li et al. (2003) reported fundamental differences in the coupled interaction between the Indian and the Pacific Oceans.

In addition, it has been suggested that ENSO can trigger IOD events by creating favorable circulation conditions over the Indian Ocean (Gualdi et al., 2003; Shinoda et al., 2004), or by modulating the convection center and the Walker circulation (Ueda and Matsumoto, 2000; Annamalai et al., 2003; Fischer et al., 2005). As a consequence, positive IOD tends to co-occur with El Niño events, and negative IOD with La Niña (Baquero-Bernal et al., 2002; Annamalai et al., 2003; Li et al., 2003; Ashok et al., 2003; Yamagata et al., 2004; Annamalai et al., 2005; Yu and Lau, 2005; Fischer et al., 2005; Bracco et al., 2005; Behera et al., 2006; Yuan et al., 2008b; Luo et al., 2010). Moreover, different studies indicate that ENSO affects the IOD variability (Alexander et al., 2002; Zhang et al., 2015; Dong and McPhaden, 2017) likewise its periodicity, intensity, and structure (Behera et al., 2006). Nevertheless, decadal variability in the relationship between IOD and ENSO has been reported, with multiple periods when the IOD-ENSO connection is significantly degraded (i.e., Ashok et al., 2003; Tozuka et al., 2007; Santoso et al., 2012; Izumo et al., 2014; Krishnaswamy et al., 2015; Ham et al., 2017; Nidheesh et al., 2019).

In contrast, different studies suggested that the Indian Ocean could modulate ENSO itself. For example, the IOBM affects the ENSO by modulating the Western Pacific wind anomalies favoring its phase transition (Kug and Kang, 2006; Kug et al., 2006b; Ohba and Ueda, 2007; Okumura et al., 2011). An IOB warming, associated with the mature phase of El Niño events, hastens El Niño's demise. The IOB warming induces enhanced convection over the Indian Ocean, which in turn reinforces an anomalous anticyclone circulation over the northwest Pacific and westward wind anomalies over the equatorial Western Pacific, leading to the rapid termination of El Niño and promoting its subsequent transition to La Niña via wind-forced upwelling Kelvin waves (Kug and Kang, 2006; Kug et al., 2006b,a; Cai et al., 2019). Moreover, because of the asymmetric effect of El Niño over SST and associated deep convection anomalies over the Indo-Pacific region compared with La Niña,

there is also an asymmetry in the IOBM contribution to the ENSO demise. This explains why the more significant anomalies associated with an IOB warming have a more prominent influence over the Western Pacific wind variability than an IOB cooling. Consequently, a warming of the IOB is more effective in influencing the termination of El Niño than the opposite case (Ohba and Ueda, 2007; Okumura and Deser, 2010; Cai et al., 2019). Moreover, the asymmetric IOBM-ENSO feedback could potentially contribute to the more systematic phase transitions from El Niño to La Niña and a shorter duration of El Niño (Ohba and Ueda, 2009; Okumura et al., 2011; Ohba and Watanabe, 2012).

On the contrary, several studies argued that the IOD could affect either the simultaneous or the following year ENSO evolution (e.g., Clarke and Van Gorder, 2003; Kug and Kang, 2006; Izumo et al., 2010b, 2014; Webster and Hoyos, 2010; Luo et al., 2010; Annamalai et al., 2010; Yuan et al., 2011, 2013). For instance, positive IOD events that co-occur with El Niño tend to reinforce the warm ENSO phase by inducing anomalous westerly winds in the Western Pacific (Luo et al., 2010; Annamalai et al., 2010). The authors indicated that the suppressed convective activity over a cold eastern Indian Ocean induces westerlies over the Western Pacific, thus strengthening the El Niño. In addition, due to the tendency for IOD to lead ENSO events by 14 months, some authors suggested that the IOD can influence the following year's ENSO (Clarke and Van Gorder, 2003; Izumo et al., 2010b, 2014; Jourdain et al., 2016). However, Stuecker et al. (2017) points out that the lead correlation is just the result of the IOD being a passive response to ENSO and its biennial tendency.

The effect of the IOD on influencing the ENSO relies on an atmospheric bridge, where the Indian Ocean affects the wind variability over the Western Pacific. Some studies (Izumo et al., 2010b, 2014, 2016; Jourdain et al., 2016) propose that during a positive IOD which tends to co-occur with El Niño, a cold eastern Indian Ocean pole induces westerly wind anomalies over the Western Pacific. Then, during the quick demise of the IOD in boreal winter, the sudden wind relaxation over the Western Pacific forces an upwelling Kelvin wave that promotes the rapid transition to La Niña (Izumo et al., 2016). Furthermore, Jourdain et al. (2016), examing both observations and CMIP5 models, concluded that the tendency of positive IOD events to lead to La Niña events by 14 months tends to be more significant than the opposite case. However, as pointed out by Jourdain et al. (2016), the tendency of El Niño to induce a positive IOD and its subsequent transition to La Niña the following year raises uncertainties regarding the causality effect of the IOD-ENSO relationship.

On the contrary, other studies (Izumo et al., 2010b; Wieners et al., 2017; Saji et al., 2018) suggested that a warm eastern Indian Ocean induces an increased convective response that accelerates the Walker circulation in boreal fall; the enhanced easterly wind anomalies over the Western Pacific favor the built-up of heat content anomalies over the Warm Pool promoting an El Niño event the following year (Picaut et al., 1997). Independently of which case is correct, the sudden demise of the IOD eastern pole in boreal winter induces a fast wind change over the Pacific that forces an oceanic response over the Western Pacific and triggers an ENSO event (Izumo et al., 2016).

Altogether, the previous investigations state that the interannual SST variability over the Indian Ocean (IOBM and/or the IOD) favors the ENSO phase transitions, hence strengthening ENSO's biennial tendency (Kug and Kang, 2006; Izumo et al., 2010b, 2014; Ha et al., 2017). Furthermore, as pointed out by Kug et al. (2020), the IOBM, which co-occurs almost systematically with ENSO, can be interpreted as an integral part of the ENSO cycle favoring its turnabout; meanwhile, the IOD, in some degree independent from ENSO, could represent a potential additional source of predictability.

Complementary, Yuan et al. (2011, 2013) suggested that the IOD could influence the interannual variability of the Pacific Ocean through the Indonesian Throughflow (ITF), representing a more significant teleconnection between the eastern Indian and Pacific Oceans than the atmospheric bridge. The authors demonstrated that interannual Kelvin waves that originated over the eastern Indian Ocean could penetrate the Pacific Ocean through the Indonesian Seas. Nevertheless, some studies show that the oceanic bridge has a minimal influence in contrast with the atmospheric bridge (Clarke, 1991; Kajtar et al., 2015; Izumo et al., 2016).

Another way the Indian Ocean might influence ENSO is by modulating the Intraseasonal Variability (hereafter ISV). Since the 1997-98 strong El Niño event, numerous studies have indicated that high-frequency ocean and atmospheric variability (ISV) play a significant role in ENSO dynamics and predictability (Moore and Kleeman, 1999; Kessler and Kleeman, 2000; Zavala-Garay et al., 2005; Boulanger et al., 2004; McPhaden et al., 2006b; Shi et al., 2009; Wang et al., 2011; Chen et al., 2016). A part of this high-frequency atmospheric variability occurs as Westerly Wind Events (hereafter, WWE), zonal wind anomalies over the western and central Pacific. WWEs are known for exerting an influence over the ENSO by directly exciting oceanic Kelvin waves over the western and central Pacific that triggers or accelerates the onset of El Niño (Harrison and Schopf, 1984; McPhaden et al., 1988; McPhaden, 1992, 1999; Lengaigne et al., 2002), and by maintaining El Niño conditions when WWEs are positioned over the eastern Pacific (Seiki and Takayabu, 2007).

Furthermore, a significant fraction of the ISV over the tropics is controlled by the Madden-Julian Oscillation (MJO, Madden and Julian, 1971, 1972; Zhang, 2005). The MJO can be broadly defined as the eastward-propagating perturbations of tropical convection in the 20–90 days range, making it a serious candidate for the modulation of WWEs (Seiki and Takayabu, 2007; Puy et al., 2016). During the MJO convective phase, anomalous convective activity develops over the Indian Ocean and propagates eastward, producing WWEs over the western to central Pacific (Kessler et al., 1995; Kessler and Kleeman, 2000; Zhang, 2005; McPhaden et al., 2006b). Moreover, MJO-related WWEs have a significant oceanic response because the wind events are spatially and temporally coherent (Kessler et al., 1995; Shinoda and Hendon, 2001; Zhang and Gottschalck, 2002).

The Modulation of the MJO by the IOD has been reported in observation and model outputs (Wilson et al., 2013; Benedict et al., 2015). The strengthening of the MJO during a negative IOD and a weakening accompanying a positive IOD has been related to the MJO

sensitivity to local low-level moisture (Wilson et al., 2013), IOD-SST patterns (Yuan et al., 2014), and low-level zonal westerlies (Inness et al., 2003; Zhang et al., 2006). During a negative IOD event, the positive SSTA over the easter Indian Ocean and the low-level westerly wind anomalies facilitate the development and eastward propagation of the MJO over the Indian Ocean (Izumo et al., 2010a; Wilson et al., 2013; Seiki et al., 2016). Furthermore, during a negative IOD event, the low-frequency (55-100 days) variability of the boreal winter MJO signal is enhanced in both the atmospheric convection and oceanic response, with a further eastward propagation of the signal; thus, having a potentially more substantial impact over the Western Pacific (Izumo et al., 2010a). In addition, Wieners et al. (2016) suggested that cold SSTA over the western Indian Ocean during boreal summer might enhance the intraseasonal wind variability over the Western Pacific Ocean during the following spring, which they partly attributed to the MJO.

Overall, the studies discussed above suggest a two-way interaction between the Pacific and the Indian Ocean at the interannual and intraseasonal timescales; however, most have focused on the potential influence of the Indian Ocean's SST variability on ENSO. The main goal of this paper is to shed additional light by analyzing the spatio-temporal covariability of the tropical subsurface temperature between the two oceans to assess the potential role of the Indian Ocean as a precursor of the ENSO and its phase transition. To achieve this goal, we use an empirical technique that is able to detect propagating structures between the subsurface of the oceans at interannual timescales. Then, we analyzed two potential mechanisms in which the Indian Ocean may influence ENSO related to the leading process in the oceans' subsurface variability. The remainder of this chapter is organized as follows. Section 2.2 summarized the data set and methods used. Section 2.3 analyzes the leading interannual modes of variability of the tropical subsurface temperature and describes the spatio-temporal evolution of the atmosphere before the development of the major El Niño events. Two mechanisms are discussed in which the Indian Ocean influences ENSO: an atmospheric bridge and a modulation of the MJO-related intraseasonal variability over the Indo-Pacific region. We conclude in Section 2.4, with a brief summary and discussion of the results.

2.2. Datasets and methods

For this study, we made use of monthly data of SST, subsurface ocean temperature, the zonal and meridional wind components, and geopotential height at different pressure levels. Monthly data of the subsurface temperature of the ocean, on 1°x 1°grid from the period of 1958-2019 was obtained from the European Center for Medium-Range Weather Forecast (ECMWF) ocean reanalysis data (ORAS5; Zuo et al., 2019). The NOAA Extended Reconstructed monthly Sea Surface Temperature (SST V5; Huang et al., 2017) with a resolution of 2° is also used with the same temporal coverage. Moreover, the atmospheric component, with 2.5° resolution, was collected from the NCEP/NCAR Reanalysis 1 (Kalnay et al., 1996)

Variable	Source	**Horizontal resolution**	Temporal resolution	Time coverage	Reference
Subsurface Temperature	ORAS-5	1°x1°	monthly	1958-2020	Zuo et al. (2019)
Winds	NCEP/NCAR Reanalysis 1	2.5°x2.5°	monthly	1958-2020	Kalnay et al. (1996)
SST	NOAA Extended Reconstructed SST-V5	2°x2°	monthly	1854-2020	Huang et al. (2017)
Subsurface Temperature	CMEMS GLORYS Ocean Reanalysis (GLORYS2V4)	0.25°x0.25°	daily	1993-2019	Lellouche et al. (2013)
10m zonal winds	ERA5	0.25°x0.25°	daily	1979-2020	Hersbach et al. (2019)
OLR	NOAA OLR	2.5°x2.5°	daily	1979-2020	Liebmann (1996)

Table **2-1**.: Summary of the data sets used in Chapter 2.

for the same period. The NOAA's Oceanic Niño Index (ONI) was used to define El Niño events, which is based on variations in 3-month running means of SSTs in a central Pacific region defined as Niño-3.4 (5°N-5°S, 120-170°W) based on centered 30-year base periods updated every five years. If the ONI remains larger than 0.5°C for a minimum of 5 consecutive months, an El Niño event is said to occur.

To evaluate the possible influence of the Indian Ocean on the development of El Niño events in the intraseasonal time scale, we analyzed daily data of surface winds, SST, OLR, and ocean subsurface temperature. The 10m zonal winds with a horizontal resolution of 0.25° are taken from the ERA-5 reanalysis (Hersbach et al., 2019), which spans from January 1979 to December 2020. The daily outgoing long-wave radiation (OLR) with a horizontal resolution of 2.5° is taken from NOAA (Liebmann, 1996) for the period 1979-2020. Finally, the subsurface ocean temperatures are taken from the Copernicus Marine Environment Monitoring Service (CMEMS) Global Ocean Physics Reanalysis (GLORYS2 version 4 (Garric et al., 2017)) from January 1993 to December 2015. GLORYS2V4 has a horizontal resolution of 1/4° and 75 levels depth. The GLORYS2V4's 20°C isotherm depth is designed as the depth of the thermocline (henceforth referred to as Z20).

Several authors have indicated that MJO on its eastward propagation over the Western Pacific gives rise to westerly wind events (WWEs, Kessler and Kleeman, 2000), which remotely acts to warm the eastern Pacific through the propagation of downwelling Kelvin Waves (Kessler et al., 1995). Different criteria had been used to define the WWEs (Harrison and Vecchi, 1997; Seiki and Takayabu, 2007; Chiodi et al., 2014; Puy et al., 2016; Liang and Fedorov, 2021) based on the zonal extension, duration, and magnitude of the wind event. The WWEs are here defined as 3°N-3°S average intraseasonal (20-90 days) 10m zonal wind anomalies above 2 m/s with a zonal extent of at least 10° during not less than 5 days. Following Puy et al. (2016) and Liang and Fedorov (2021), the strength of the WWE is characterized by the space-time integration of the zonal wind anomalies over the wind event patch denoted as "wind event index" (WEI, Puy et al., 2016) as in Equation 2-1. The central date day_0 for each event is computed using a weighted average as in Equation 2-2. The central location lon_0 of the WWE on day_0 is computed using Equation 2-3, where lon_0

denote the longitudes of the wind patch.

$$WEI = \int_{lon} \int_{time} U_{wind}(x,t)dxdt \tag{2-1}$$

$$day_0 = \frac{\int_{lon} \int_{t} U_{wind}(x,t)day(t)dxdt}{\int_{lon} \int_{time} U_{wind}(x,t)dxdt} \tag{2-2}$$

$$lon_0 = \frac{\int_{lon} U_{wind}(x,day_0)lon(x)dxdt}{\int_{lon} U_{wind}(x,day_0)dx} \tag{2-3}$$

As in Wheeler and Kiladis (1999), the MJO signal is isolated from the daily OLR as the space-time filtering of the eastward propagating component with zonal wave numbers 1-5 and periods of 20-90 days. In the filtered data, negative OLR anomalies correspond to the convective phase of the MJO; meanwhile, positive anomalies characterized the suppressed MJO's phase.

2.3. Results and discussion

We used a composite analysis technique to study the evolution of the strongest El Niño events, defined as the positive peaks during which ONI Index exceeds one standard deviation (i.e., 1963-64, 1965-66, 1968-69, 1972-73, 1982-83, 1986-87, 1987-88, 1991-92, 1994-95, 1997-98, 2002-03, 2006-07, 2009-10 and 2015-16). Figure **2-1** portrays the simultaneous evolution of the surface and subsurface temperature anomalies 36 months before the peak of the selected events. A 3 to 7 year band-pass filter (BPF) was applied to isolate the interannual variability. The mean evolution of the most intense El Niño events shows that positive anomalies build up over the subsurface of the Indo-Pacific Warm Pool region 36 months before the ENSO's peak (Figure **2-1**A). This condition is coherent to a recharged state of the tropical Pacific in the oscillatory theory (Jin, 1997a), where positive anomalies pile up on the western region before an El Niño event. The subsequent decaying phase of La Niña like conditions (Figure **2-1**B) is associated with thermocline variability, which is produced by an eastward-propagating downwelling Kelvin wave (Figure **2-1**C-E) that starts the onset of the El Niño event (Godfrey, 1975; Wyrtki, 1975). The warming of the eastern Pacific Ocean (Figure **2-1**E) triggers Bjerknes' feedback (Bjerknes, 1969), enhancing the coupled ocean-atmosphere instability responsible for El Niño growth.

Moreover, the evolution of the Indian Ocean shows warm anomalies located in the central region between 50 m and 300 m depth, 36 months before the peak of the El Niño events (Figure **2-1**A). The progression of the tropical Indian Ocean during the following year (Figure **2-1** B-C) exposes the role of Rossby waves in the formation of the surface dipole (Webster

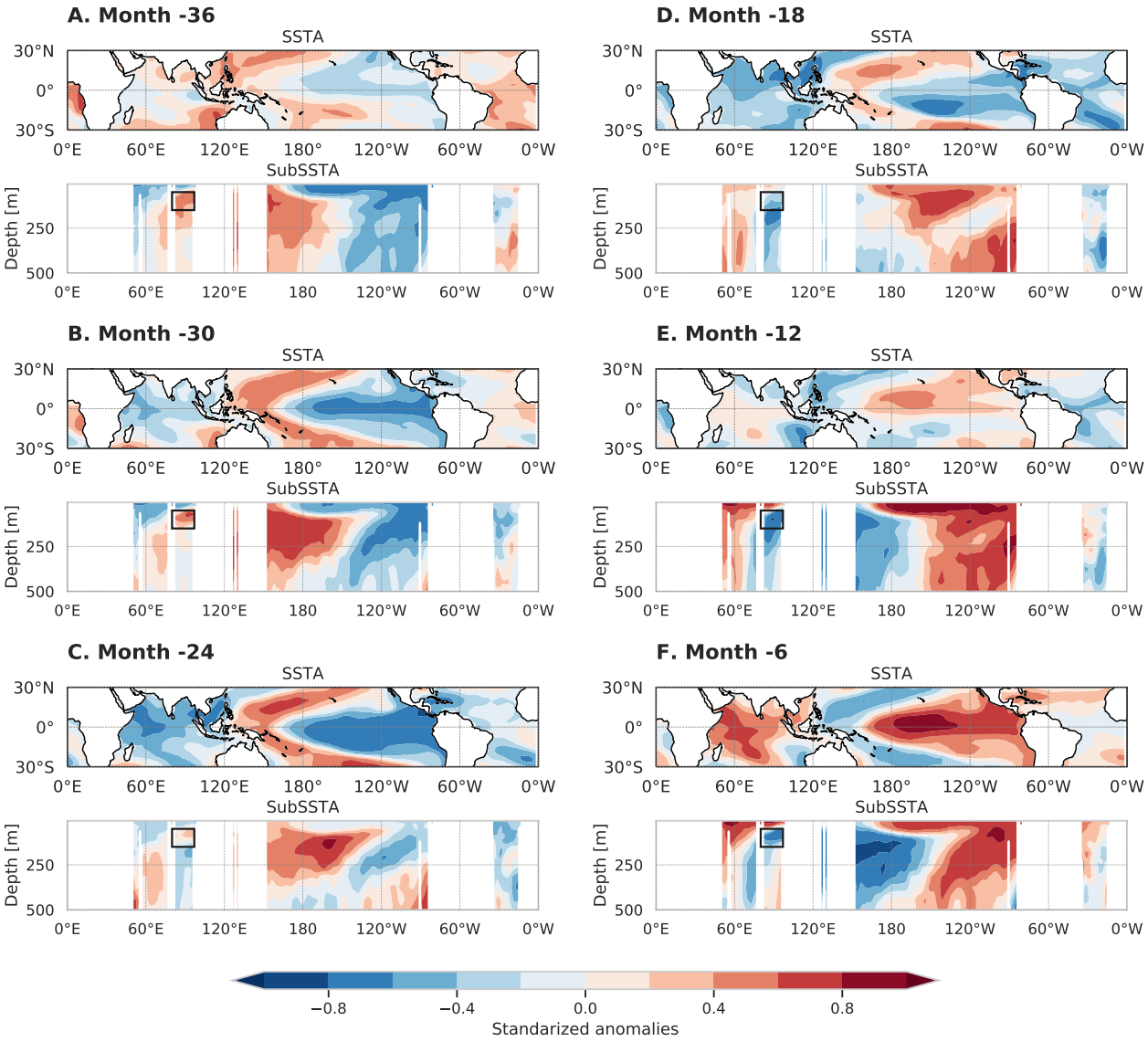

Figure **2-1**.: Time evolution of the composite SST(top) and subsurface temperature anomalies (bottom) from month 36 to month 0 before the peak of the strongest El Niño events (i.e., 1963-64, 1965-66, 1968-69, 1972-73, 1982-83, 1986-87, 1987-88, 1991-92, 1994-95, 1997-98, 2002-03, 2006-07, 2009-10 and 2015-16). In black is the eastern Indian Ocean region (80°E - 97°E, 50m - 150m depth) that is suggested to be leading the warm of the Western Pacific and the subsequent propagation of the downwelling Kelvin wave throughout the Pacific Ocean.

et al., 1999; Murtugudde et al., 2000; Xie et al., 2002; Rao et al., 2002; Feng and Meyers, 2003; Yamagata et al., 2004; Rao and Behera, 2005). In particular, we noted the upward propagation (surge) of positive temperature anomalies over the eastern Indian Ocean (80°E - 97°E, 50m - 150m depth) and its subsequent westward displacement through the subsurface (Figure **2-1** B-C). Figure **2-1**D shows that in the interannual time scale, the development of the Indian Ocean Dipole first occurs on the subsurface of the ocean before its manifests itself on the surface around 6 to 12 months later (Figure **2-1** E-F), in agreement with the finds of Horii et al. (2008). A dipole structure is the dominant pattern of the subsurface tropical Indian Ocean which is controlled by ocean-wave dynamics and forced by zonal winds in the equatorial region (Rao et al., 2002; Rao and Behera, 2005; Feng and Meyers, 2003; Shinoda et al., 2004; Yamagata et al., 2004; Zhao and Nigam, 2015).

Previous studies had identified the eastern pole of the Indian Ocean as a region crucial for the initiation (Annamalai et al., 2003) and termination of the IOD (Rao and Yamagata, 2004), as well as a region that influences the wind variability over the Western Pacific (Izumo et al., 2010b, 2014, 2016; Jourdain et al., 2016; Wieners et al., 2017). In Figure **2-1**, it is noticed that the eastern Indian Ocean region develops positive anomalies before anomalies of the same sign build up in the western of the Pacific Ocean. This suggests that the anomalous warmth of the eastern Indian Ocean leads to the accumulation of heat content anomalies over the Western Pacific Ocean and the subsequent propagation of the downwelling Kelvin wave through the Pacific Ocean. Coherently, earlier investigations (Izumo et al., 2010b; Wieners et al., 2017; Saji et al., 2018) indicated that a warm eastern Indian Ocean (or a cold western Indian Ocean; Wieners et al., 2016) leads the development of an El Niño event by 15 months due to an increased convective response that accelerates the Walker circulation in boreal fall. The enhanced easterly wind anomalies over the Western Pacific favor the built-up of heat content anomalies over the Warm Pool promoting an El Niño event the following year (Picaut et al., 1997). Consequently, to show a close link between the eastern Indian Ocean subsurface signal and the development of ENSO, we calculated an index (hereafter referred to as SubEIO) by averaging the interannual anomalies of the subsurface temperature between 50 and 150 m depth for the region comprehended between 80°E-97°E and 10°N-10°S.

Figure **2-2** shows the lagged correlations maps between the subsurface temperature anomalies of SubEIO index and the surface and subsurface temperature anomalies of the tropical band. Overall, Figure **2-2** highlights the influence of interannual subsurface variations on SST over the Indian Ocean; notice that the correlations are stronger near the equator. The resulting correlation maps illustrate a similar spatiotemporal pattern to the composite evolution of the strongest El Niño events. During the first 6 months, the SubEIO index is highly correlated with the Indio-Pacific Warm Pool region in the surface and subsurface temperature. In contrast, a significant negative correlation is found in the Western Indian and Eastern Pacific oceans. Between 6 and 12 months, there is a transition phase where on the first 150 meters depth, where positive correlations are concentrated in the eastern Indian

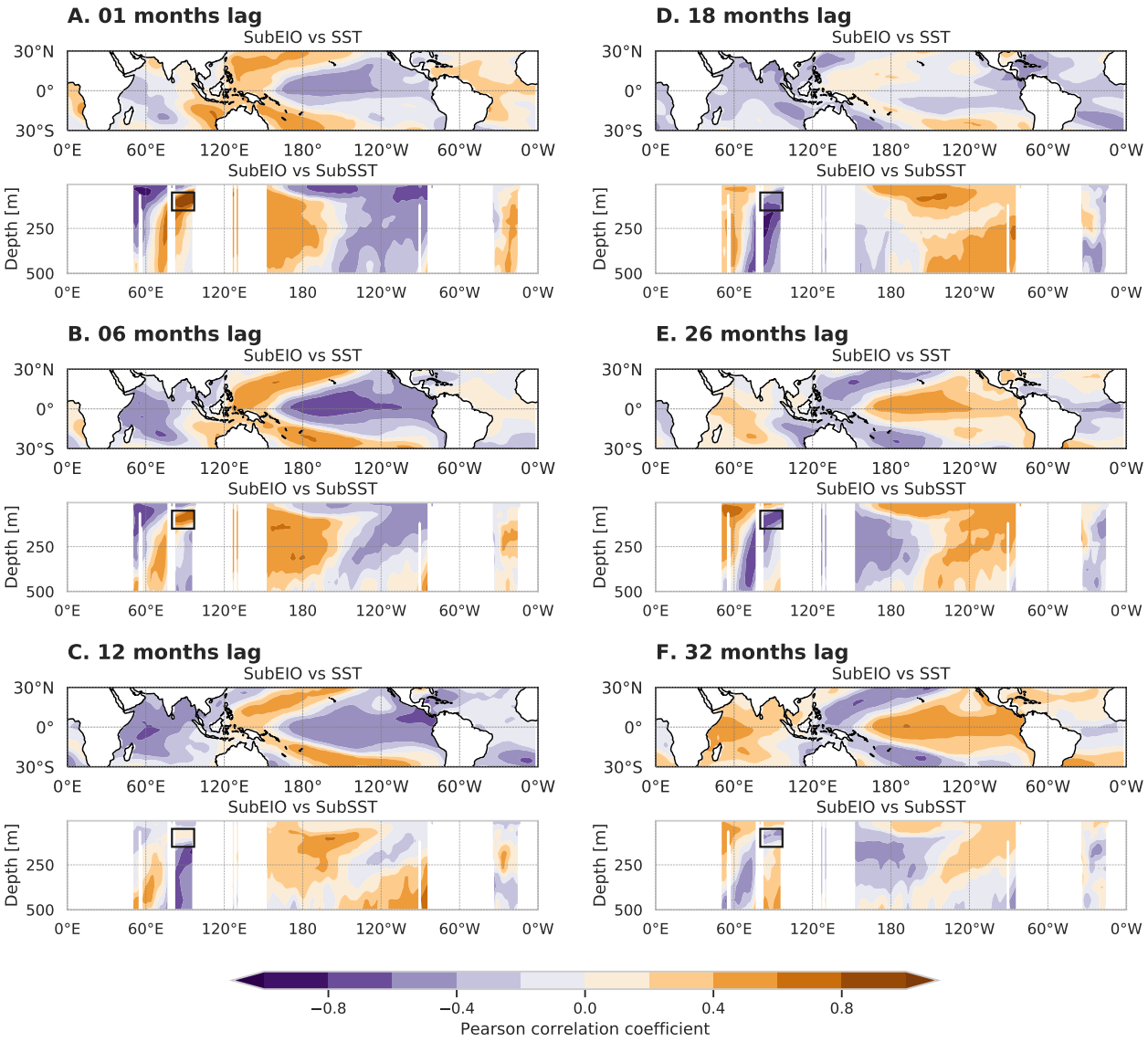

Figure **2-2**.: Lagged correlation maps between the subsurface time series anomalies of the region selected within the eastern Indian Ocean (90°E - 100°E, 50m - 150m depth) and the surface and surface anomalies of the tropical band. The results showed a similar spatiotemporal structure to the composite evolution of the strongest El Niño events, suggesting a typical pattern in the development of both phases of the ENSO events.

Ocean. Then, the positive correlations migrate westward at greater depths, and negative correlations emerge over the eastern boundary. This phenomenon suggests the interaction of Rossby waves and points out the influence of ocean dynamics in the interannual variability of the tropical Indian Ocean (McCreary, 1976; Feng et al., 2001; Xie et al., 2002; Rao et al., 2002; Yamagata et al., 2004; Rao and Behera, 2005). In contrast, a negative basin-wide correlation pattern appears over the surface of the Indian Ocean, which is coherent with the basin-wide response of the Indian Ocean lagging one season the ENSO's mature phase (Klein et al., 1999; Webster et al., 1999; Saji et al., 1999; Murtugudde and Busalacchi, 1999; Venzke et al., 2000; Xie et al., 2002; Luo et al., 2010; N. H. Saji, 2018).

Significant positive correlations over the Western Pacific Ocean reach depths up to 400 meters; thus, indicating the storing of heat content in the equatorial upper ocean to precondition an El Niño event in the following months (Jin, 1997a). In the coming months (12-20 month lag), the eastward displacement of the positive correlation exposes the role of a Kelvin wave in developing an ENSO event (Godfrey, 1975; Wyrtki, 1975). Meanwhile, the Indian Ocean evolves into a dipole structure for both the surface and subsurface temperature, which is consistent with the tendency of co-occurrence of IOD and ENSO events (Baquero-Bernal et al., 2002; Annamalai et al., 2003; Li et al., 2003; Ashok et al., 2003; Saji and Yamagata, 2003; Yamagata et al., 2004; Annamalai et al., 2005; Yu and Lau, 2005; Fischer et al., 2005; Bracco et al., 2005; Behera et al., 2006; Yuan et al., 2008b; Luo et al., 2010).

Finally, as the positive correlation, through a Kelvin wave, reaches the Pacific Ocean's eastern boundary, the opposite coast is charged with negative correlations that firstly emerged over the eastern Indian Ocean. The highest positive correlations between the SubEIO region and the eastern Pacific Ocean occurred around 26–28 months for both the surface and the subsurface temperature. The previous results suggest that a signal that is first developed in the subsurface of the eastern Indian Ocean gets amplified over the Western Pacific at interannual time scales. Thus, the co-evolution of the Indian Ocean and the Pacific Ocean in the interannual time scale suggests an empirical interaction between the oceans, where an atmospheric (Clarke and Van Gorder, 2003; Izumo et al., 2010b, 2014, 2016; Wieners et al., 2016, 2017; Jourdain et al., 2016; Wang et al., 2019) and ocean (Meyers, 1996; Yuan et al., 2011, 2013) bridge could be interplaying.

2.3.1 Leading subsurface interannual variability modes

Because of the suggested co-variability between the oceans, it is meaningful to diagnose the dominant pattern of interannual variability by using the time-extended empirical orthogonal function technique (EEOF; Weare and Nasstrom, 1982). The EEOF analysis is based on the spatial and temporal covariance matrix of the ocean's 60-year monthly tropical subsurface temperature averaged between 10°N and 10°S with a 28-month sequence lag. The longitude–depth domain used for the analysis is the tropical band from 5m to 315m depth below the surface. The data were detrended, and a band-pass filter (BPF) between 3-7 years was

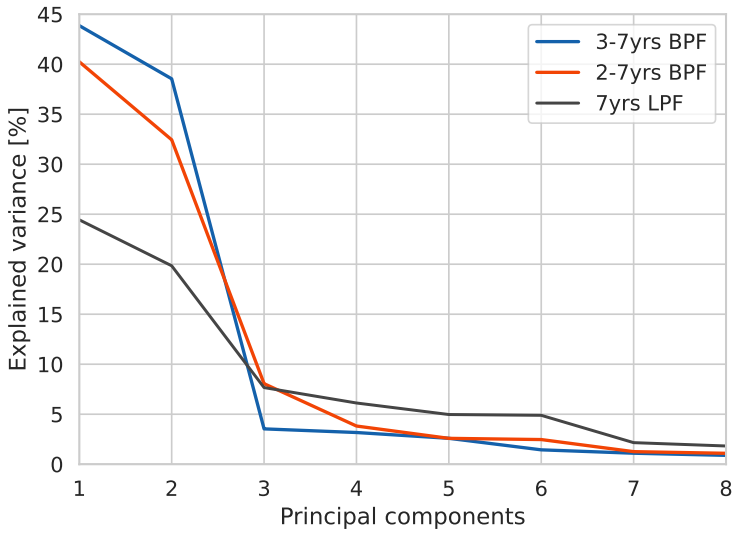

Figure **2-3**.: Explained variance by the principal components according to the time filter used: 3-7 years band-pass filter (BPF) in blue, 2-7 years band-pass filter (BPF) in orange, and 7 years low-pass filter (LPF) in grey.

applied to the longitudinal average cross-section between 10°N and 10°S. Previously, Wang et al. (2019) used a similar technique to analyze the subsurface covariability between the Indian and Pacific oceans in both observational data and coupled global climate model simulations. Figure **2-4** and **2-5** show the two most important extended EOF's spatial patterns, which together explain 82.40% of the variance (Figure **2-3**). The large explained variance is indicative of the influence of the long timescale for the phenomena.

To compare the significance of the filter band used, we performed the same analysis using a 2-7 year band-pass filter (BPF) and a 7 years low-pass filter (LPF). When comparing the result obtained by the 2-7 and 3-7 years BPF (Figure **2-3**), the variance explained by the first couple of principal components is very similar and well separated from the other modes, 72.68% compared with the 82.40% respectively. However, when the 7 years LPB was used, the first couple of modes only explained the 44.28 % of the variance. Therefore, given the 3-7 year BPF maximizes the explained variance of the first mode pair, it was chosen for the analysis. In addition, the time evolution of the first couple of EEOFs is not altered when using the different temporal filters as a similar structures were obtained, varying only in the magnitude of the anomalies as seen in the Section A.1.

Figure **2-4** displays the time evolution of the first EEOF mode, which accounts for 43.86% of the variance of the data. To understand the development of the phenomena, we will consider that the positive magnitudes plotted on Figure **2-4** and **2-5** represent warm temperature anomalies, and the negative values represent anomalies of opposite sign. Therefore the time sequence of the EEOF1 over the Pacific Ocean captures an eastward propagating Kelvin wave (8-20-month lag) that contributes to the demise of the prevailing El Niño conditions

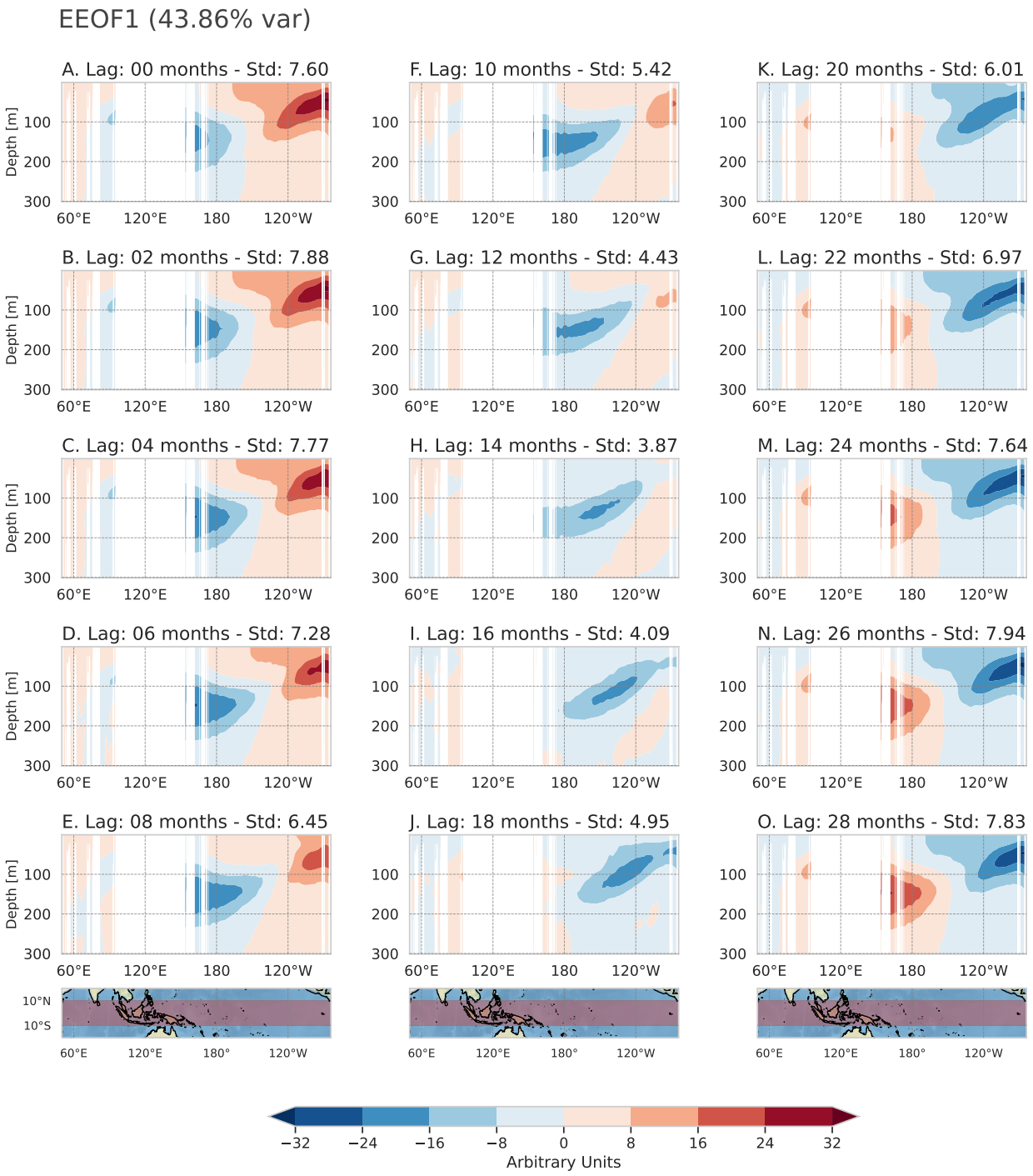

Figure **2-4**.: The spatial pattern of the first mode of the subsurface temperature EEOF from month 0 to month 28. Spatial standard deviation (σ_{xy}) of each field is given on the upper-right corner. Dimensionless units.

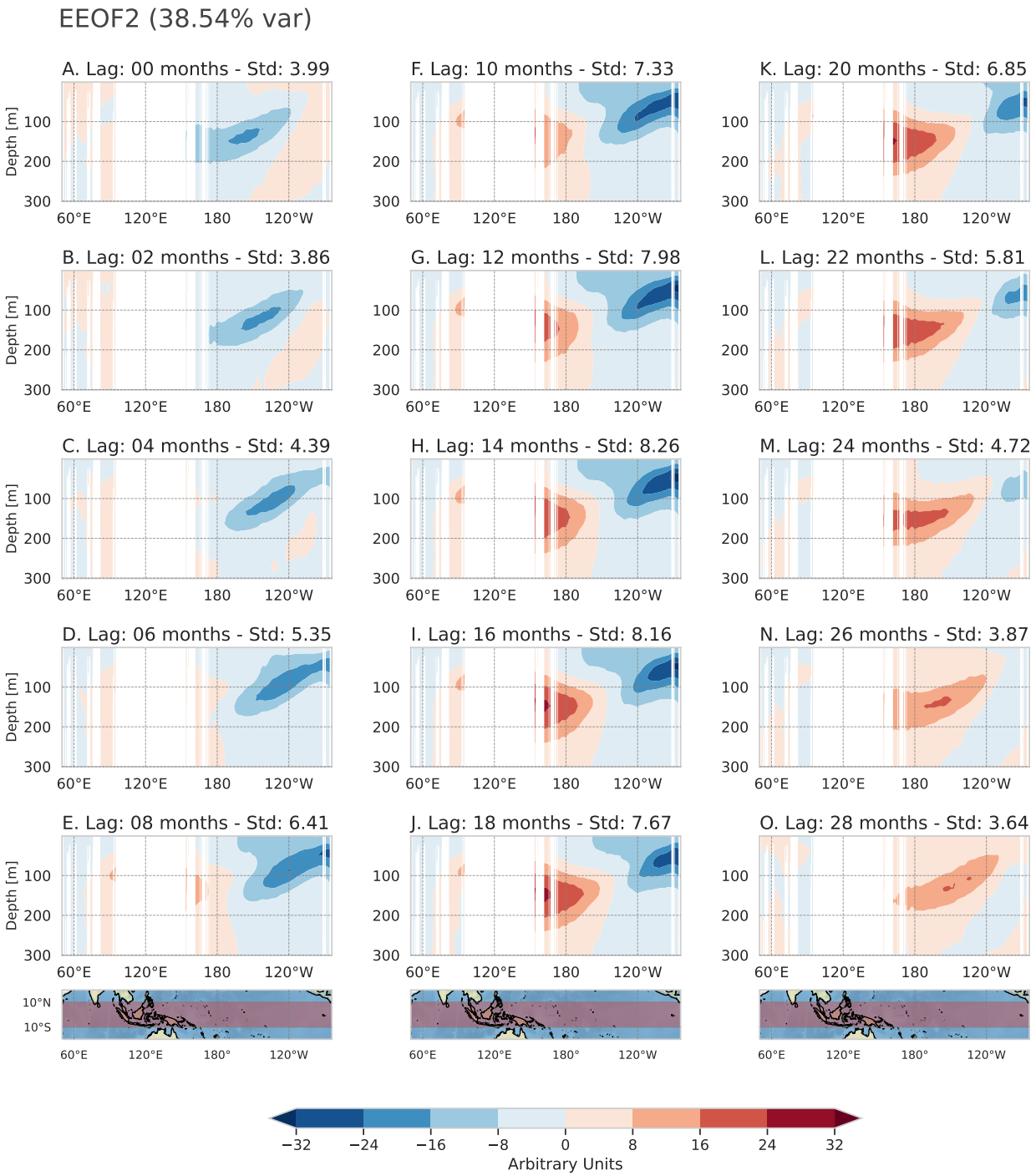

Figure **2-5**.: similar to Figure **2-4** but for the second mode of the subsurface temperature EEOF.

during the first 8-months (Figure **2-4** A-B). From month 0 to month 12, a basin-wide mode is manifested over the Indian Ocean as a delayed response to the El Niño event (Klein et al., 1999; Webster et al., 1999; Murtugudde and Busalacchi, 1999; Saji et al., 1999; Venzke et al., 2000; Luo et al., 2010; N. H. Saji, 2018). Meanwhile, the subsurface tropical Indian Ocean develops a dipole structure (0-8-month lag).

At the 8-16 month lag, the Indian Ocean experiences the westward displacement of the negative loading through the basin's subsurface and the upward propagation of positive loading from the subsurface over the eastern coast, thus, highlighting the influence of ocean dynamics on the interannual SST variability of the Indian Ocean. The previous findings are coherent with earlier observations (Feng and Meyers, 2003; Horii et al., 2008; Wang et al., 2019) and the process described in Figures **2-1** and **2-2**. On a study of the interannual variability of the Indian Ocean, Feng and Meyers (2003) using EEOF of expendable bathythermograph profiles (XBT) also noticed an upward propagation signal along the Sumatra-Java coast before it reached the surface layer. The authors highlighted the role of internal ocean dynamics in influencing the SST pattern of the IOD. Moreover, Horii et al. (2008) using TRITON buoys located close to the equator and over the eastern pole of the IOD also found that before the onset of the 2006 positive IOD event, a region of significant negative anomalies first appeared from the thermocline down to 250m depth before reaching the surface in the following months.

Between 12-16-months lag, as the negative temperature loading over the Western Pacific Ocean moves eastward in the form of a Kelvin wave, the positive temperature loading intensifies over the subsurface of the eastern Indian Ocean and also built up over the western coast of the Pacific Ocean. In the following months, positive loading builds up over the Western Pacific Ocean (i.e., recharge of heat content), favoring the development of the following El Niño event. Figure **2-4** highlights the influence of ocean wave dynamics on ENSO's phase transition represented by the EEOF1.

The second EEOF mode, which accounts for 38.54% of the variability of the data, is shown in Figure **2-5**. In contrast with EEOF1, the time evolution starts with the developing state of the La Niña event in the Pacific Ocean, which will reach its peak around the 6-8th-month lag. Meanwhile, the Indian Ocean describes a positive basin-wide mode. Simultaneously, positive loadings start concentrating over the eastern Indian Ocean (4 and 6 months lag) before the same would emerge over the Western Pacific Ocean. The build-up of warm anomalies over the Western Pacific and its following eastward propagation accounts for the decaying state of the La Niña event and the subsequent transition to El Niño state in the following months. As noted by Wang et al. (2019), the development of the subsurface eastward perturbations that trigger the El Niño events come after warm anomalies were present over the eastern Indian Ocean. In summary, the second oscillation mode (EEOF2) is related to the phase transition of ENSO, as it connected the growth of subsurface temperatures anomalies over the Indo-Pacific Region that will, in turn, shift the state of the ENSO's Pacific conditions in the following months.

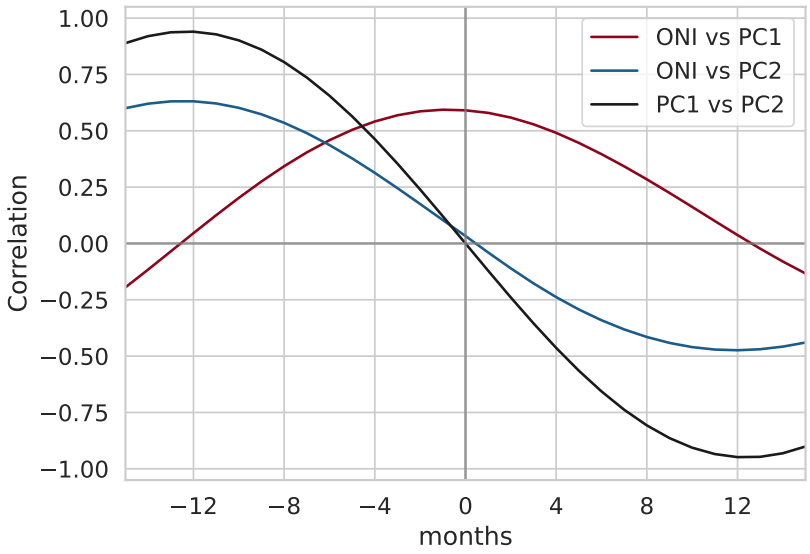

Figure **2-6**.: Lead-lag correlations between the leading time series of the dominant EEOF for the subsurface temperature: ONI index against PC1 (red line); ONI index against PC2 (blue line); and PC1 against PC2 (black line). PC2 is leading both the ONI index and PC1 for about 12 months.

As can be seen in both Figures **2-4** and **2-5**, during the 26th month, the distribution of temperature anomalies in the two tropical oceans is out of phase with those in month 0. Thus, both EEOFs display half a cycle of the co-evolution of both ocean basins, where one mode is leading the other. The lagged correlation (Figure **2-6**) between the leading couple associated time series of EEOF (i.e., PCs, principal components) reveals that the most significant correlations are found when PC1 leads/lags PC2 by 12 months, which could be connected with the quasi-biennial time scale of ENSO (Rasmusson and Carpenter, 1982; Jiang et al., 1995). Moreover, the second mode of variability leads the ONI index by 12 months, thus, potentially suggesting a source of predictability related to the coupled interaction across the two oceans.

Coherently, previous studies have suggested that independently or together, the IOBM and IOD could play a role in leading ENSO phase transitions by modulating Western Pacific wind variability, hence strengthening the quasi-biennial time scale of ENSO (Kug et al., 2006a; Izumo et al., 2010b, 2014; Ha et al., 2017; Cai et al., 2019). Furthermore, Ha et al. (2017) suggested that the combined effect of the IOD and IOBM have a more significant impact on the Western Pacific wind variability in favoring the ENSO phase transition than the sole effect of the IOD or the IOBM alone. The previous result suggests a close link between the EEOF modes and ENSO's phase transition, which is possible through the interbasin ocean waves dynamics and a potential atmospheric/ocean bridge. In addition, we suspect that the second-leading EEOF mode could give helpful insides into the Indian Ocean's influence over the Western Pacific wind variability at interannual time scales.

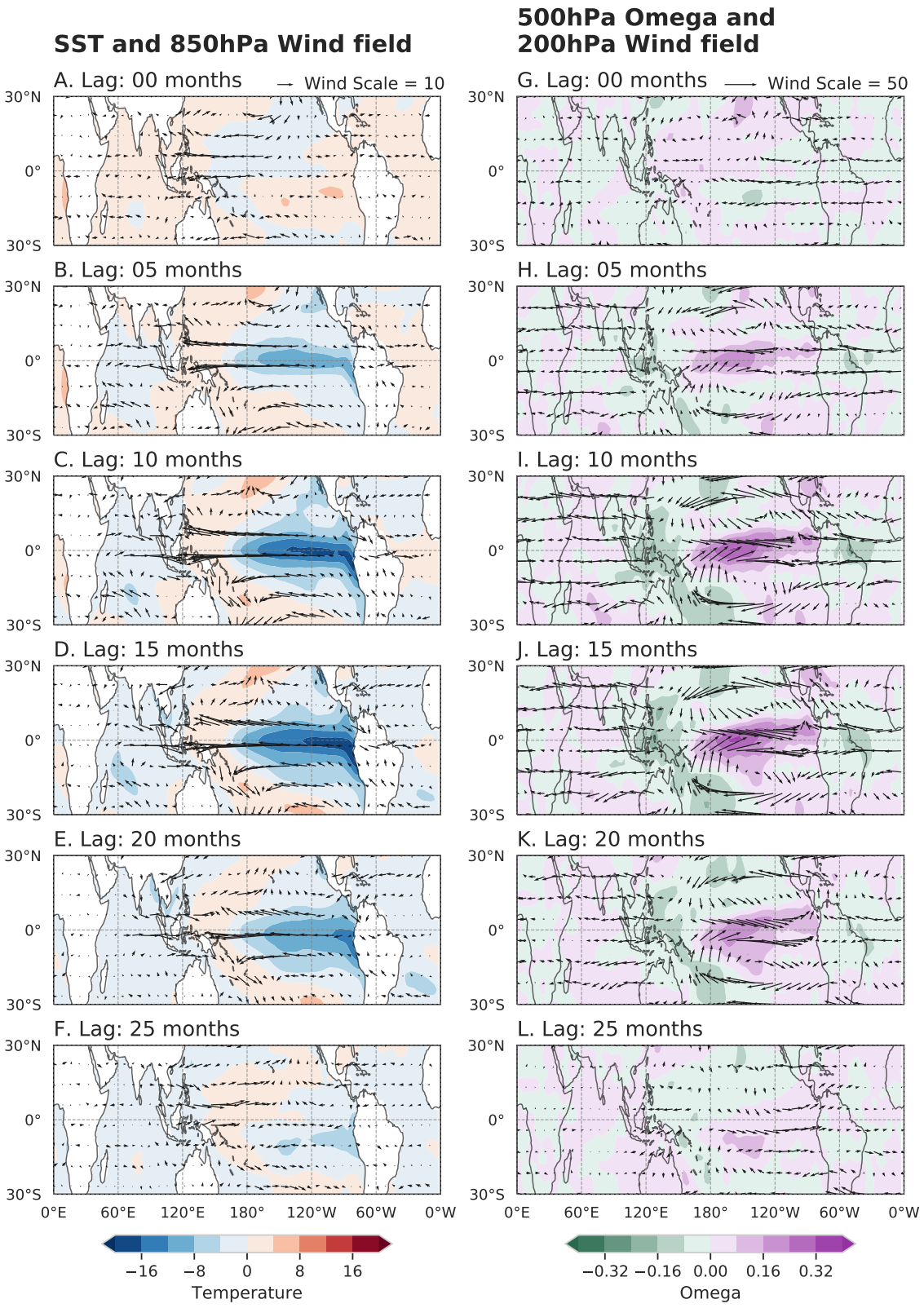

Figure **2-7**.: Left column: SST (shading) and 850hPa wind field (vector) standardized anomalies associated with the second EEOF from month 0 to month 25. The right column is the same as the left column but for the 500hPa vertical velocity Omega (shading) and 200hPa wind field (vector). Dimensionless units.

2.3.2 Atmospheric bridge

To examine a possible atmospheric bridge between the ocean basins connected to the leading interannual subsurface variability, the lower and upper tropospheric wind fields, vertical velocity in the middle atmosphere, and sea surface temperature anomalies were projected onto the second principal component (PC) of the EEOF analysis.

During the first 15 months (Figure **2-7** A through D), the atmospheric response to the EEOF2 on the lower levels consists of a low-level convergence wind anomaly above the Indo-Pacific region. For month 0 over the Pacific Ocean, an anticyclonic circulation is observed over the northwest region, together with an easterly wind over the equatorial western Pacific. Over the Indian Ocean, the anomalous circulation is characterized by cross-equatorial south-easterly winds across the southwestern Indian Ocean and westerlies along the equator. This wind pattern forces open-ocean upwelling and a shoaling of the thermocline in the southwestern region (Xie et al., 2002), which can be observed by the rapid basin-wide SST cooling that started over the southern Indian Ocean and intensified at the southwestern coast. On the other hand, over the Pacific Ocean, the negative SSTAs observed over the eastern Pacific Ocean promote the intensification of the trade winds and the augmentation of the Warm Pool over the western boundary (Figure **2-7** A through E). In conjunction, as previously reported by different studies (Izumo et al., 2010b; Wieners et al., 2016; Wang et al., 2019), the low-level convergence over the Indo-Pacific region favors the accumulation of heat content (Wyrtki, 1985; Jin, 1997a), thus, promoting the development of an El Niño event (Meinen and McPhaden, 2000). After the demise of the La Niña event (Figure **2-7** E-F), the westerly wind anomalies propagate from the Indian Ocean to the Western Pacific Ocean, thus suggesting an atmospheric bridge mechanism in line with previous investigations (Clarke and Van Gorder, 2003; Izumo et al., 2010b; Wieners et al., 2016, 2017). This eastward propagation of zonal wind anomalies from the Indian Ocean to the Pacific had been previously noted (Clarke and Van Gorder, 2003; Izumo et al., 2010b; Wieners et al., 2016), although its mechanism remained unclear (Clarke, 2008). What is clear is that the anomalous westerly equatorial winds interact with the Western Pacific leading to the eastward expansion of the Warm Pool and forcing an oceanic response.

According to Izumo et al. (2010b) a negative IOD event accelerates the Walker circulation, promoting the easterlies anomalies over the Western Pacific Ocean and the buildup of warmer water. Meanwhile, Wieners et al. (2016) proposed that the subsidence over the southwestern Indian Ocean, favored by cold SSTA in the region, gives rise to westerlies over the Indian Ocean and enhanced convection above Indonesia, resulting in easterlies over the Western Pacific Ocean. Additionally, Wieners et al. (2016) found that a cold western Indian Ocean favors easterlies over the Pacific ocean but also the buildup of a strong warm pool. Then, after the sudden demise of the eastern IOD pole in boreal winter, the westerly winds anomalies propagate from the Indian Ocean to the Pacific Ocean, where they trigger an oceanic response that influences the development of an En Niño event (Izumo et al., 2010b; Wieners et al.,

2016, 2017).

Conversely, despite the IOBM-ENSO feedback asymmetry (the amplitude of the Indian Ocean warming being significantly larger than the cooling; Hong et al., 2010), La Niña event is also known to promote the SST cooling of the tropical Indian Ocean by forcing off equatorial upwelling Rossby waves (Xie et al., 2002) over the eastern Indian Ocean that significantly affects the southwestern tropical coast (as seen in Figure **2-7**, Chowdary et al., 2006; Singh et al., 2013). Therefore, the atmospheric evolution coupled to the second EEOF mode captures the close covariations between the Indian and the Pacific Ocean in the interannual time scales, which may be due to mutual influence.

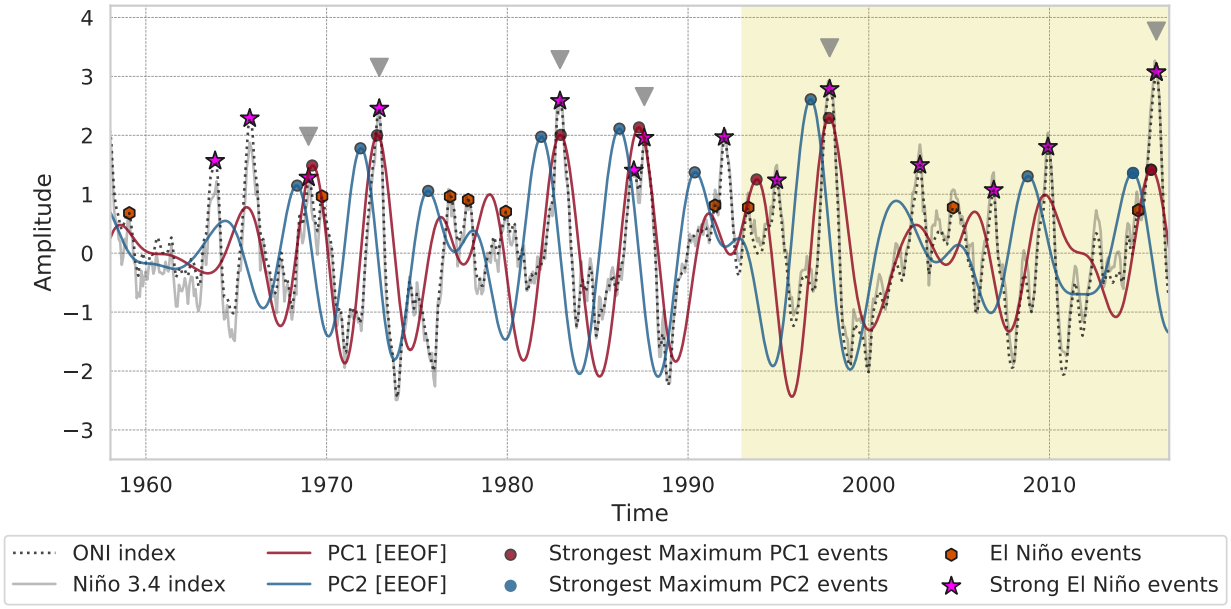

Figure **2-8**.: Standardized time series of the ONI index (dotted line), Niño-3.4 SSTAs (gray line), and the first (PC1, red line) and second (PC2, blue line) principal components of the EEOF analysis. The red (blue) circles indicate the peaks above one standard deviation of PC1 (PC2). According to the ONI index definition, the orange hexagons and the pink stars indicate the El Niño events from 1958 to 2016. Pink stars denote the El Niño events above one standard deviation. The area filled in yellow indicates the period covered by the daily oceanic reanalysis GLORYS2V4 data set. The gray triangles indicates those El Niño events that occurred after a consecutive prominent peak of both PC2 and PC1 (i.e., 1968-69, 1972-73, 1982-83, 1987-88, 1997-98, and 2015-16). The indexes were standardized in order to compare them.

Composite atmospheric evolution

Figure **2-8** displays the leading couple associated PC series of EEOF modes against the ONI index and Niño-3.4 SSTAs. The figure shows that both PC1 and PC2 have a similar interannual variation to the ONI index, showing especially large amplitudes around 1970 to 2000. Moreover, extreme El Niño events, including 1972-73, 1982-83, and 1997-98 are matched to a large PC1 and PC2; events that coincide with the fully coupled IOD-ENSO-IOBM interaction that favors a fast ENSO phase transition as reported by Ha et al. (2017). Moreover, as reported by Kessler (2002) during the 1982-83, 1986-87, and 1997-98 El Niño events, the Upper Ocean Heat Content (or the Warm Water Volumen, WWV) suddenly increased just before the El Niño began, which conflicts with the idea of a slow heat recharge as a consequence of La Niña.

To identify possible large-scale mechanisms related to the suggested atmospheric bridge, we made a composite analysis of the strongest El Niño events (i.e., ONI index above one standard deviation as indicated by the pink stars on Figure **2-8**) that coincided with significant peaks of the time series associated with the couple leading EEOF modes. The six events selected (i.e., 1968-69, 1972-73, 1982-83, 1987-88, 1997-98, and 2015-16) occurred after a consecutive significant peak of both PC1 and PC2 indexes. This list of events also contains the termed Super El Niño events (i.e., 1972-73, 1982-83, and 1997-98; Ha et al., 2017). On the other hand, comparing the results of the six selected events with the remaining 14 (i.e., 1963-64, 1965-66, 1969-70, 1976-77, 1977-78, 1979-80, 1986-87, 1991-92, 1994-95, 2002-03, 2004-05, 2006-07, 2009-10, and 2014-15) will allow us to observe the main differences in the evolution of the atmospheric structure.

With the six El Niño events selected from Figure **2-8**, we performed a composite analysis to explore the evolution of the horizontal atmospheric structure. The velocity potential and stream function were computed from the wind field via spherical harmonics for this analysis. In the following figures, month 0 corresponds to the positive peak of PC2 occurring 12 months before the peak of the El Niño event. The 850 hPa stream function shows the development of a couple of anomalous twin off-equatorial cyclones over the Indian Ocean and a strong off-equatorial anticyclonic circulation over the northwestern Pacific Ocean starting around month -4 (Figure **2-9** B). This circulation pattern gets disorganized around month -2 but reintensifies during month 0. Hereafter a significant center of anomalous low pressure develops over the other subtropical Pacific ocean Figure **2-10**-E, promoting an off-equatorial cyclonic circulation over the Pacific. From then on, the anomalous circulation intensifies over the eastern Pacific Ocean coherently with the development of a warm ENSO event.

The velocity potential at 200hPa (an important diagnostic of upper-level divergence and thus convective activity in the tropics; Figure **2-11**) initially shows the westward migration of stronger upper-tropospheric divergence from the Warm Pool region into the central Indian Ocean. After month 0, the negative core migrates eastward to the eastern Pacific Ocean, coinciding with the mature stage of the El Niño event and the peak in the Walker Circulation

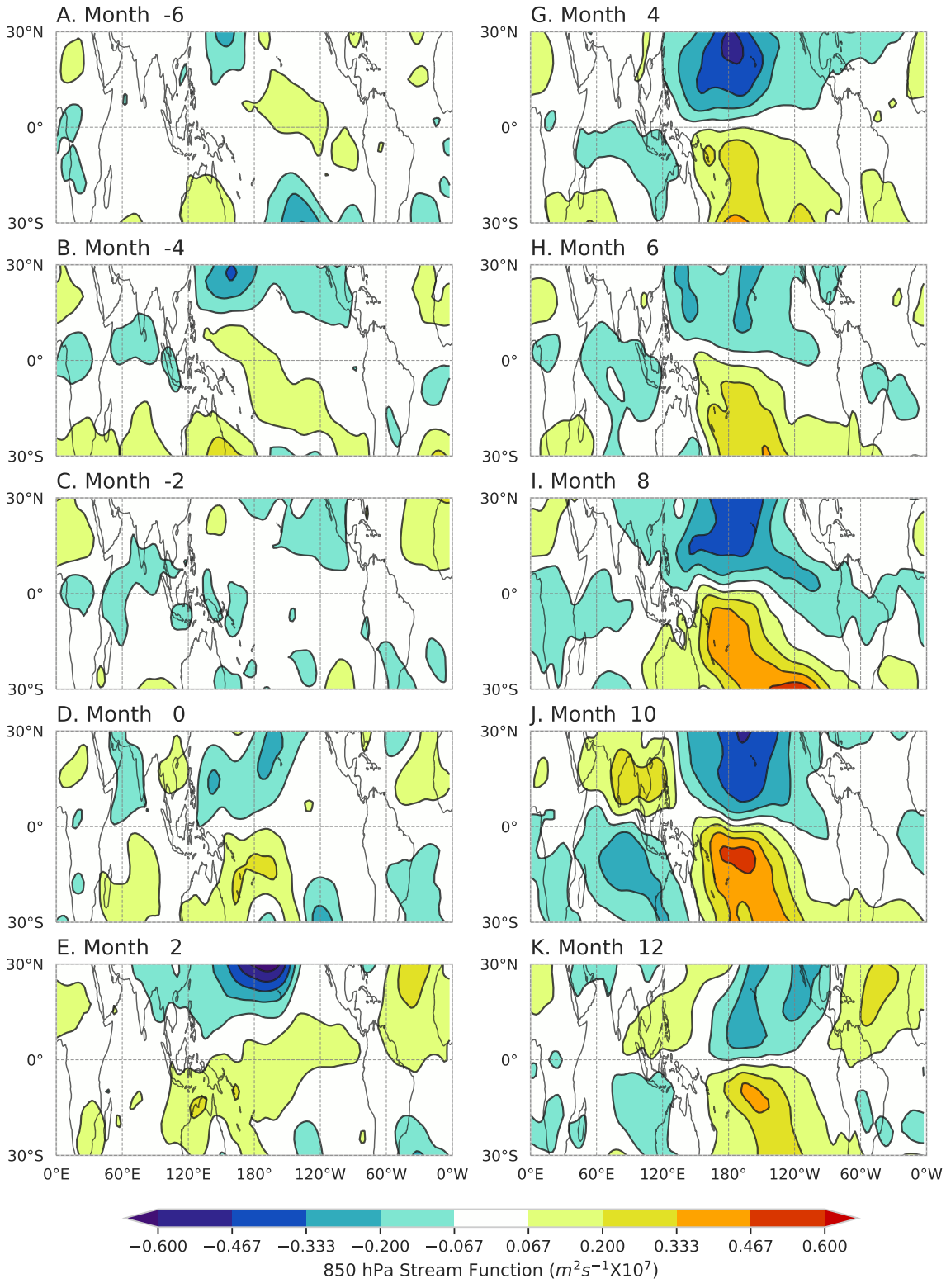

Figure **2-9**.: Time evolution of the composite 850 hPa Stream Function anomalies from month -6 to month 12 center around the minimum peak of PC2 for the six events highlighted in Figure **2-8**. The El Niño events selected are 1968-69, 1972-73, 1982-83, 1987-88, 1997-98, and 2015-16. Month 0 corresponds to the peak of PC2 time series.

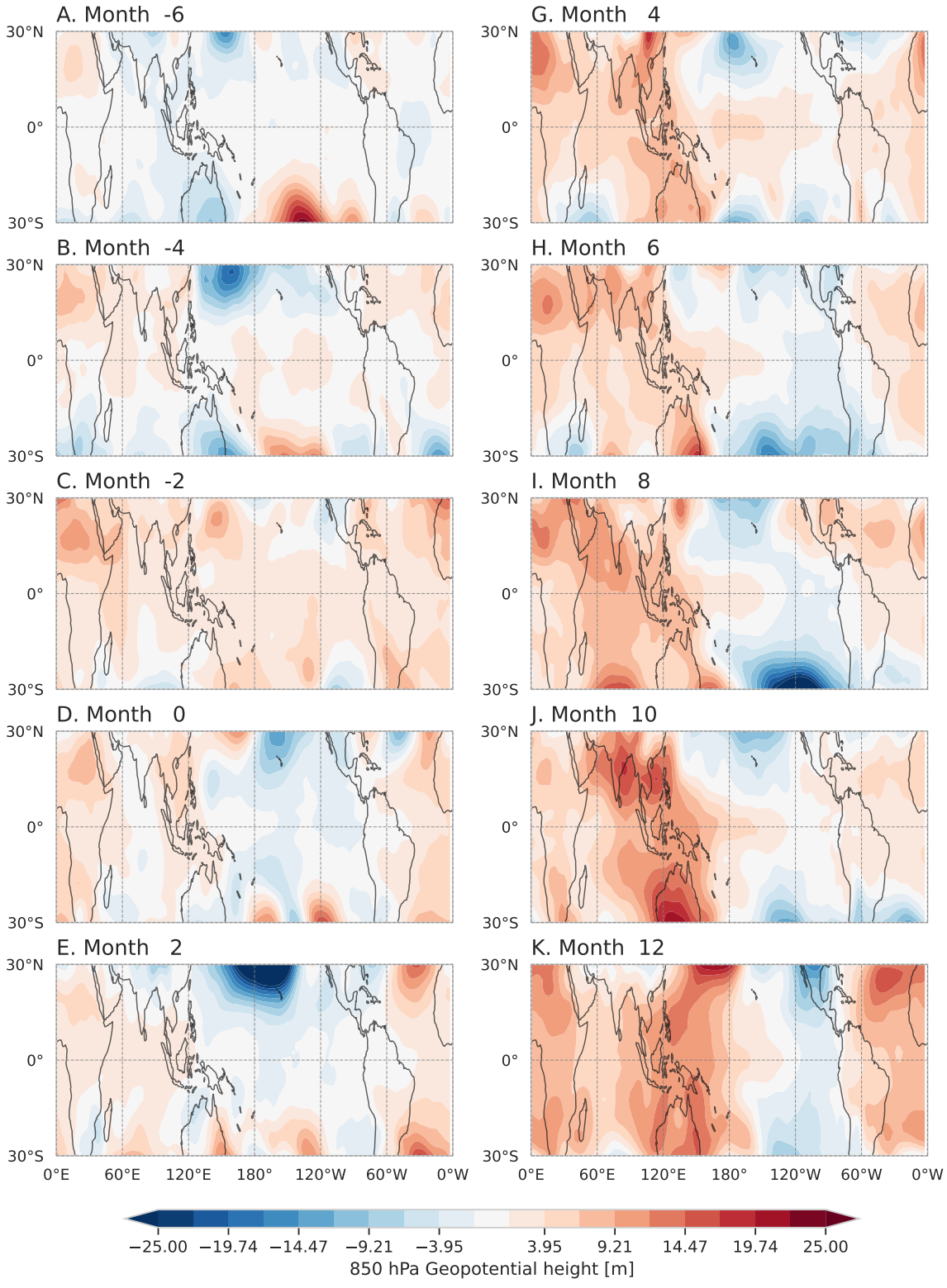

Figure **2-10**.: Similar to Figure **2-9** but for the 850hPa geopotential height anomalies.

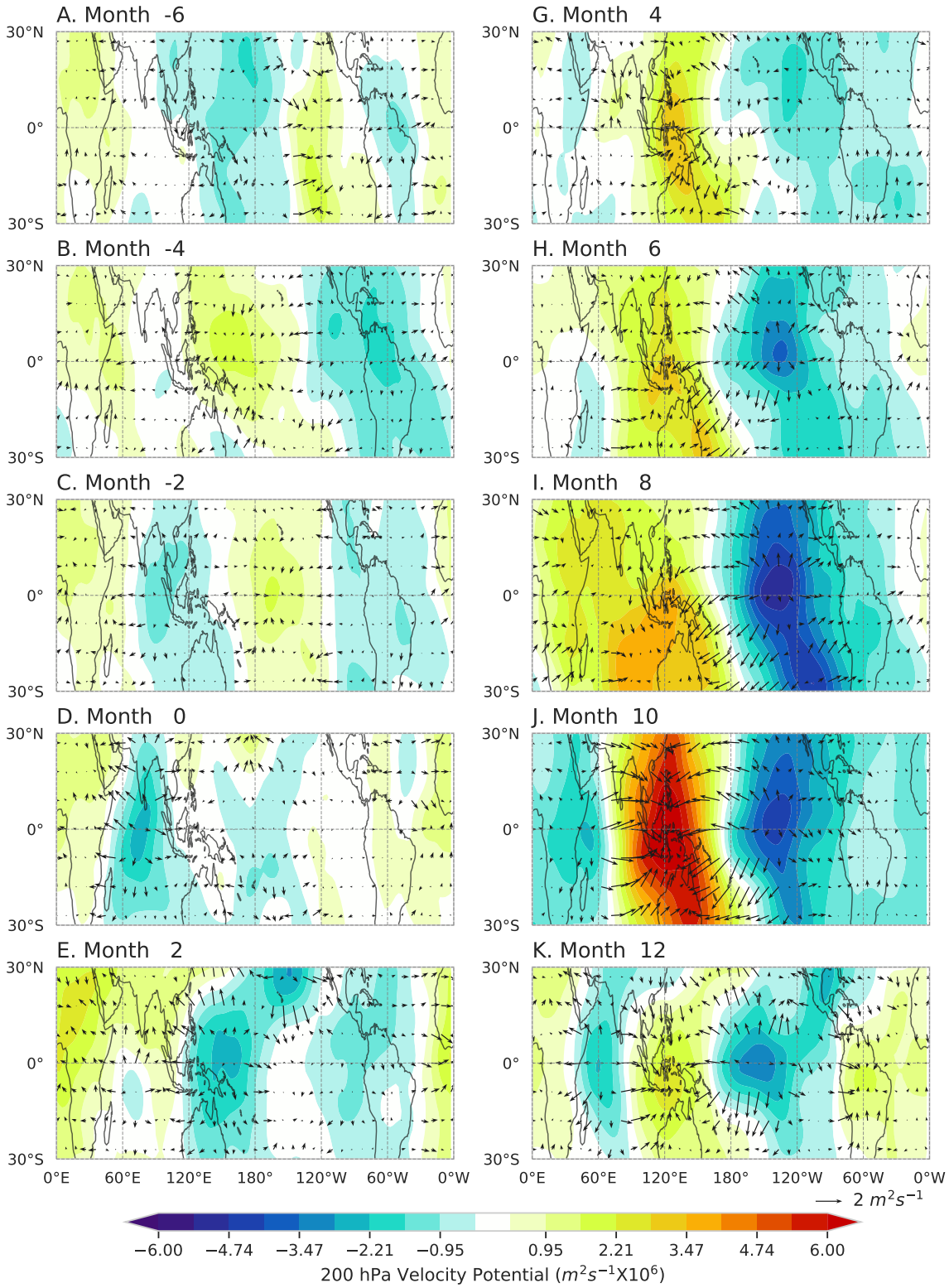

Figure **2-11**.: Similar to Figure **2-9** but for the Velocity Potential and divergent winds anomalies at 200hPa.

changes (Reason et al., 2000). The eastward movement of the velocity potential is consistent with previous observational findings (Yasunari, 1985; White and Cayan, 2000) and a CGCM model results (Behera et al., 2006) where zonal divergent wind anomalies propagate eastward from the Indian Ocean to the Pacific, leading to a favorable precondition to the onset of the El Niño event (Yamagata and Masumoto, 1990).

The previous analysis indicates that before the evolution of some of the most significant El Niño events, the migration of enhanced convection from the Warm Pool region over the Indian Ocean induced by ocean dynamics (EEOF modes) favors the development of anomalous off-equatorial twin cyclones. The anomalous circulation is responsible for the low-level converging anomaly above the Indo-Pacific region seen in Figure **2-7** (e.g., cross-equatorial south-easterlies winds over the southwestern Indian Ocean and westerlies along the equator); and build-up of positive heat content anomalies over the Warm Pool region. The recharge of the WWV of the Western Pacific causes the eastward migration of deep convection along with the zonal propagation of the westerlies from the Indian Ocean into the Warm Pool, where the anomalous westerlies winds generate an oceanic response and favors eastward the expansion of the Warm Pool. Moreover, the six of the El Niño event studied (i.e., 1968-69, 1972-73, 1982-83, 1987-88, 1997-98, and 2015-16) evolved into a La Niña the following year, thus highlighting the fast phase transition mediated by the Indo-Pacific coupling as suggested by Ha et al. (2017).

However, comparing the composite evolution of the 14 remaining El Niño events shows that the magnitude of the anomalies is much smaller than when analyzing only the six highlighted events. On the other hand, the Figure **2-12** shows that the cyclonic circulation characteristic of El Niño events is formed much later and more disorganizedly than in the previous case. And as the velocity potential shows (Figure **2-13**), there is no joint interaction with the Indian Ocean, as the eastward propagation produced in this ocean is not shown. This suggests that the coupled interaction between the two oceans is dominated by the stronger El Niño events.

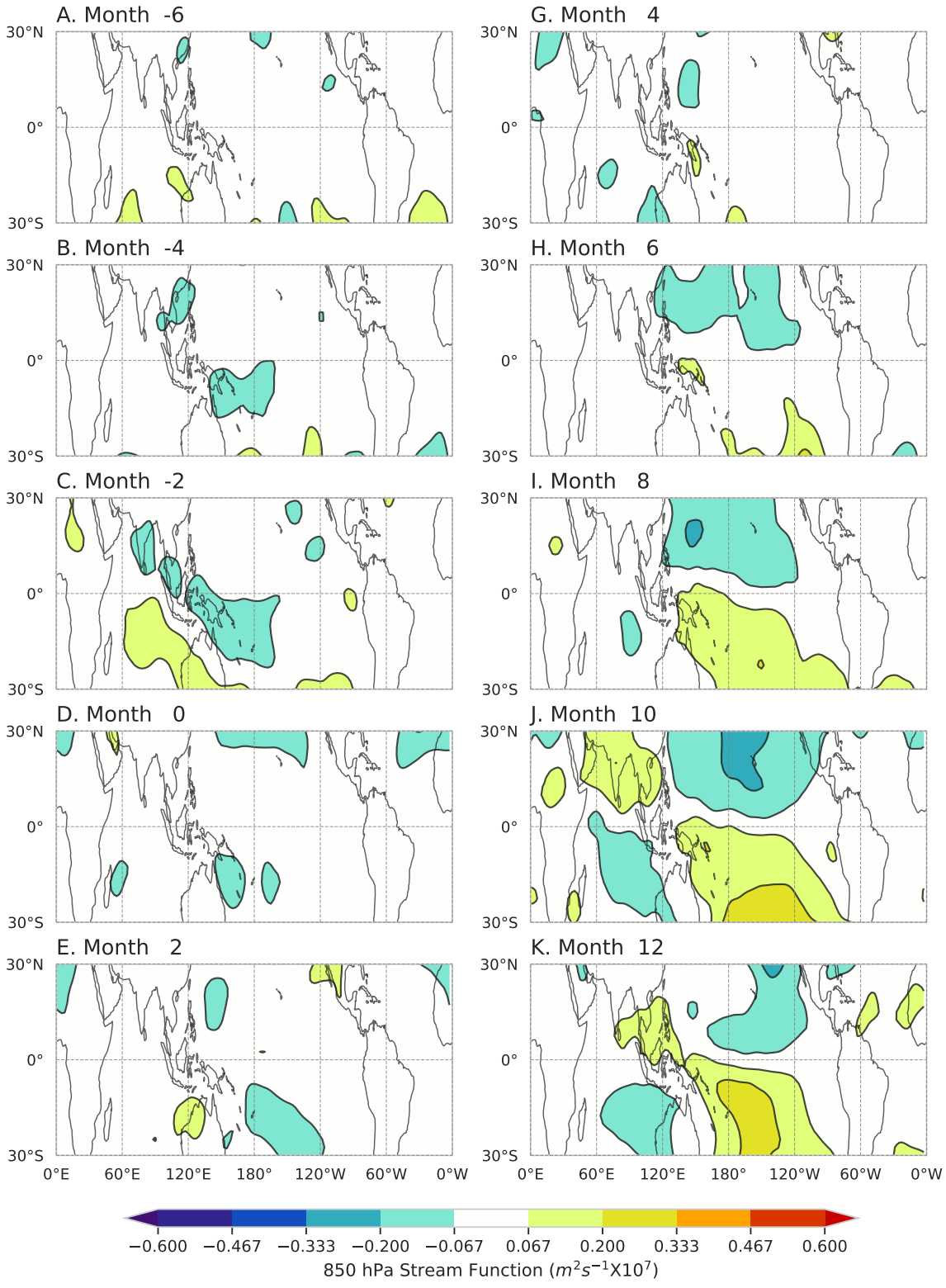

Figure **2-12**.: Time evolution of the composite 850 hPa Stream Function anomalies from month -6 to month 12 center around the minimum peak of PC2 for the six events highlighted in Figure **2-8**. The El Niño events selected are 1963-64, 1965-66, 1969-70, 1976-77, 1977-78, 1979-80, 1986-87, 1991-92, 1994-95, 2002-03, 2004-05, 2006-07, 2009-10, and 2014-15. Month 0 corresponds to the peak of PC2 time series.

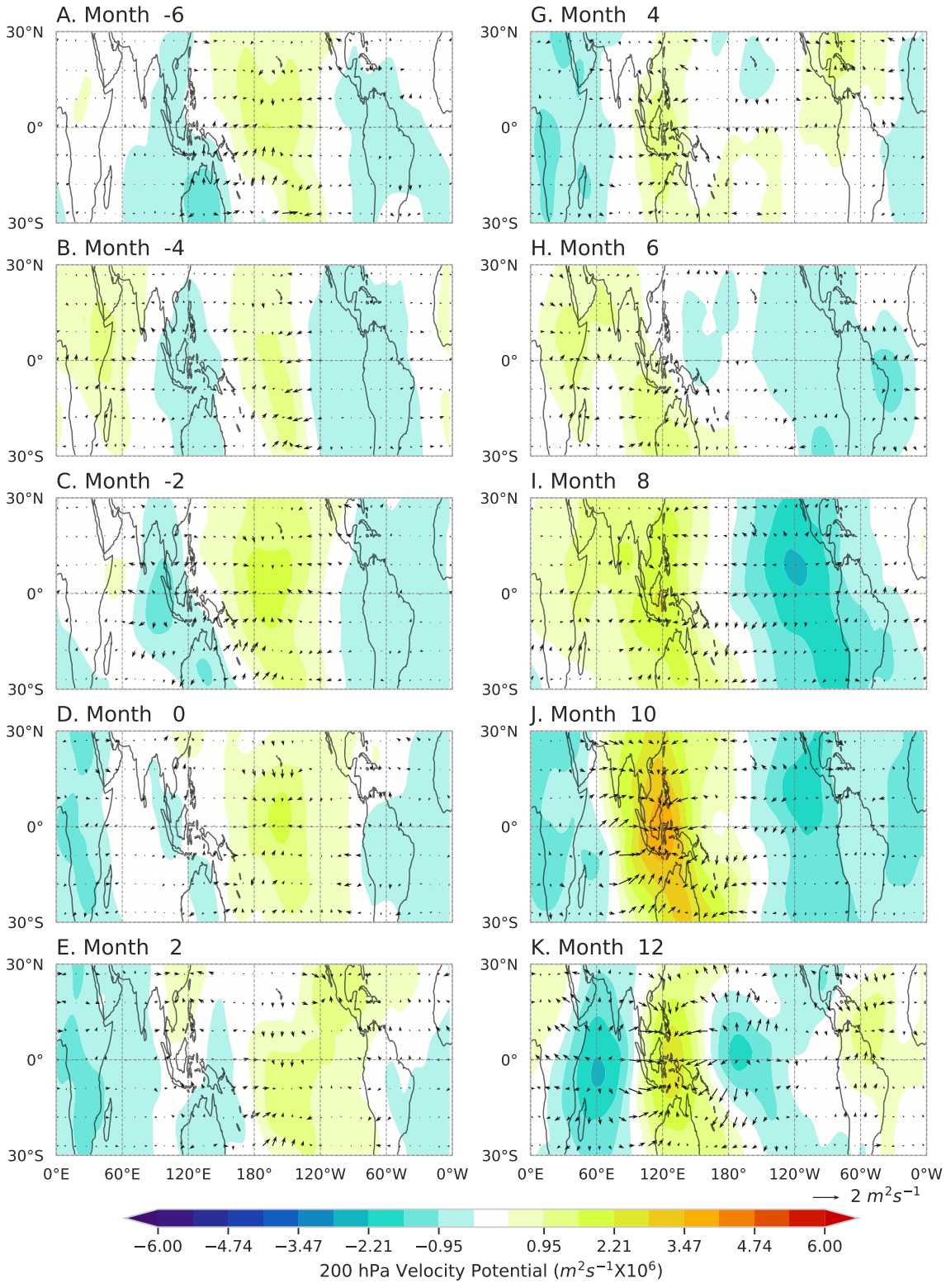

Figure **2-13**.: Similar to Figure **2-12** but for the Velocity Potential and divergent winds anomalies at 200hPa. The El Niño events selected are 1963-64, 1965-66, 1969-70, 1976-77, 1977-78, 1979-80, 1986-87, 1991-92, 1994-95, 2002-03, 2004-05, 2006-07, 2009-10, and 2014-15. Month 0 corresponds to the peak of PC2 time series.

2.3.3 Interannual modulation of the ISV

As suggested by Kessler et al. (1995), the intraseasonal variability (ISV, 20-90 days) could be a window through which the Pacific reacts to signals originated outside the basin. Additionally, the intraseasonal wind variability is also modulated by Western Pacific westerlies and the eastward extension of the Warm Pool (Yamagata and Masumoto, 1990; Kessler et al., 1995; McPhaden, 1999; McPhaden et al., 2006b; Zhang, 2005). Therefore, the zonal propagation of westerlies from the Indian Ocean over the Warm Pool could also suggest an enhancement of the intraseasonal wind variability over this region modulated by the Indian Ocean (Izumo et al., 2010b).

The MJO, on its eastward propagation, is known to give rise to westerly wind events (WWEs, also known as westerly wind bursts or WWBs) in the western-to-central equatorial Pacific (Kessler and Kleeman, 2000; Zhang, 2005). Moreover, earlier studies pointed out the modulation of the MJO-related activity by the Indian Ocean (Izumo et al., 2010a; Wilson et al., 2013; Benedict et al., 2015; Wieners et al., 2016). The MJO-driven wind stress forces intraseasonal Kelvin waves (Kessler et al., 1995; Hendon et al., 1999; Zavala-Garay et al., 2005; Hendon et al., 2007) that remotely warm the Eastern Pacific. WWEs associated with the MJO are determinants for the ENSO in the intraseasonal time scale, given that they have a more significant influence over the ocean because the wind events are spatially and temporally coherent (Kessler et al., 1995; Shinoda and Hendon, 2001; Zhang and Gottschalck, 2002).

Figure **2-14**-A displays the power Hovmoller (time-longitude diagram) of the wavelet variance for the OLR anomalies in the 20-90 day band at each longitude between 5°N-5°S. The diagram highlights the spatial and temporal variability of the MJO-associated OLR fluctuations. It can be noticed that the maximum variance is located over the Indian Ocean and the Western Pacific Warm Pool, the only regions, from a climatological point of view, with sufficiently high SST temperature to sustain enhanced convection for extended periods (Waliser and Graham, 1993). The power Hovmoller also exhibits the interannual eastward expansion of MJO-related activity into the eastern Pacific Ocean, which corresponds with the commonly observed eastward propagation of the MJO along with the eastward expansion of the Warm Pool during El Niño events (Yamagata and Masumoto, 1990; Kessler et al., 1995; McPhaden, 1999; McPhaden et al., 2006b; Zhang, 2005).

Figure **2-14**-B shows the time-average 20-90-day power as a function of longitude. The figure compares the longitudinal distribution of power during the entire record (black line) against the activity only considering the boreal winter and spring season (DJFMAM, green line), the time of the year when the MJO intensifies (Zhang, 2005). When contrasting the time-average power during DJFMAM for the most significant positive peak of PC2 (6 events considered, red line in Figure **2-14**-B) against the baselines (black and green lines), a broad local maximum appears over the Warm Pool region (135°-170°E), indicating an increase of activity over the region. Additionally, the standardized 3-month running-mean of the 20-

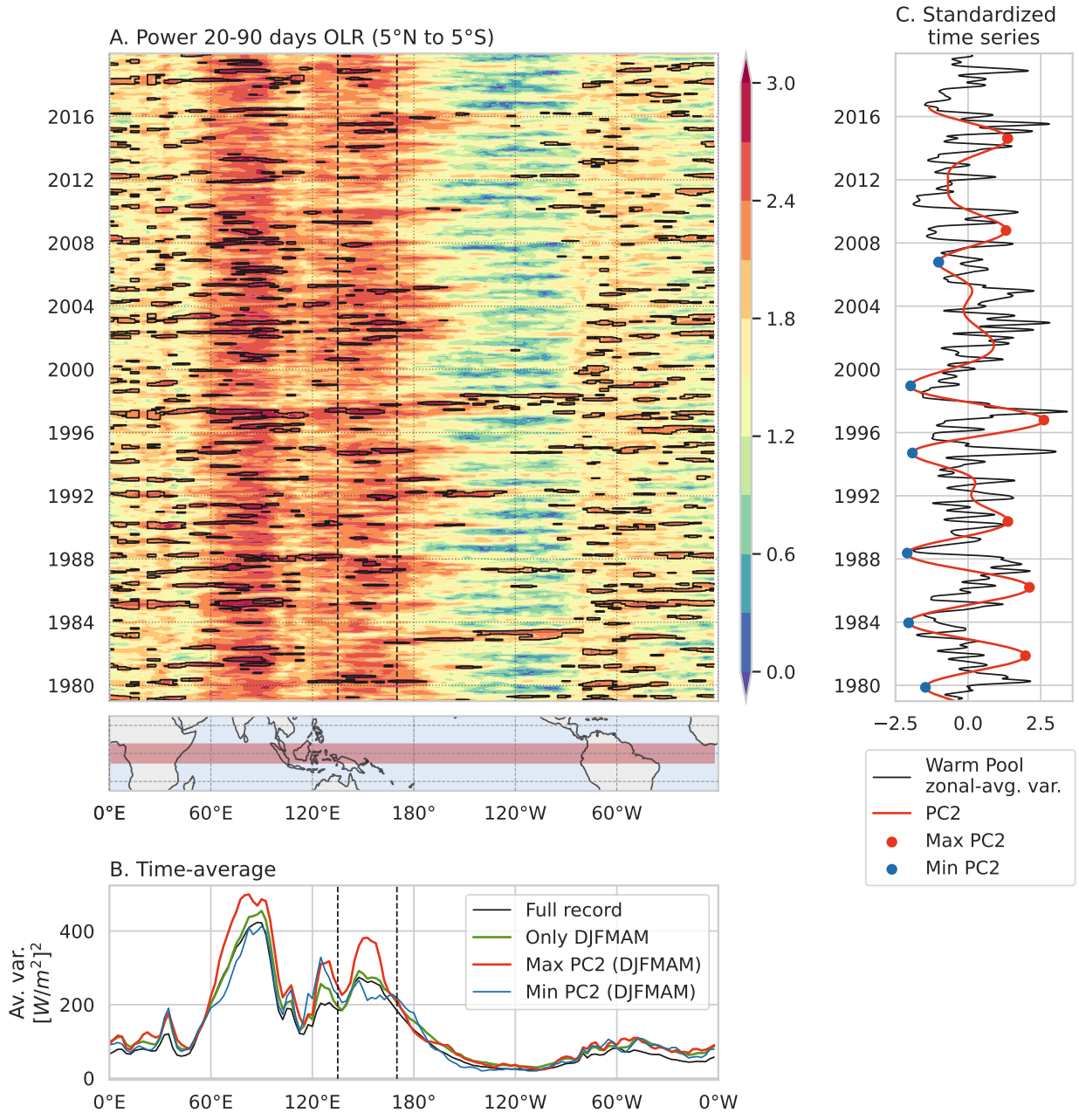

Figure **2-14**.: (A) The 20-90 days OLR power Hovmoller diagram between 5°N-5°S. The thick back contour is the 95% confidence level, using the corresponding white-noise spectrum at each longitude. (B) The time average variance of the complete record of OLR (black); and for only the boreal winter and spring (i.e., DJFMAM) of the whole record (green), during a significant positive peak of PC2 (6 events considered, red) and a significant negative peak of PC2 (6 events considered, blue). (C) Standardized time series of the 3-month running mean of the 20-90 days OLR zonal average variance over the Warm Pool region (135°-170°E, black) and the PC2 time series. In figures (A) and (B), the Warm Pool region is denoted between the two dashed vertical lines.

90 days OLR zonal average variance for the Warm Pool (Figure **2-14**-C) describes similar interannual fluctuations in comparison with the standardized PC2 time series. Our results suggest an interannual modulation of the MJO activity by the leading subsurface variability modes during the boreal winter-spring.

To emphasize the MJO-induced wind influence over the ocean dynamics process in the Indo-Pacific region, we constructed Hovmoller diagrams showing the intraseasonal evolution of crucial variables for El Niño events that coincide with peaks of both PC time series. Considering the temporal coverage of the daily ocean reanalysis data used in this study (1993-2016, refer to Figure **2-8**), it is better to show some particular cases than the composite structure based on a few events.

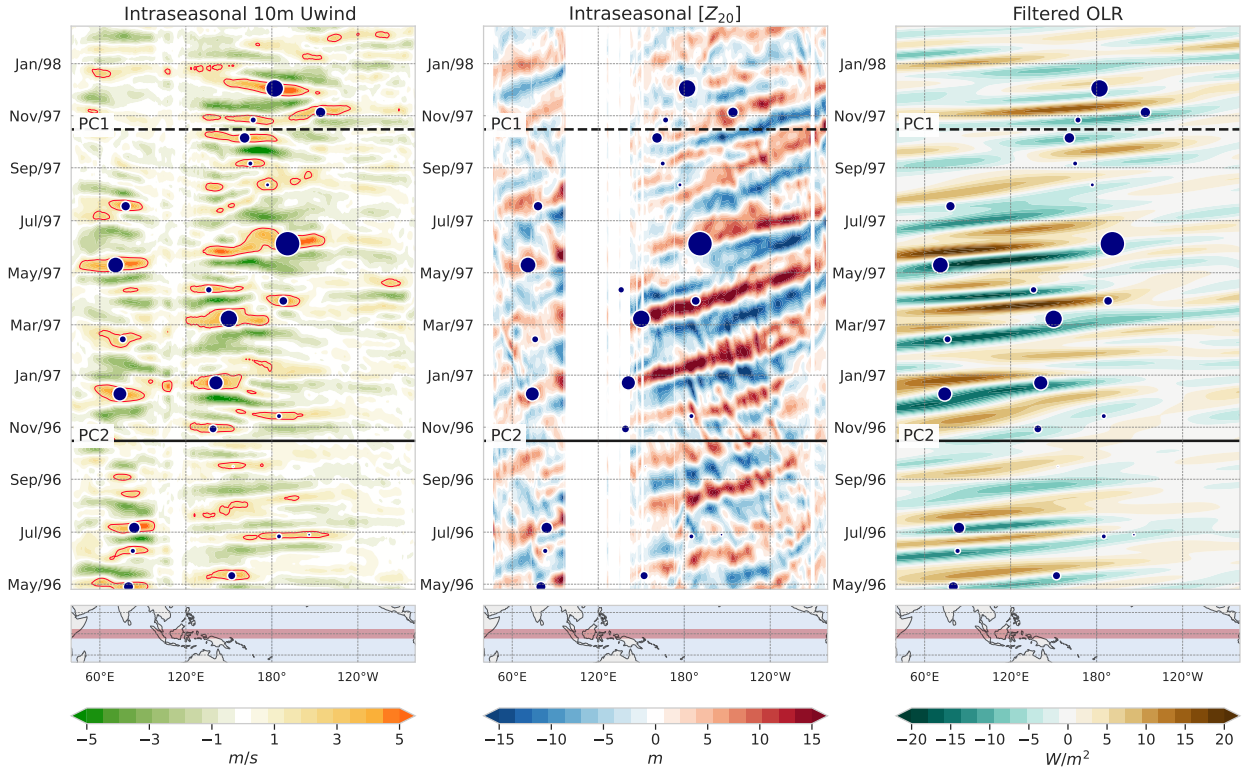

Figure **2-15**.: Average 3°N-3°S time-longitude section for the 1996-97 El Niño event. **A** intraseasonal 10m zonal wind anomalies. Red contours indicate the 2 m/s threshold. **B** intraseasonal thermocline depth anomalies (define as the depth of the 20°C isotherm), and **C** space-time filtered OLR variations. The band-pass filtering retains positive zonal wavenumbers 1-5 and periods between 20-90-days as in Hendon et al. (2007). Negative (positive) values represent the MJO convective (suppressed) phase. Solid blue circles mark WWEs events; the circle radius is proportional to WEI index. The dashed (continuos) black line denotes the peak of PC1 (PC2).

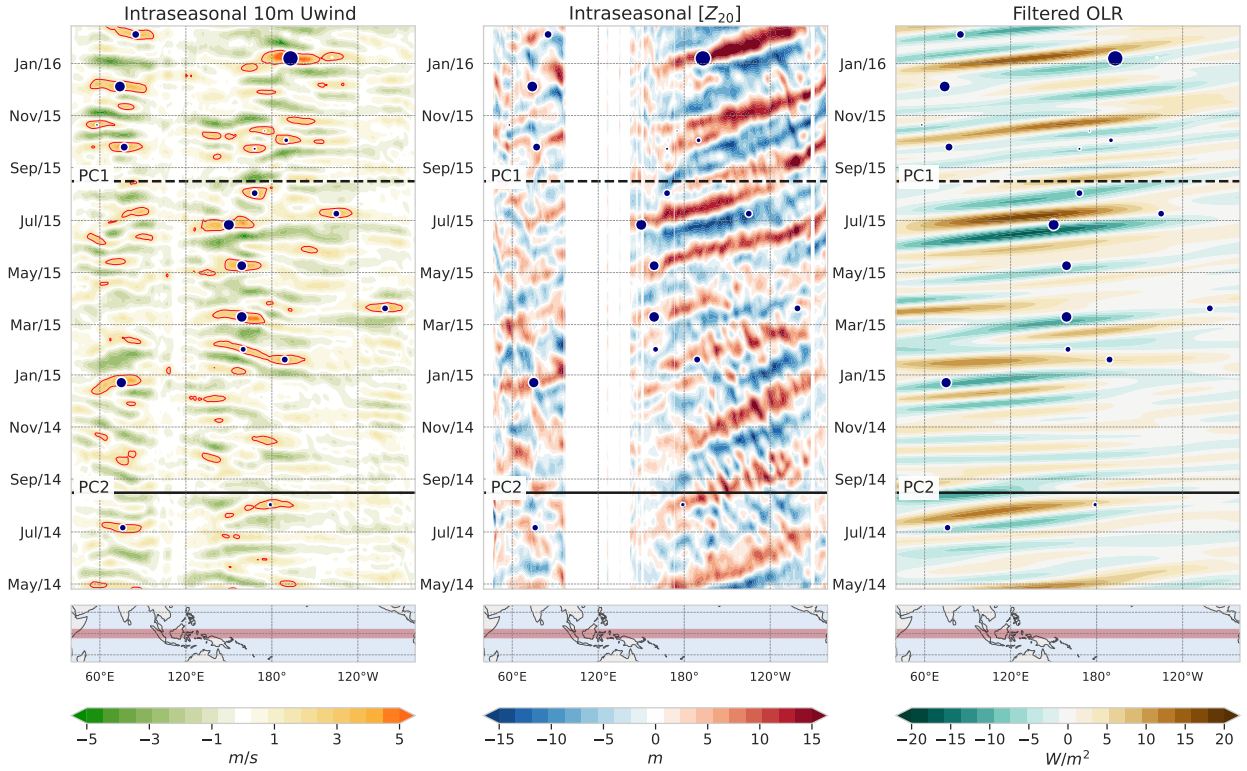

Figure **2-16**.: Similar to Figure **2-15** but for the 2015-16 El Niño event.

The evolution of the 1997-98 El Niño event, one of the strongest on record, was significantly modulated by high-frequency variability (Yu and Rienecker, 1999; McPhaden, 1999). Figure **2-15** A, B shows the intraseasonal oceanic response to a series of WWEs of generally increasing intensity or fetch that occurred prior to and during the development of the warm event. The WWEs, indicated by the blue circles in Figure **2-15**, excited intraseasonal Kevin waves, which is evident from the perturbations that they produced to the thermocline depth (Figure **2-15** B, the depth of the 20^{o}C isotherm was used as a proxy of the thermocline depth). The strong WWEs that occurred from December 1996 to July 1997 were attributed to the convective phase (Figure **2-15** C) of a series of unusually strong MJO events during spring (Yu and Rienecker, 1999; McPhaden, 1999; Lengaigne et al., 2002; Hendon et al., 2007). The MJO-induce westerly winds and the eastward expansion of the warm pool resulted in a positive feedback that allowed the further penetration of the MJO in the Pacific ocean over warm water over which subsequent cycles of the MJO could force the ocean (Figure **2-15** C; refer to McPhaden, 1999).

On the other hand, the 2015-16 El Niño was preceded by an aborted warm event during 2014. According to Levine and McPhaden (2016) during the summer of 2014, an episodic easterly wind event inhibited the development of the El Niño event but also halted the discharge of anomalous Warm Water Volumen (WWV) from the equatorial Pacific. Levine

and McPhaden (2016) claimed that the remaining heat content (WWV) combined with strong WWEs during boreal spring and summer of 2015 gave a head start to the rapid growth of the following warm event. Figure **2-16** exhibit a series of intraseasonal downwelling Kelvin waves excited by WWEs during early 2015. The WWEs were embedded between the convective phase of the MJO, as can be seen in Figure **2-16**-C.

Although the results suggest an interannual modulation of the MJO activity during the boreal winter spring, it does not imply a direct casualty. The short time scale component of the MJO-induced WWEs represents a stochastic component for ENSO variability (Puy et al., 2016). Nonetheless, WWEs are also modulated by the location of the Warm Pool (Eisenman et al., 2005; Gebbie et al., 2007). Consequently, MJO-induced WWEs are only partially independent of ENSO, as ENSO modulates its activity and geographical distribution.

2.4. Conclusions

In this study, the covariability of the Indian and Pacific oceans is assessed by analyzing the subsurface ocean temperature in the tropical band. A simple composite examination of the development of the strongest El Niño events highlights the role of ocean wave dynamics in the evolution of the ENSO and hints at an eastward propagating signal from the Indian Ocean previous to the onset of the El Niño event. In addition, a lead-lagged correlation between the eastern Indian Ocean and the subsurface temperature profile confirms that a signal that started over the Indian Ocean gets amplified over the Pacific Ocean at interannual time scales. Furthermore, we used an empirical approach to diagnose propagation structures through the subsurface temperature across the two basins by utilizing a filtered time Extended-EOF technique. The leading couple EEOF modes capture the covariability between the Indian and Pacific oceans and the ocean wave dynamics responsible for the ENSO event and its systematic phase transition, in agreement with the recharge/discharge framework (Wyrtki, 1985; Jin, 1997a). When the EEOF analysis was performed with different temporal filters, similar structures were obtained, varying only in the magnitude of the anomalies. Additionally, the quasi-biennial time scale of ENSO is shown to be favored by the leading modes of subsurface variability of the two oceans, as the phase transition is coupled to the interbasin interaction. The first EEOF mode portrays the onset of a mature phase of the ENSO and its subsequent transition to the opposite phase forced by ocean waves. Meanwhile, the second mode exhibits the accumulation or depletion of heat content anomalies over the Indo-Pacific region, preconditioning the development of an ENSO event and favoring its phase transition. The second EEOF mode also exposed that the build-up of positive temperature anomalies over the Western Warm Pool region lagged by a few months the accumulation of positive heat content anomalies over the eastern Indian Ocean, thus, suggesting a possible precursor of an El Niño event within the Indian Ocean. However, when the strongest El Niño events were removed (i.e., 1968-69, 1972-73, 1982-83, 1987-88, 1997-98, and 2015-16) and the time Extended EOF analysis performed, there was a substantial

change in the patterns associated with EEOFs (as can be seen in Figure **A-5** and **A-6**). This means that the ocean coupling is dominated by stronger events.

Previous studies focused on the interannual SST variability linked the influence of the Indian Ocean onto ENSO through an atmospheric bridge (Clarke and Van Gorder, 2003; Izumo et al., 2010b, 2014, 2016; Jourdain et al., 2016; Wieners et al., 2016, 2017; Ha et al., 2017; Cai et al., 2019) or an oceanic connection (Yuan et al., 2011, 2013). Here, we investigated a possible atmospheric mechanism coupled with subsurface covariability between the two oceans before an El Niño event was developed. Our results indicated that the build-up of positive temperature anomalies over the eastern Indian Ocean promotes the intensification of the Walker Circulation, which in turn enhances the low-level convergence wind anomaly above the Indo-Pacific region, thus, favoring the building-up of heat content over the Indo-Pacific region. Over the Indian Ocean, cross-equatorial south-easterlies winds across the southwestern Indian Ocean, and westerlies along the equator tilt the thermocline to the eastern Indian Ocean. Meanwhile, a decaying La Niña event forces easterlies across the Pacific Ocean. After the demise of the La Niña conditions, the westerly wind anomalies propagate from the Indian Ocean to the Western Pacific Ocean, thus indicating an atmospheric bridge in line with previous investigations (Izumo et al., 2010b; Wieners et al., 2016, 2017; Wang et al., 2019; Saji et al., 2018). Nevertheless, the mechanism is not entirely independent from the ENSO, as La Niña events are known to cause the SST cooling of the Indian Ocean, thus indicating a two-way interaction between the basins.

A composite analysis of the atmospheric circulation during periods of maximum variability of the EEOF2 (six events selected) exhibited the migration of enhanced convection from the Warm Pool region over the Indian Ocean, which favors the development of anomalous off-equatorial twin cyclones across the Indian Ocean. This anomalous circulation is responsible for the low-level converging anomaly above the Indo-Pacific region, promoting the accumulation of heat content over the region. In addition, the eastward propagation of the velocity potential and zonal divergent wind anomalies from the Indian Ocean onto the Western Pacific coincide with the zonal propagation of the westerlies, leading to favorable preconditioning of the onset of the El Niño event (Yamagata and Masumoto, 1990). Although the empirical ocean modes are coupled to an atmospheric interaction, they are only relevant for some El Niño events, in particular, the strongest ones (i.e., 1968-69, 1972-73, 1982-83, 1987-88, 1997-98, and 2015-16).

Additionally, periods of high positive amplitude of the PCs led to the development of the strongest El Niño events, which were all followed by a La Niña the subsequent year. This highlights the role of the interbasin subsurface coupling between the two basins in favoring the ENSO phase transitions and the tendency of El Niño events to be followed by La Niña during the subsequent year (Larkin and Harrison, 2002; Ohba and Ueda, 2009; McPhaden and Zhang, 2009; Okumura and Deser, 2010). Conversely, future research can complement this investigation by analyzing the coupled interaction that promotes the transition from an El Niño event into La Niña, as the data suggests. In addition, ENSO asymmetry and

its influence over the Indian Ocean could also influence the relationship presented in this chapter, thus representing another path for future work.

In addition, the zonal propagation of westerlies from the Indian Ocean over the Warm Pool could also suggest an enhancement of the intraseasonal wind variability (ISV) over this region modulated by the Indian Ocean (Izumo et al., 2010b). Moreover, a significant fraction of the ISV over the tropics is controlled by the MJO (Madden and Julian, 1971, 1972; Zhang, 2005) which the Indian Ocean can also influence (Izumo et al., 2010a; Wilson et al., 2013; Benedict et al., 2015; Wieners et al., 2016). The MJO's convective phase is known to force intraseasonal Kelvin waves that favor the development of the El Niño event (Kessler et al., 1995; Kessler and Kleeman, 2000; Zhang, 2005; McPhaden et al., 2006b). We found that the longitudinal 20-90day OLR power distribution during the boreal winter and spring season over the Warm Pool is enhanced during the periods of maximum variability of the EEOF2, thus, suggesting an interannual modulation of the MJO activity by the leading subsurface variability modes. Nevertheless, the enhancement of the MJO signal does not imply a direct influence of the Indian Ocean as ENSO can also modulate the intraseasonal activity by the eastward expansion of the Warm Pool region (Eisenman et al., 2005; Gebbie et al., 2007).

Both the atmospheric bridge and the ISV modulation could contribute to the influence of the Indian Ocean over the ENSO. Although the mechanisms are not entirely independent from ENSO, they support a two-way interaction mediated by the leading interannual ocean process. Additionally, it would be worth analyzing an oceanic bridge related to the coupled interaction between the two oceans, as suggested by Yuan et al. (2011, 2013). Overall, the result presented in this chapter highlights the coherent interannual variability between the two oceans and supports the view that tropical Indo-Pacific climate variability should be studied as a whole rather than as separated basin modes.

3. Evaluation of the leading interannual modes of subsurface climate variability in the CMIP6 models

Abstract

Numerous investigations indicated that the main SST variability modes over the Indian Ocean, the IOBM (Indian Ocean Basin Mode) and the IOD (Indian Ocean Dipole), exert an influence over the Western Pacific wind variability favoring a systematic ENSO phase transition and enhancing ENSO's biennial tendency. Using observational data for the last 60 years and the six-phase of Coupled Model Intercomparison Project (CMIP6) historical simulation, this study investigates the role of subsurface interbasin coupling between the Indian and the Pacific Ocean on ENSO evolution. Here, we used an empirical model evaluation approach to assess the representation of the CMIP6 models on simulating the spatial patterns of the leading interannual modes of subsurface variability obtained from the observational data. Our results indicate that 23 out of 39 models (58.97%) coincide in reproducing the variability modes described by the reference data, thus, confirming the role of the subsurface interbasin coupling in the ENSO's oscillatory nature and phase transition. Finally, we compared the performance of the CMIP6 models in simulating the leading interannual subsurface temperature modes with their ability to represent the compressive CLIVAR ENSO metrics. We suggest that the accurate representation of the interbasin coupling at the interannual time scale is determinant for a correct representation of the ENSO phase transition.

Keywords

El Niño-Southern Oscillation (ENSO); CMIP6; Inter-basin Interaction; Tropical Indo-Pacific; Indian Ocean Dipole (IOD); Indian Ocean basin-wide Mode (IOBM); Interannual variability; Empirical orthogonal functions; ENSO transition.

3.1. Introduction

Studying climate models of different hierarchies has been essential for bridging the gap between the theoretical understanding of ENSO and its numerical representation. Moreover, General Circulation Models (GCMs) have been fundamental tools for understanding ENSO

mechanisms, its forecasting, and projecting future ENSO risk. Thus, evaluating the performance of the GCMs in representing the ENSO properties, teleconnections, and mechanisms is extremely necessary to determine the models' strengths and weaknesses, and track model improvements during its development and across generations. Although clear advances in the simulation of ENSO throughout the previous generation of Coupled Model Intercomparison Project (CMIP) models had been noted (Achuta Rao and Sperber, 2006; Flato et al., 2013; Bellenger et al., 2014), well-known systematic errors (Guilyardi et al., 2020) persist in the models' latest generation (Fasullo, 2020; Fasullo et al., 2020; Brown et al., 2020; Planton et al., 2021).

Although the ENSO is rooted in the tropical Pacific Ocean, the main SST variability modes over the Indian Ocean (i.e., the IOBM and the IOD) are suggested to exert an influence over the Western Pacific wind variability favoring a systematic ENSO phase transition; and could event trigger an ENSO event (Clarke and Van Gorder, 2003; Kug and Kang, 2006; Kug et al., 2006b; Ohba and Ueda, 2007; Izumo et al., 2010b, 2014; Luo et al., 2010; Webster and Hoyos, 2010; Okumura et al., 2011; Ohba and Watanabe, 2012; Jourdain et al., 2016; Wieners et al., 2016, 2017; Cai et al., 2019). As a result, a correct simulation of the interbasin processes is suggested to be determinant for the proper representation of the ENSO in the CGCMs and its projections (Kug and Ham, 2012; Ha et al., 2017; Cai et al., 2019; Kug et al., 2020).

In that respect, the IOBM described as a basin-wide warming of the Indian Ocean is known to be a passive response to El Niño caused by the shifting of the Walker circulation and surfaces heat fluxes (Klein et al., 1999; Murtugudde and Busalacchi, 1999; Lau and Nath, 2000, 2003; Alexander et al., 2002; Wu and Kirtman, 2004; Ohba and Ueda, 2005; Kug and Kang, 2006; Kug et al., 2006a,b; Xie et al., 2009, 2016; Cai et al., 2019). However, a warm IOB can favor the fast transition from El Niño to La Ñina by inducing easterlies over the Western Pacific (Kug and Kang, 2006; Kug et al., 2006b; Ohba and Ueda, 2007; Okumura et al., 2011). Moreover, the IOBM evidences an amplitude asymmetry, with a more significant basinwide warming than the corresponding cooling (Hong et al., 2010), which promotes the phase transition from El Niño to La Niña and a shorter duration of El Niño (Ohba and Ueda, 2009; Okumura et al., 2011; Ohba and Watanabe, 2012).

The IOD has a tendency to co-occur with it due to a modulation of the circulation of the Walker circulation over the Indian Ocean (Ueda and Matsumoto, 2000; Gualdi et al., 2003; Annamalai et al., 2003; Shinoda et al., 2004; Fischer et al., 2005). Conversely, positive IOD events that co-occur with El Niño tend to reinforce the warm ENSO phase by inducing anomalous westerly winds in the Western Pacific (Luo et al., 2010; Annamalai et al., 2010). Moreover, the IOD has a tendency to lead ENSO events by more than a year (Izumo et al., 2010b, 2014) which has been related to an atmospheric bridge where the IOD is influencing the development of the following ENSO (Izumo et al., 2010b, 2014, 2016; Jourdain et al., 2016; Wieners et al., 2017). Furthermore, Jourdain et al. (2016), examing both observations and CMIP5 models, concluded that the tendency of positive IOD events to lead to La Niña events by 14 months tends to be more significant than the opposite case. A recent study by

Ha et al. (2017), where they analyzed both observation and CMIP5 simulation, indicated that during the development of the El Niño phase, the combined effect of a concurrent positive IOD followed by an IOBM promotes a robust rapid transition to La Niña in comparison with the independent effect of either the IOD or IOBM.

The previous investigations suggest that the SST variability over the Indian Ocean favors the ENSO phase transition, thus, enhancing ENSO's biennial tendency. Moreover, in Chapter 2, the leading modes of subsurface variability between the two oceans at interannual time scales showed a close relationship to the ENSO's phase transition, thus emphasizing the role of the subsurface interbasin coupling over the ENSO evolution. Consequently, in this chapter, we assess the skill of CMIP6 models in reproducing the observed interannual modes of climate variability by comparing their historical simulations of the subsurface temperature against the observational data. Then, taking advantage of a freely available compressing set of ENSO diagnostics metrics for CGCMs (CLIVAR ENSO Metrics Package, hereafter CME2021; Planton et al., 2021); we compare the performance of the GCMs in simulating the leading interannual subsurface temperature modes with their ability to represent the CLIVAR ENSO metrics.

3.2. Data and methods

The monthly subsurface potential temperature of the ocean from the European Center for Medium-Range Weather Forecast (ECMWF) ocean reanalysis data (ORAS5; Zuo et al., 2019) was used as the reference dataset for the period of 1958-2014. From the CMIP6 (Eyring et al., 2016) we use 39 models that had available historical simulations of the subsurface temperature (Table **3-1**). Throughout the document, only the first ensemble member of each model was used for the same time coverage of the reference data.

Considering the different spatial resolutions of the different data sets, the observational data (ORAS5) was brought to the exact resolution of each CMIP6 model by bilinear interpolation methods. Also, similar to Subsection 2.3.1, the data were detrended, and a band-pass filter between 3-7 years was applied to the longitudinal average cross-section between 10°N and 10°S. Then, we used the extended empirical orthogonal function technique (EEOF; Weare and Nasstrom, 1982) with a 28-month sequence lag to diagnose the dominant pattern of interannual variability. The longitude–depth domain used for the analysis was the tropical band from surface to 350 m depth. From the EEOF technique, the two leading extended spatial patterns obtained for each GCM were compared with the leading couple spatial patterns achieved from the reference data (ORAS5) for the particular resolution analyzed. The Figure **3-1** shows the variance distribution explained by the oscillation modes for both observational data and CMIP6 models. Since the first pair of EEOFs explain a similar percentage of the variance, it is possible for the modes to swap positions. Considering this possibility, the evaluation of EEOF performance was carried out among the combination of the first pair of modes for which the highest correlations were obtained. Finally, Taylor

Institution	Model	Resolution lon/lat	Vertical levels	Top grid cell (m)	Reference
CSIRO-ARCCSS	ACCESS-CM2	360x300	50	0-1	Dix et al. (2019)
CSIRO	ACCESS-ESM1-5	360x300	50	0-1	Ziehn et al. (2019)
AWI	AWI-CM-1-1-MR	1140x720	46	0-5	Semmler et al. (2018)
AWI	AWI-ESM-1-1-LR	720x360	46	0-5	Danek et al. (2020)
BCC	BCC-CSM2-MR	360x232	40	0-10	Wu et al. (2018)
BCC	BCC-ESM1	360x232	40	0-10	Zhang et al. (2018)
CAMS	CAMS-CSM1-0	360x200	50	0-10	Rong (2019)
CCCma	CanESM5	361x290	45	0-6.19	Swart et al. (2019)
CAS	CAS-ESM2-0	362x196	30	0-10	Chai (2020)
NCAR	CESM2	320x384	60	0-10	Danabasoglu (2019b)
NCAR	CESM2-FV2	320x384	60	0-10	Danabasoglu (2019a)
NCAR	CESM2-WACCM	320x384	60	0-10	Danabasoglu (2019d)
NCAR	CESM2-WACCM-FV2	320x384	60	0-11	Danabasoglu (2019c)
THU	CIESM	720x560	46	0-6	Huang (2019)
CMCC	CMCC-CM2-HR4	1442x1051	50	0-1	Scoccimarro et al. (2020)
CMCC	CMCC-CM2-SR5	362x292	50	0-1	Lovato and Peano (2020)
CMCC	CMCC-ESM2	362x292	50	0-1	Lovato et al. (2021)
EC-Earth-Consortium	EC-Earth3	362x292	75	0-1	EC-Earth (2019a)
EC-Earth-Consortium	EC-Earth3-AerChem	362x292	75	0-1	EC-Earth (2020a)
EC-Earth-Consortium	EC-Earth3-CC	362x292	75	0-1	EC-Earth (2021)
EC-Earth-Consortium	EC-Earth3-Veg	362x292	75	0-1	EC-Earth (2019b)
EC-Earth-Consortium	EC-Earth3-Veg-LR	362x292	75	0-1	EC-Earth (2020b)
FIO-QLNM	FIO-ESM-2-0	320x384	60	0-10	Song et al. (2019)
NOAA-GFDL	GFDL-CM4	1440x1080	75	0-2	Guo et al. (2018)
NOAA-GFDL	GFDL-ESM4	720x576	75	0-2	Krasting et al. (2018)
NASA-GISS	GISS-E2-1-G	360x180	40	0-10	NASA/GISS (2018)
MPI-M	ICON-ESM-LR	720x360	40	0-12	Lorenz et al. (2021)
IPSL	IPSL-CM5A2-INCA	182x149	31	0-10	Boucher et al. (2020)
IPSL	IPSL-CM6A-LR	362x332	75	0-2	Boucher et al. (2018)
IPSL	IPSL-CM6A-LR-INCA	362x332	75	0-2	Boucher et al. (2021)
UA	MCM-UA-1-0	192x80	18	0-40	Stouffer (2019)
MIROC	MIROC6	360x256	63	0-2	Tatebe and Watanabe (2018)
HAMMOZ-Consortium	MPI-ESM-1-2-HAM	256x220	40	0-12	Neubauer et al. (2019)
MPI-M	MPI-ESM1-2-HR	802x404	40	0-12	Jungclaus et al. (2019)
MPI-M	MPI-ESM1-2-LR	256x220	40	0-12	Wieners et al. (2019)
MRI	MRI-ESM2-0	360x363	61	0-2	Yukimoto et al. (2019)
NUIST	NESM3	384x362	46	0-6	Cao and Wang (2019)
SNU	SAM0-UNICON	320x384	60	0-10	Park and Shin (2019)
AS-RCEC	TaiESM1	320x384	60	0-10	Lee and Liang (2020)

Table **3-1**.: List of models considered from the CMIP6 on their historical simulation (1958-2014) of the subsurface temperature of the ocean. The models AWI-CM-1-1-MR, AWI-ESM-1-1-LR, and ICON-ESM-LR that originally have an unstructured grid were converted to a regular grid according to their nominal resolution of 25, 50, and 50 km respectively.

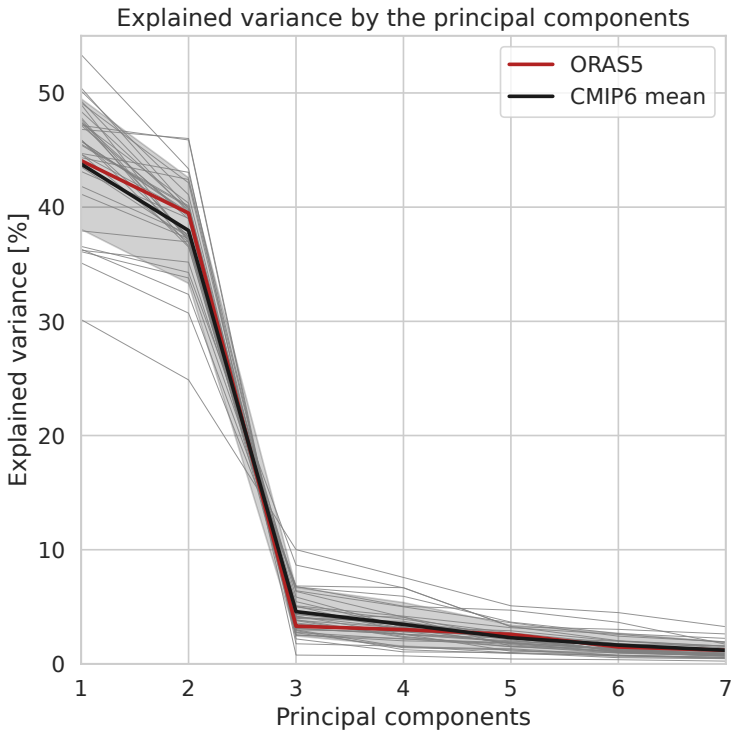

Figure **3-1**.: Distribution of variance explained by the first EEOF modes for observational data (ERA5, red line) and CMIP6 models (thick black line). The gray lines show the particular results of the CMIP6 models

Diagrams (Taylor, 2001) were used as a statistical summary of the performances of each model.

As ENSO involves complex interactions across an extensive range of space and time scales (Timmermann et al., 2018), a growing number of state-of-the-art coupled models are resolving finer time scales and resolutions; thus, increasing the resources needed to analyze and evaluate the models' output. Recently, freely available diagnostic frameworks (Guilyardi et al., 2016; Planton et al., 2021) have provided a compressing set of ENSO diagnostics and metrics for GCMs, facilitating the intercomparison process and the selection of the best models suited for a particular need. In a combined effort, the CLIVAR Pacific Region Panel and community experts on ENSO developed a set of performance metrics to evaluate ENSO simulations, applied these metrics to the CMIP5 and CMIP6 models, and made their codes and results available to the public domain (Planton et al., 2021).

To suggest a possible relationship between the performance of the GCMs in representing the leading interannual subsurface temperature modes and how well models simulate the observed characteristics of ENSO, we used the result of the CEM2021 (Planton et al., 2021, which are freely available on `https://cmec.llnl.gov/results/enso/`). The CEM2021 are divided into three categories: Performace (background climatology and basic ENSO char-

acteristics), Teleconnections (ENSO's worldwide teleconnections), and Processes (ENSO's internal processes and feedbacks). Planton et al. (2021) analyzed the historical simulations of 46 CMIP5 models and 42 CMIP6 models initialized in 1850 and run to 2014. Their results are also based on the first ensemble member of each model; meanwhile, the observation data set varies in time coverage depending on the source used (refer to Planton et al., 2021). Furthermore, on their analysis, both models and observations were regridded toward a generic 1°x1° grid before computing the metrics when needed. From the 39 CMIP6 models from which the subsurface temperature was available, only 30 were also analyzed by Planton et al. (2021) on the CEM2021.

To objectively summarize results across all metrics, Planton et al. (2021) used a common normalization based on the mean error distribution of 88 models (42 from CMIP5 and 46 of CMIP6) against the reference data set. In this study, we acquired the non-normalized performance of each model (Planton et al., 2021) and normalized it based on the data available to us. As a diagnosis metric for the EEOF modes, we choose the root mean square error (RMSE) between the spatial pattern of the coupled leading interannual modes obtained from the observations compared to the patterns computed using the GCMs.

3.3. Results and discussion

Figure **3-2** and Figure **3-3** summarized the CMIP6 models' performance on simulating the spatial patterns of the leading couple interannual EEOF modes. In general, the results are very consistent between the two figures. This is because individual models have a similar performance in reproducing EEOF1 and EEOF2 separately, thus implying the close association between the extended modes. Moreover, 25 (23) of the 39 models from 15 (14) different institutions display correlations higher than 0.75 and between a distance range of 0.5 standard deviations from the observations for EEOF1 (EEOF2). The fact that various institutions coincide in reproducing these variability modes confirms that they represent a relevant process in the interannual time scale.

Additionally, a higher resolution does not guarantee a better performance on a general scope as models of considerably different resolutions had similar results. Nevertheless, the majority of the high-performance models have a nominal resolution of 100 km or more refined. Besides, models with higher resolutions achieved better scores for some institutions than models with coarser resolutions, e.g., GCMs belonging to MPI-M, IPSL, NOAA-GFDL, CMCC, and AWI institutes.

We also noted that the models belonging to the same institute tend to have similar metrics, which could be related to a shared conceptualization of the models. For example, GCMs associated with EC-Earth Consortium have a close correlation and relative similar standard deviation; meanwhile, models affiliated with the IPSL institute have similar correlations but different standard deviations.

Our results indicate that the CMIP6 models that best simulate the spatial patterns of both

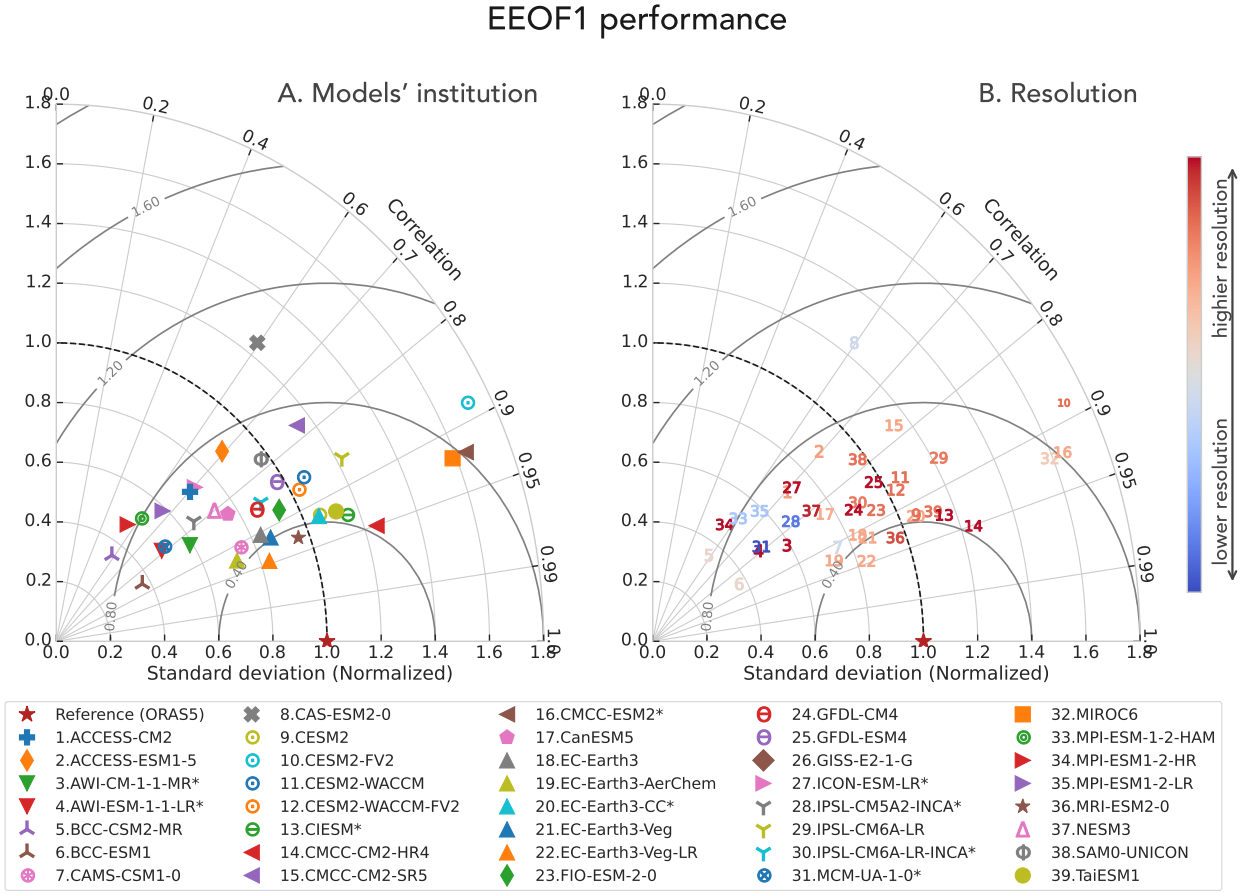

Figure **3-2**.: Normalized Taylor diagrams for the representations of the spatial pattern for the first leading interannual mode of the subsurface temperature (EEOF1). The figure is comparing ORAS5 observations with the historical simulations of the CMIP6 models for the period 1958–2014. Figure (A) indicates the models' institution; models with the same marker belong to the same modeling institution. Figure (B) compares the models' performance against their horizontal resolution. A star (*) after a model name indicates that the model was not considered by Planton et al. (2021). Model not shown in the figure: GISS-E2-1-G (std: 2.33, corr: 0.82).

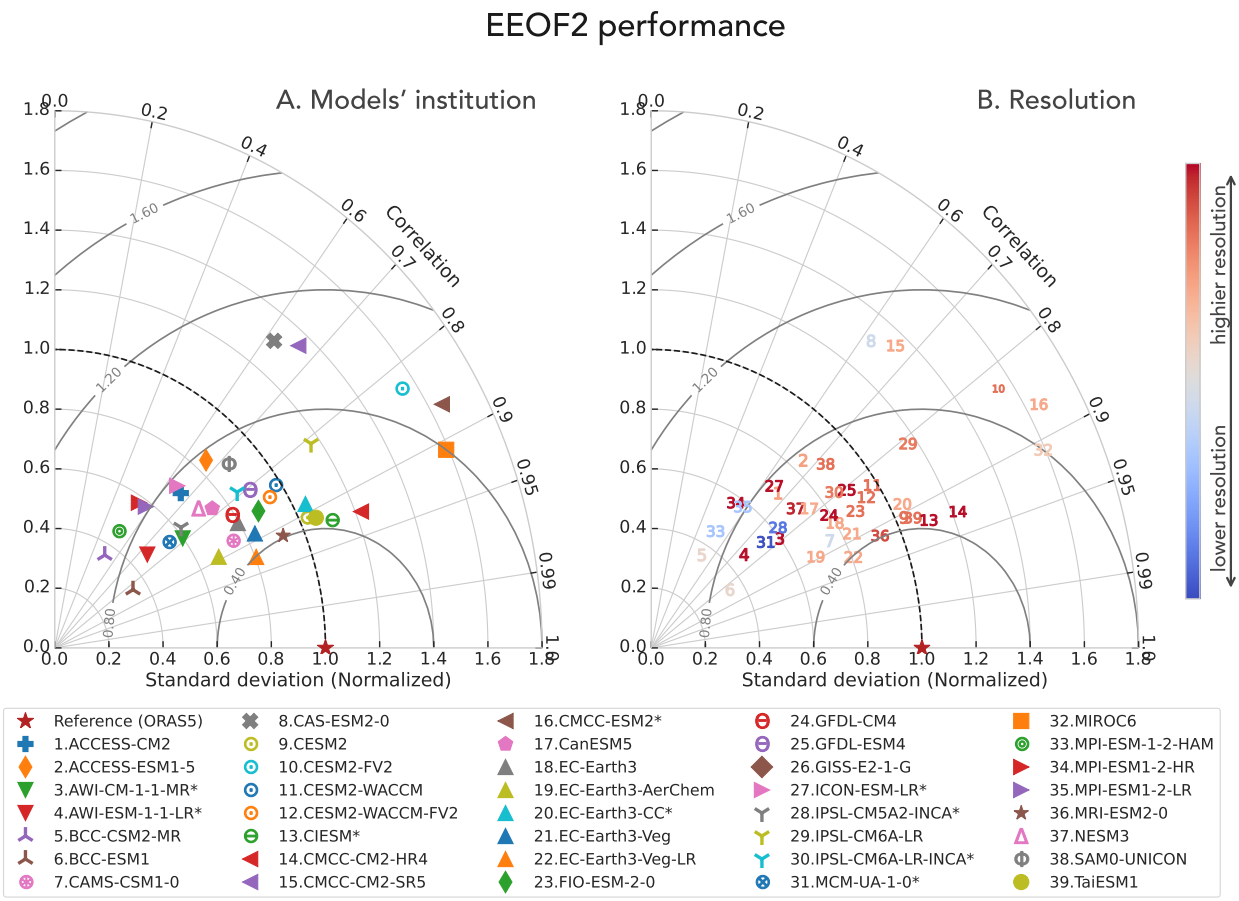

Figure **3-3**.: Same as Figure **3-2** but for EEOF2. Model not shown in the figure: CMCC-ESM2 (std: 1.97, corr: 0.12).

extended modes are EC-Earth3-Veg-LR, MRI-ESM2-0, CMCC-CM2-HR4, CIESM2, and TaiESM1. Meanwhile, the worst spatial representation models are CAS-ESM2-0, CESM2-FV2, MPI-ESM1-2-HR, GISS-E2-1-G and BCC-CSM2-MR.

Figure **3-4** presents an overview of CMIP6 results using a portrait plot for each of the three diagnostic metrics defined as part of the CEM2021 (cf., Figure 2 on Planton et al., 2021) in addition to the one proposed here to analyze the leading interannual modes of subsurface variability. The figure presents the normalized metrics against the multi-model mean error (MMME) to summarize results across all metrics objectively. Here we calculated the MMME with the 30 models that were also analyzed by Planton et al. (2021). Additionally, the color scale in Figure **3-4** (± 2 standard deviation from the MMME in each column) is indicated relative to the range of error of the multi-model mean. Thus the figure highlights the performance of each model relative to the multi-model distribution. For most models, the relative performance is mixed across the metrics, and as indicated by Planton et al. (2021) there is no physically consistent way to combine the metrics of each collection to come up with a single objective ranking; it all depends on the specific climate phenomenon studied.

Given that, in general, the models have a similar representation of the EEOF modes, as also noted in Figures **3-2** and **3-3**, the majority of the models marginally outperformed the MMME. As a result, Figure **3-4** clearly highlights the models with a weaker representation of the process (as indicated by the darker red boxes).

To establish a possible relationship between the ENSO performance metrics and the representation of the interannual subsurface modes, we computed the intermetric correlations across the CMIP6 models (Figure **3-5**). This analysis pointed out that the representation of both EEOF modes is highly correlated with the ENSO life cycle (ENSO_lifecycle, correlation of 0.84) and the climatological bias of the zonal structure of the zonal wind stress (eq_Taux_bias, correlation of 0.06). The ENSO life cycle metric evaluates the temporal evolution of the Niño 3.4 SSTA associated with ENSO. Usually, an El Niño event terminates quickly after the mature phase and shifts into a cold phase by the following summer. In contrast, La Niña tends to persist throughout the second year and reintensifies in winter (also known as the ENSO transition asymmetry; Larkin and Harrison, 2002; Ohba and Ueda, 2009; McPhaden and Zhang, 2009; Okumura and Deser, 2010). On the other hand, the eq_Taux_bias estimate the zonal RMSE of the equatorial Pacific climatological zonal wind stress (Taux) between the model and observations. According to Planton et al. (2021), CGCMs usually show a decreased circulation in the Central Pacific and an increased circulation over the Western Pacific.

The previous analysis of the subsurface interannual variability modes (Subsection 2.3.1) indicated that the leading couple EEOF modes represent the oscillator nature of ENSO through the co-evolution of the Pacific and Indian oceans' wave dynamics and were also closely related with the ENSO phase transition. The frequent shifting between the two opposite phases of the ENSO can be interpreted as alternations between the two EEOF modes (Figures **2-4** and **2-5**). Consequently, the high correlation between the ENSO life cycle with the EEOF mode metrics highlights the dominant role of the ocean dynamics on the oscillatory nature of ENSO and its phase transition (Zebiak and Cane, 1987; Suarez and Schopf, 1988; Neelin et al., 1998; Jin, 1997a). A common bias between CMIP6 models is to portray short-duration La Niña events, a weak capacity to generate 2-year La Niña and a weak representation of the ENSO asymmetry transition; thus, translating into problems in reproducing the diversity of events duration (Planton et al., 2021). Here we suggest that these biases are related to a weak representation of the primary interannual ocean dynamics process as it is shown by Figure **3-4**, where the interbasin coupling favors the ENSO phase transition. Furthermore, the underlined correlation between the EEOF's metrics and the equatorial Taux bias points out the ENSO's sensitivity to the representation of the climatological features and their associated effects on ENSO variability. Biases in the representation of the climatological Taux affect the equatorial upwelling and the zonal tilt of the equatorial thermocline (Guilyardi et al., 2020).

Alternatively, An and Kim (2018) investigated the mechanisms responsible for the asymmetrical ENSO transition over the observational record and compared it against CMIP5

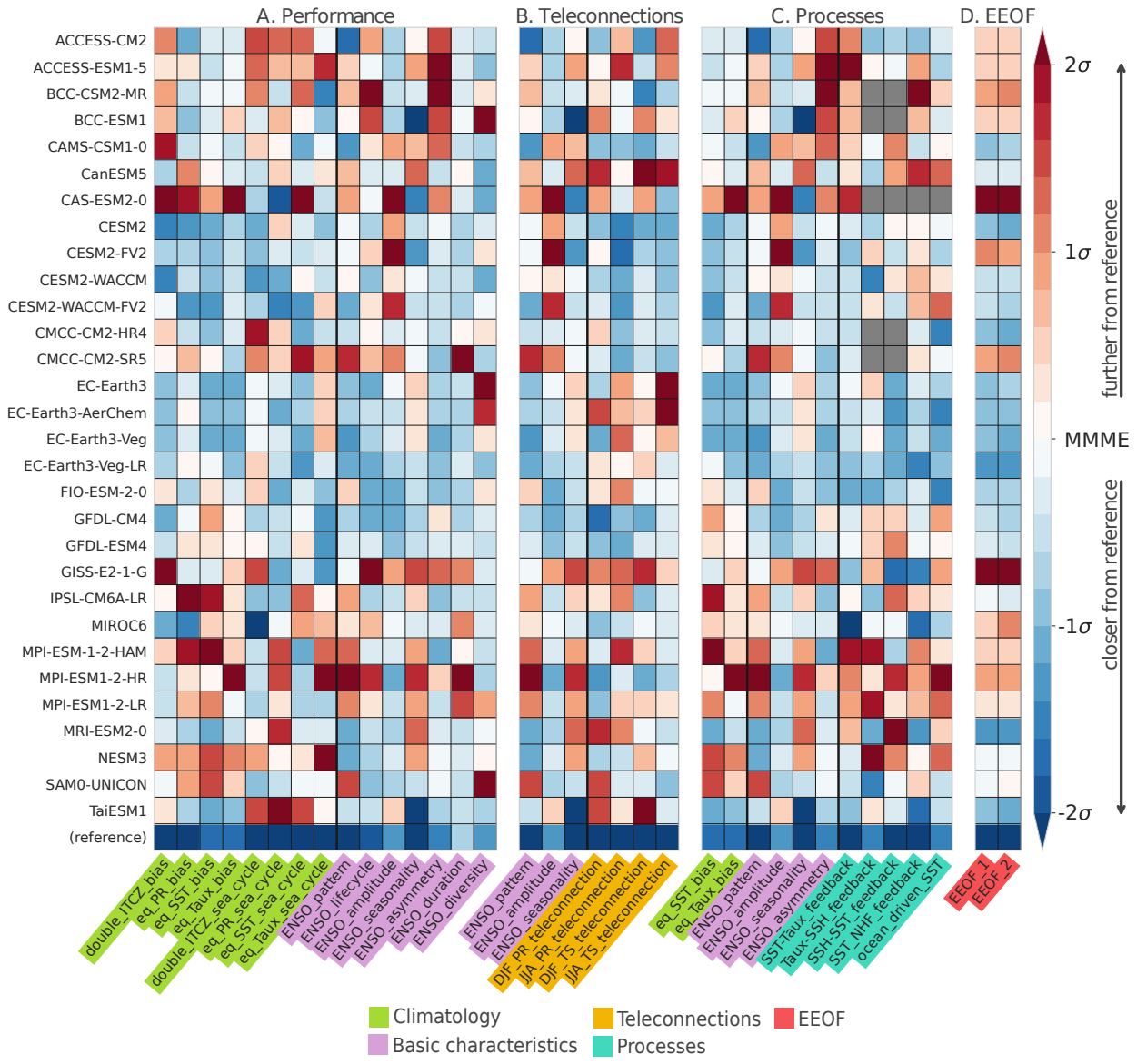

Figure **3-4**.: CMIP6 models' performance on the CLIVAR ENSO Metrics 2021 (CEM2021, Planton et al., 2021) and the couple leading interannual modes of subsurface variability. The figure shows the metric values (anomalies) relative to multi-model mean error (MMME) and normalized by the standard deviation (σ) of each column. The darker the blue (red), the closer (further) the model is to the reference for a given metric. Missing information is indicated in gray. As in Planton et al. (2021), the metrics are grouped according to their application: (A) Performance, (B) Teleconnections, (C) Processes, and (D) EEOF, the last column describing the interannual variability coupled modes. Individual metrics are highlighted in color-codes according to particular categories (refer to Table **B-1** for definitions): background climatology (light green), basic ENSO characteristics (magenta), teleconnections (yellow), physical processes (cyan), or the leading interannual subsurface modes of variability (red, as defined in Section 3.2).

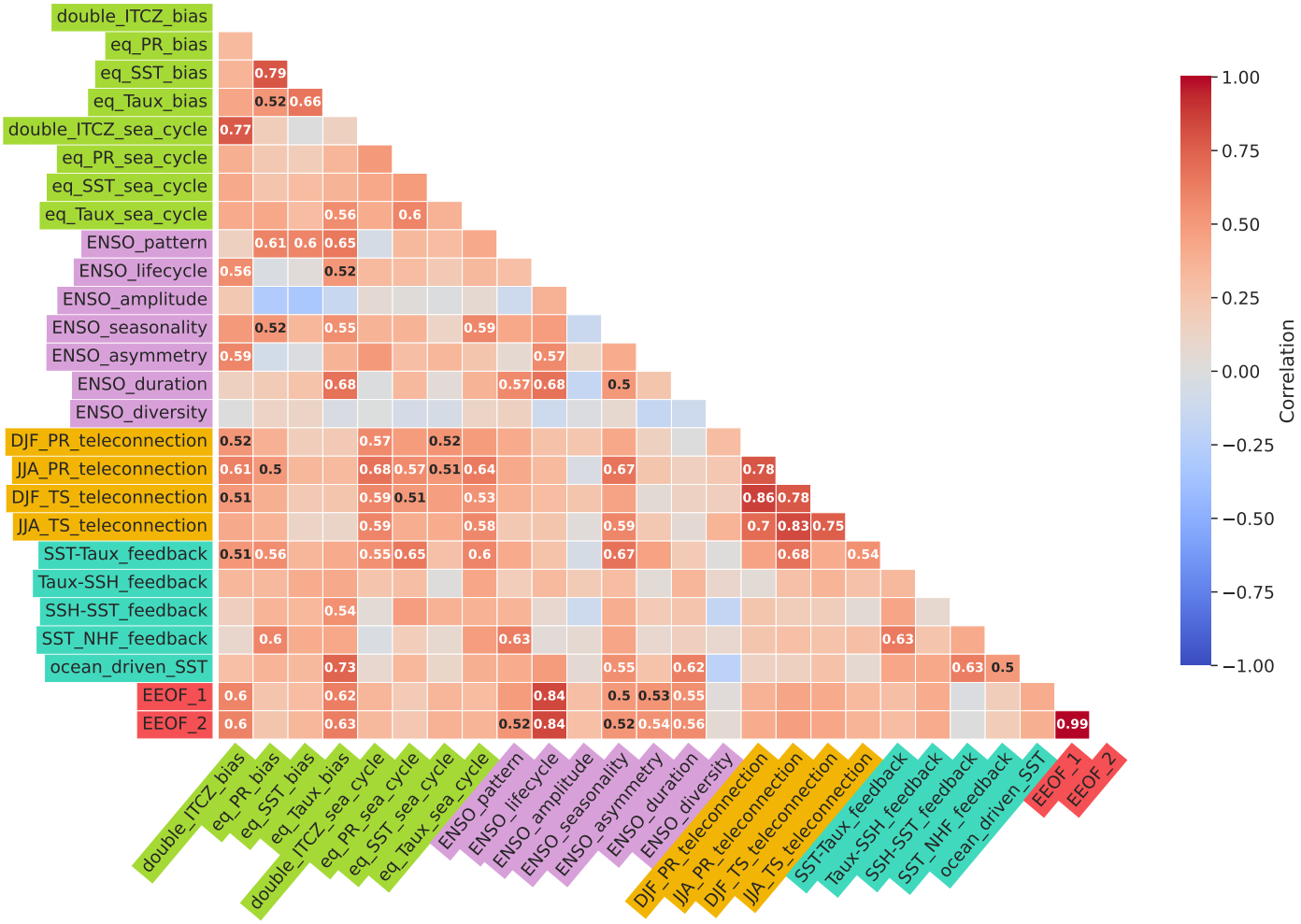

Figure **3-5**.: Intermetric correlations computed across the CMIP6 models. Individual metrics are highlighted in color-codes according to particular categories (refer to Table **B-1** or Table B1 in Planton et al. (2021) for definitions): background climatology (light green), basic ENSO characteristics (magenta), teleconnections (yellow), physical processes (cyan), or the leading interannual subsurface modes of variability (red, as defined in Section 3.2). Correlations greater than ±0.5 had been indicated in the figure.

historical simulation. They suggested that the stronger response of ocean waves against the surface wind during El Niño than during La Niña plays a primary cause of a dominant swing from El Niño to La Niña. The authors also pointed out that interbasin interactions with the Indian and Atlantic oceans also play some role in driving the transition asymmetry. Furthermore, in the historical simulations of the CMIP5, the model-to-model difference in transitions asymmetry was significantly related to that in ocean wave response to surface wind forcing but not to that in the interbasin interactions.

Finally, the fact that the previous analysis is based on only one simulation per model raises questions regarding the robustness of the results. Recently, Lee et al. (2021) tested the sensitivity of the CEM2021 (Planton et al., 2021) to internal variability alone by considering large ensembles of CMIP6 model simulations. They determined that more than 50 ensemble simulations are needed per model to robustly capture the baseline ENSO characteristics and physical processes, at least 12 simulations for the background climatology analysis, and at least 6 for the remote ENSO teleconnections. Consequently, an additional investigation focused on a larger ensemble size is needed to reinforce the robustness of the result presented here.

3.4. Conclusions

This study investigates the coevolution of the subsurface temperature of the Indian and Pacific oceans using observations and CMIP6 historical simulation. An empirical model evaluation approach has been applied to assess the representation of the CMIP6 models in simulating the spatial patterns of the leading interannual modes of subsurface variability. Our results indicate that 23 models from 13 different modeling institutions coincide in reproducing the variability modes described by the reference data, thus, confirming the role of the subsurface interbasin coupling in the ENSO's oscillatory nature and phase transition. In general, models with a nominal resolution of 100 km or more refined achieved high performance in the empirical evaluation. Although, a higher resolution does not guarantee a higher performance, as models of considerably different resolutions achieved similar results.

The ability of the CMIP6 models to reproduce the interannual subsurface temperature modes was compared with their performance of the CLIVAR ENSO Metrics (CME2021; Planton et al., 2021). The diverse range of model performance within each of the metrics indicates the complex nature of the model biases and highlights that it is unlikely to be a single model best suited to all applications. In addition, we found that the representation of the interannual subsurface temperature modes between the two basins is highly correlated with the ENSO life cycle (ENSO_lifecycle) and the climatological structure of the zonal wind stress (eq_Taux_bias). In agreement with previous studies (Ohba and Ueda, 2009; Okumura et al., 2011; Ohba and Watanabe, 2012; Izumo et al., 2010b, 2014; Jourdain et al., 2016; Wieners et al., 2016, 2017; Ha et al., 2017), the coupling between the Indian Ocean and the Pacific Ocean at interannual time scales favors the ENSO phase transition. Therefore, we

suggest that a realistic representation of the interbasin subsurface temperature variability at interannual time scales is necessary for a correct representation of the ENSO phase transition metrics and a better understanding of the ENSO phenomenon. Furthermore, increasing the ensemble size in the empirical evaluation is needed to strengthen the robustness of the results.

4. Conceptual Model

Abstract

Simple conceptual models are valuable tools for investigating theoretical concepts that may serve as sources of insight into ENSO sensitivities and predictability. We study the quasi-periodicity route to chaos arising from a seasonally forced delayed differential model for the El Niño-Southern Oscillation (ENSO). For a specific set of parameter values, the model can produce chaotic solutions that reproduce the irregular behavior observed in the ENSO phenomena. The control parameter is the intensity of the nonlinear coupling (k) between the ocean and the atmosphere, which modulates the dynamical behavior of the system. Furthermore, we included an additional term in the model to investigate the influence of the MJO-induced wind variability over the Western Pacific. The modified model described a similar quasi-periodicity route to chaos as the coupling parameter is increased. The inclusion of the MJO term shifts the dominant periodicities of the numerical solution toward the lower frequencies.

Keywords

El Niño-Southern Oscillation (ENSO); Madden-Julian Oscillation (MJO); Delay Differential Equations; Inter-basin Interaction; Tropical Indo-Pacific; Quasi-periodic route to Chaos; Deterministic Chaos.

4.1. Introduction

The major aspects that give rise to El Niño-Southern Oscillation (ENSO), the dominant mode of climate variability on the interannual time scale, are reasonably well understood (Neelin et al., 1998). Bjerknes (1969) was to first to propose the positive atmospheric feedback on the equatorial sea surface temperature (SST) field via the surface wind stress in generating the ENSO cycle. Although the primary mechanisms are comprehended, ENSO's irregularity behavior presents challenges for its prediction, even at sub-annual (6-12 months) lead times (Cane et al., 1986; Latif et al., 1994).

Much of the theory on the ENSO variability was grounded on the Zebiak-Cane model (Cane and Zebiak, 1985; Zebiak and Cane, 1987), the first coupled ENSO model, and the first dynamical model that produced a successful prediction of El Niño (Cane et al., 1986). The model coupled an ocean numerical model (Cane and Patton, 1984), modified with the addition of a frictional surface layer (Zebiak, 1985), to a Matsuno/Gill atmospheric

model (Zebiak and Cane, 1987). The Zebiak-Cane model was the first to describe the self-sustained coupled oscillation of the ENSO phenomenon and stated that the essential elements of the ENSO are contained within the tropical Pacific (Zebiak and Cane, 1987). It also highlighted the role of the ocean heat content in producing the oscillatory characteristics of the model and the equatorial ocean dynamics in setting the intrinsic time lags that could sustain the oscillation. Furthermore, various simple delay oscillator models were developed and presented a more complete theory for the onset, termination, and cycling nature of ENSO events (Suarez and Schopf, 1988; Battisti and Hirst, 1989; Tziperman et al., 1994; Picaut et al., 1996; Jin, 1997a,b; Weisberg and Wang, 1997). The delayed oscillator models rely on oceanic adjustment (i.e., equatorial waves) and air-sea coupling to establish the phenomenon's cycling nature. Four different types of delayed oscillator models had been proposed, all of which are described extensively on Wang (2001, 2018) and references therein.

Despite that the oscillatory character of ENSO is well comprehended; its irregularity is yet an open question. For example, spectral analysis of the Niño 3.4 time series, as seen in Figure **4-1**, shows power at all frequencies associated with the irregularity but with a preferred time scale of 3 to 5 years, thus, implying that multiple time scales may be involved in ENSO variability (Rasmusson and Carpenter, 1982; Jiang et al., 1995). The irregularity of ENSO has been explained by two different mechanisms: (I) deterministic chaotic behavior associated with large-scale nonlinear dynamics; and (ii) uncoupled atmospheric weather noise

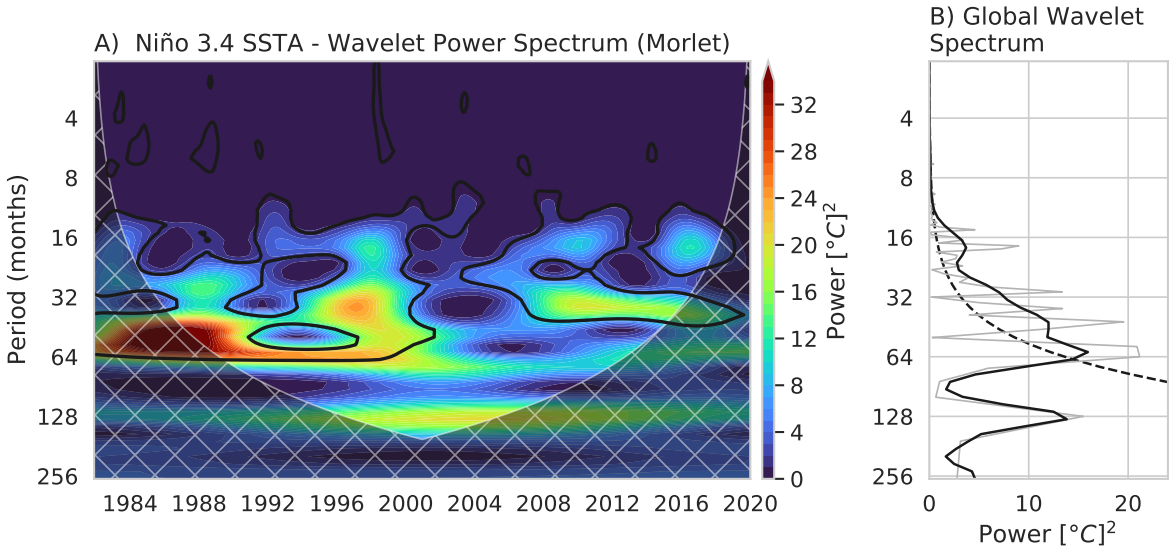

Figure **4-1**.: (A) Niño 3.4 SSTA wavelet power spectrum, the colored contours indicate the power, the thick contour encloses regions of greater than 95% confidence level for a red-noise process. Cross-hatched regions on either end indicate the cone of influence where edge effects due to the finite length of the time series become important. (B) Niño 3.4 SSTA global wavelet spectrum.

(i.e., stochastic forcing, Penland and Sardeshmukh, 1995; Blanke et al., 1997; Eckert and Latif, 1997; Kleeman and Moore, 1997; Moore and Kleeman, 1999; Jin et al., 2007), although these theories are not mutually exclusive. The deterministic chaotic behavior can result from the nonlinear interaction between the seasonal cycle and the ENSO mode (Tziperman et al., 1994, 1995; Chang et al., 1994; Jiang et al., 1995; Jin et al., 1994, 1996) which can also limit ENSO's predictability. This approach can also describe the tendency of El Niño to peak at the end of the calendar year, explaining it through phase-locking to the annual cycle. However, Stein et al. (2010, 2011) also found phase-locking when they employed a linear stochastic model, suggesting that nonlinear dynamics may not be necessary for explaining ENSO's seasonality.

According to the first theory, ENSO's irregularity occurs when the intrinsic ENSO's frequency enters into nonlinear resonant with the seasonal cycle. As the nonlinear coupling of the system is increased, the frequency-locked regimes expand and overlap. As a result, chaos arises as the ENSO oscillator is not able to lock to a single resonance and jumps irregularly between unstable subharmonic solutions of the competing frequencies. This transition is one of the universal routes to chaos and corresponds to the overlapping of nonlinear resonances also known as "Arnold tongues" in parameter space (Jensen et al., 1984; Bohr et al., 1984; Bak, 1986).

Different studies have suggested that westerly wind events (WWEs) as those associated with the Madden-Julian Oscillation (MJO) play a significant role in ENSO dynamics and predictability (Moore and Kleeman, 1999; Kessler and Kleeman, 2000; Boulanger et al., 2004; Zavala-Garay et al., 2005; Zhang, 2005; McPhaden et al., 2006b; Shi et al., 2009; Wang et al., 2011; Chen et al., 2016). WWEs are known for exerting an influence over the ENSO by directly exciting oceanic Kelvin waves over the western and central Pacific that triggers or accelerates the onset of El Niño (Harrison and Schopf, 1984; McPhaden et al., 1988; McPhaden, 1992, 1999; Lengaigne et al., 2002), and by maintaining El Niño conditions when WWEs are positioned over the eastern Pacific (Seiki and Takayabu, 2007). The low-level westerly wind component of the MJO is characterized by synoptic-scale westerly wind events (Zhang, 2005) which have an effective oceanic response because the wind events are spatially and temporally coherent (Kessler et al., 1995; Shinoda and Hendon, 2001; Zhang and Gottschalck, 2002). Furthermore, the Indian Ocean might influence ENSO by a modulation of the Intraseasonal Variability (ISV). Izumo et al. (2010b) noted that zonal wind variability over the western Pacific increases after a negative IOD event. Meanwhile, Yuan et al. (2014) suggested that the eastward movement of MJO is favored during negative IOD events, as the MJO activity is more pronounced over high SSTs, where deep connections can be sustained (Gadgil et al., 1984).

Additionally, as discussed in Chapter 2, the coevolution of the subsurface temperature of the Indian and the Pacific Ocean at interannual at scale suggested an enhancement of the MJO signal over the Western Pacific during the development phase of an El Niño event. In consequence, in this chapter, we study the possible contribution of the Indian Ocean

over ENSO through an atmospheric bridge defined by the interaction of the MJO over the Western Pacific Ocean. First, due to its simplicity, we examine the seasonally force ENSO model of Tziperman et al. (1994) that includes the delayed positive and negative feedback mechanisms through wind-driven oceanic waves. Then, the role of the MJO modulation over the ENSO was analyzed by adding a mathematically formulated term that simulates the seasonal variation of the MJO over the Western Pacific Ocean. In this study, we used the direct numerical integrations and examination of return maps in a low-dimensional to study the effects of both the seasonal cycle and the MJO over the ENSO's periodicity and irregularity. In addition, the dynamical behavior of the models is characterized by the computation of the Lyapunov Exponents for the particular space parameter surveyed.

4.2. The circle map and the transition to chaos

In a similar manner that ENSO's fundamental positive feedback has been studied through conceptual models that capture the fundamental processes of the oscillation (Suarez and Schopf, 1988; Battisti and Hirst, 1989; Tziperman et al., 1994; Picaut et al., 1996; Jin, 1997a,b; Weisberg and Wang, 1997), one-dimensional maps have been used to investigate the nonlinearity in dynamical systems. This simplification has been possible as scaling behavior found in the maps carry quantitatively over to real systems (Jensen et al., 1984).

A simple example where frequency locking occurs is the one-dimensional circle map (Jensen et al., 1984; Bak, 1986), which is an iterative map of the circle to itself. The model is given by:

$$\theta_{n+1} = f\Omega(\theta_n) = \theta_n + \Omega - \frac{k}{2\pi} sin(2\pi\theta_n) \quad (mod\ 1) \tag{4-1}$$

The circle map is nonlinear, and the parameter K controls the intensity of the nonlinearity. The variable θ_n represents the phase of the oscillating system measured stroboscopically at periodic time intervals $t_n = 2\pi n/\omega$, using the frequency of the external force ω (Jensen et al., 1984). θ_{n+1} denotes the angle of the location of the nth iterations of the circle and Ω represents the frequency of the system in the absence of nonlinear coupling K. The mod operator ensures that θ_{n+1} remains between the valid unit interval by adding or subtracting 1 to its values. The full transition of the quasi-periodic route to chaos is obtained by varying both the non-linearity parameter K and Ω. As one varies one of the two parameters the system will pass through regimes that are phase-locked and regimes that are not until the chaotic behavior is encountered.

A diagnostic tool for the transition to chaos in the circle map is the winding number (W), which represents the mean number of rotations per iteration, that is to say, the frequency of the dynamical system. To scan for frequency locked regions, one varies Ω for a fixed K and

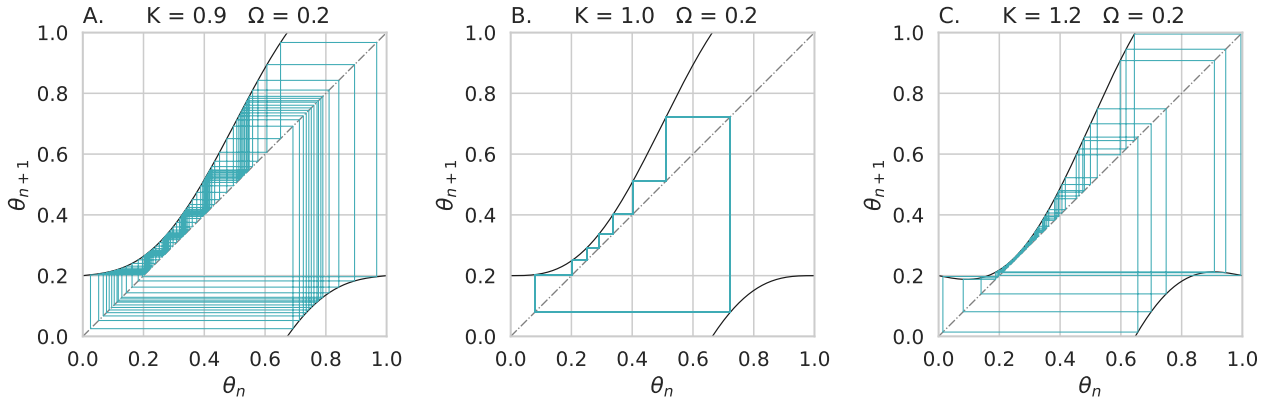

Figure **4-2**.: Return map of the circle map for $\Omega = 0.2$ and $K = 0.9$, 1 and 1.2.

searches for rational numbers. The winding number is defined as:

$$W = \lim_{n\to\infty} \frac{1}{n}(\theta_n - \theta_0) \tag{4-2}$$

where θ_n is calculated without taking modulo 1. Under different iterations, the variable θ_n could converge to a series that is either periodic, quasiperiodic, or chaotic. A periodic series is the result of the nonlinear resonance between two frequencies, hence $\theta_{n+q} = \theta_n + p$ and the frequency of the system (W) is given by the rational number p/q. Moreover, a quasi-periodic time series occurs when the winding number is irrational. If the series is chaotic, the winding number is not defined. When the nonlinearity coupling K is between 0 and 1, the map is monotonic and the behavior is periodic o quasi-periodic (Figure **4-2**-A). At K = 1, the map reaches an inflection point at $\theta_{n+1} = 0$, and the probability of the winding number to be rational is close to one (Figure **4-2**-B). For $K > 1$ the map is no longer invertible resulting in chaotic trajectories (Figure **4-2**-C).

In the circle map, the transition to chaos occurs as a function of the two parameters K and Ω shown schematically by Figure **4-3**-B. The wedge-like areas are regimes where W assumes rational values called Arnold's tongues. When K is close to zero, all the intervals are very small and the probability of W being rational is almost zero. However, with increasing nonlinear coupling the widths of all the phase-locked intervals increases. Eventually, for $K = 1$ the Arnold's tongues cover a large portion of the Ω axis and the probability of the winding number being rational is almost 1 (Figure **4-3**-A). At $K > 1$ the resonance regions overlap generating a chaotic behavior as the system jumps between competing resonances. Between jumps, the system still tends to be locked to the external frequency for some interval of time (Tziperman et al., 1995).

The return map (θ_{n+1} vs θ_n, Figure **4-2**) represents another useful diagnostic of the transition to chaos. It occurs at the critical point $K = 1$ where the monotonicity is lost and

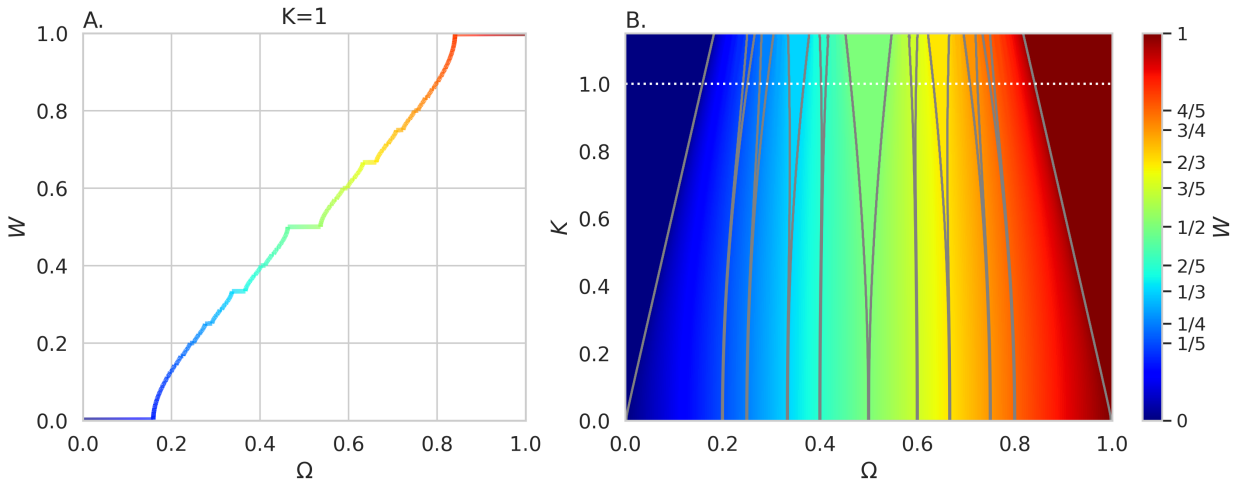

Figure **4-3**.: (A) Winding number W vs Ω for the circle map at $K = 1$, also known as the Devil's staircase. (B) Schematic Diagram of Arnold Tongues. The Devil's staircase is the cross-section of the Arnold Tonges diagram at $K = 1$.

$\partial\theta_n/\partial\theta_{n-1} = 0$.

4.3. The conceptual model

The delayed oscillator models pivot around the idea that the strongest atmosphere-ocean coupling takes place in the middle of the Pacific Ocean (Figure **4-4**). In that respect, a variation in the wind stress field induced by a positive SST perturbation in the center of the Pacific generates downwelling Kelvin waves that travel east and westward-propagating upwelling Rossby waves. As a result, the downwelling Kelvin waves enhanced the warming of the coast of South America, initiating a warm event. Meanwhile, the Rossby waves reflect on the western boundary of the Pacific Ocean as upwelling Kelvin waves, thus, creating the delayed negative feedback that will reverse the ENSO phase. Nevertheless, It is worth noting that western boundary reflection is not as efficient as the model suggests. The western boundary is quite irregular and, in practice, results in substantial scattering instead of simple reflection. Zang et al. (2002) found that only 30% of the energy of the Rossby waves is reflected as a Kelvin wave over the western boundary.

The conceptual model proposed by Tziperman et al. (1994) incorporates such a delay process and is described by the following equation:

$$\frac{dh(t)}{dt} = c_1 A\left(h\left(t - \frac{L}{2C_K}\right)\right) - c_2 A\left(h\left(t - \frac{L}{2C_R} - \frac{L}{C_K}\right)\right) + c_3 cos(\omega_a t) \tag{4-3}$$

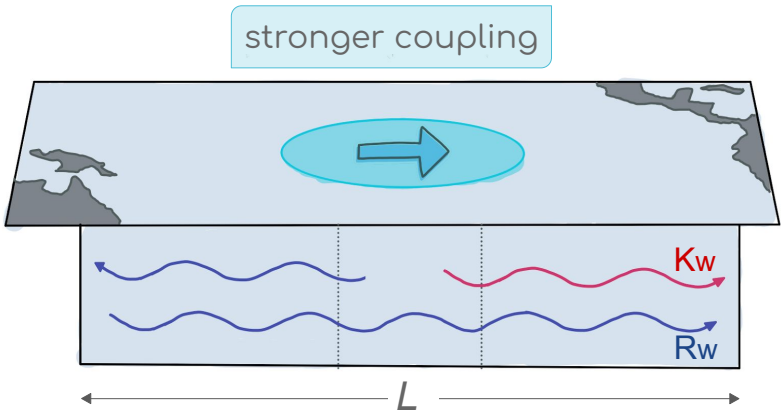

Figure **4-4**.: Schematic of the delayed oscillator mechanism. Strong coupling between the atmosphere and the ocean over the central Pacific allows wind disturbances to create ocean waves. The wind forces a downwelling Kelvin wave (K_w, red ripple) that deepens the thermocline in the eastern Pacific. And an upwelling Rossby wave (R_w, blue ripple), which after bouncing off the western edge of the ocean, decreases the depth of the thermocline in the eastern Pacific.

where $h(t)$ represents the thermocline depth deviation from the seasonal depth values at the eastern boundary, t is time, L is the basin width, and ω_a expresses the annual frequency of the seasonal forcing. The first term on the right-hand side of Equation 4-3 represents the wind-forced Kelvin wave that travels eastward at a speed C_K. The second term denotes the Rossby wave that travels westward at a speed C_R and is reflected as a Kelvin wave off the western boundary.

The forcing function $A(h)$ relates wind stress to SST and SST to thermocline depth. Munnich et al. (1991) proposed a forcing function $A(h)$ tailored to rule out unrealistic behavior and fashioned after the shape of the tropical thermocline:

$$A(h) = \begin{cases} b_+ + \frac{b_+}{a_+}\left\{tanh\left[\frac{ka_+}{b_+}(h-h_+)\right]-1\right\}, & if\ h_+ < h, \\ kh, & if\ h_- \le h \le h_+, \\ -b_- - \frac{b_-}{a_-}\left\{tanh\left[\frac{ka_-}{b_-}(h-h_-)\right]-1\right\}, & if\ h < h_-, \end{cases} \tag{4-4}$$

Following Munnich et al. (1991) $a_\pm > 1$ and

$$h_+ = \frac{b_+}{ka_+}(a_+ - 1), \quad h_- = \frac{b_-}{ka_-}(a_- - 1) \tag{4-5}$$

The function $A(h)$ is a linear piece inserted smoothly between two $tanh$ segments where the parameters $b_\pm > 1$ impose the upper and lower limits of the function, and $a_\pm > 1$ control the curvature of $A(h)$, i.e., how rapidly $A(h)$ approaches the asymptotic values $b_\pm > 1$ (Figure **4-5**). The parameter k controls the slope of $A(h)$ at $h = 0$ and modulates the strength of the

nonlinearity. As shown by Tziperman et al. (1994) k is a key parameter controlling the model's dynamical behavior.

For the integration of the conceptual model, we used the four-order Runge-Kutta algorithm adapted for delayed differential equations. Then the analysis of the transitions to chaos in the model is done by running the equations with different parameter values and examining the $h(t)$ time series. The model time series is obtained by integrating the model for 400 years with a time step of 5 days. The first 50 years of the time series were removed to dissipate the transient response of the model to the initial conditions. The values used in the numerical simulation are reported in Table **4-1**.

Parameter	**Description**	**Numerical value**
dt	Time step	5 days
L	Basin width	1
ω_a	Frequency of the annual cycle	$2\pi/365$
C_K	Kelvin wave speed	$1/72$ days^{-1}
C_K	Rossby wave speed	$1/216$ days^{-1}
$a_\pm$	Control parameters of the curvature of $A(h)$	1
b_-	Limit of $A(h)$ as $h \to -\infty$	-1
b_+	Limit of $A(h)$ as $h \to +\infty$	2
$c_1,\ c_2$	Magnitude of the waves' feedback	$c_1 = 1/180,\ c_2 = 1/120$
c_3	Magnitude of the periodic forcing	$c_3 = 1/138$

Table **4-1**.: Glossary of model's parameter.

Following Tziperman et al. (1994, 1995) the phase space ($h(t+\tau)$ vs $h(t)$) for the different

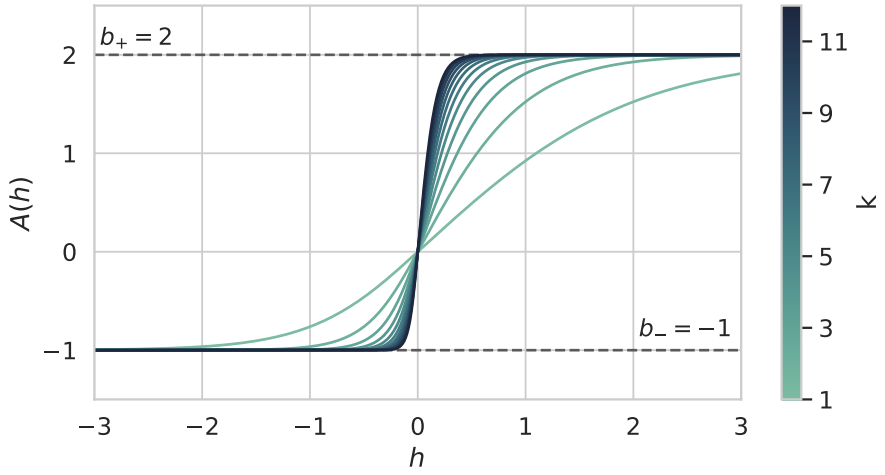

Figure **4-5**.: Forcing function $A(h)$, representative of ocean-atmosphere coupling as described by Equation 4-4.

iterations of the model was obtained using "delay coordinates" with a delay time τ of 1 year, Equation 4-6. The annual subsampling of the time series results in a simple closed curve in the phase space. Then, the return map can be computed by calculating the angle θ_n from the center of the attractor to the point $(h(t), h(t+\tau))$ in the phase space diagram (refer to Tziperman et al., 1995, Figure 3).

$$h(t) = [h(t), h(t+\tau),\ ..., h(t+(m-1)\tau)] \tag{4-6}$$

Tziperman et al. (1994) reported four dynamical regimes exhibited by the model (Equation 4-3) as k, the nonlinear coupling, is increased. The first one is a periodic behavior governed by the annual forcing Ω_a (Figure **4-6**-A) with the phase-space converging to an attractor for small values of k. As k is further increased, the model describes an irregular quasi-periodic behavior characterized by the emergence of a second frequency (Ω_n), that of the Tropical Pacific's ocean-atmosphere system (Fei-Fei Jin and Neelin, 1993; Neelin et al., 1998) which emerges from the delayed ocean adjustment with the preferable 3-4 year period (Zebiak and Cane, 1987). The two frequencies are not in accordance with one another, which results in a quasi-periodic time series. The resulting oscillation is irregular but not chaotic, and the power spectrum displays two dominant frequencies with several subharmonics (Figure **4-6**-B).

For even higher values of k, the system becomes frequency-locked. The second frequency shifts to a rational multiple of the driving annual frequency: $\Omega_n = \Omega_a p/q$, with p and q integers. The oscillator is subjected to a nonlinear resonance between the driving annual frequency Ω_a and the internal oscillatory frequency Ω_n. The result is a periodic time series (Figure **4-6**-C) in the parameter regimes (k vs Ω_a) corresponding to a mode-locked solution of Arnold's tongues. Lastly, for certain values of k, the system becomes chaotic (Figure **4-6**-D). The chaotic behavior is caused by the overlapping of the resonances and the irregular jump of the system between the frequency-locked solutions.

4.4. Implementation of the MJO forcing in the conceptual model

Numerous studies (Kessler et al., 1995; Kessler and Kleeman, 2000; Hendon et al., 1999; Shinoda and Hendon, 2001; Zhang and Gottschalck, 2002; Zhang, 2005; Zavala-Garay et al., 2005; Hendon et al., 2007) suggested that the Madden-Julian Oscillation (MJO, Madden and Julian, 1971, 1972), the dominant component of the intraseasonal variability in the tropical atmosphere (Zhang, 2005), may influence the ENSO variability and predictability. MJO constantly interacts with the ocean, thereby influencing the evolution of ENSO. Over the equatorial Indian and Western Pacific oceans, an MJO event features an eastward propagating deep convection center flanked at the surface by anomalous easterly winds to the east and

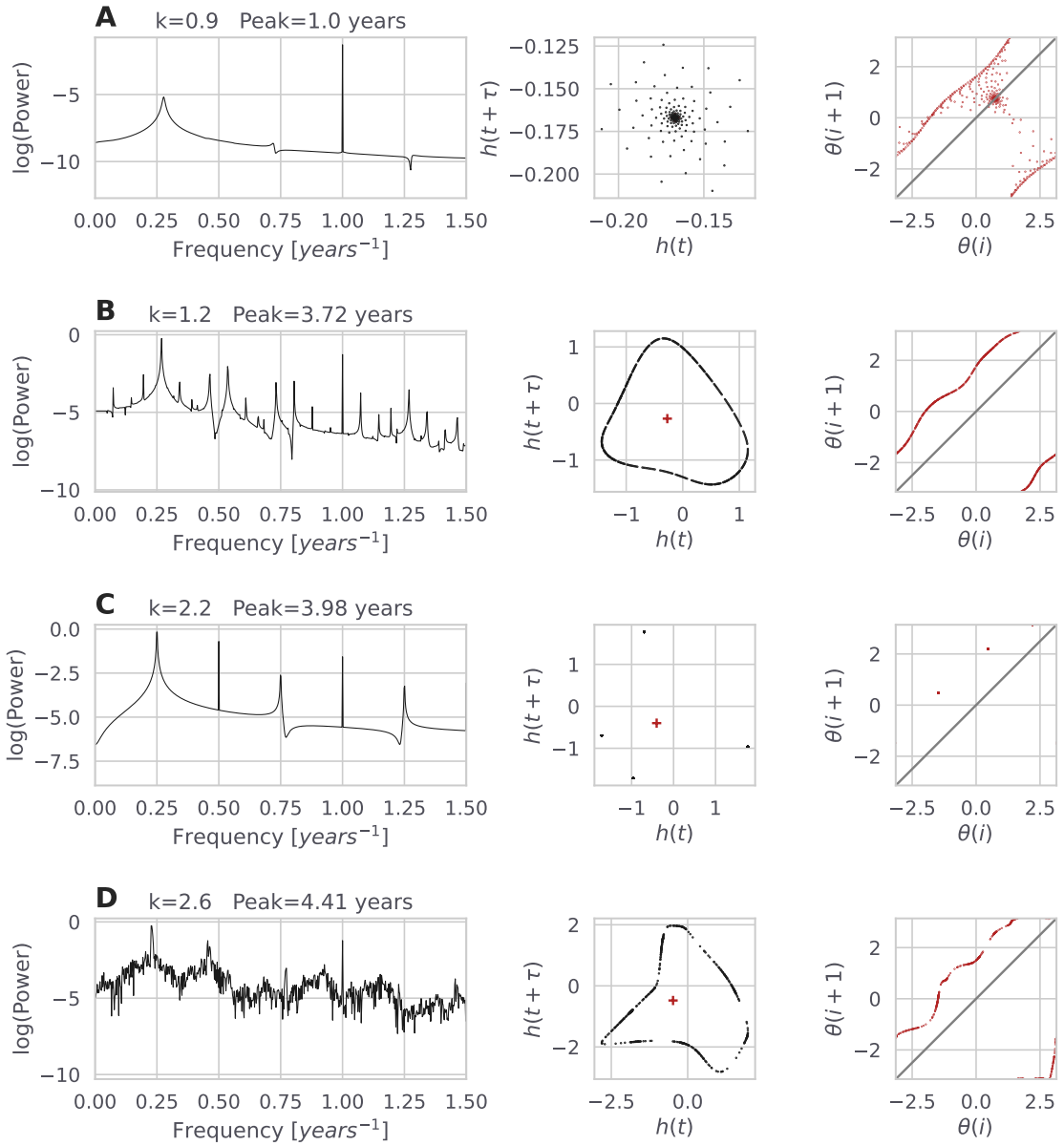

Figure **4-6**.: Integration of the conceptual model (Equation 4-3) for the selected parameters in Table **4-1**. Shown are the Fourier spectrum (left column); a phase-space diagram (middle column); return map (right column) of each run. The four cases shown are **(A)** $k = 0.9$, **(B)** $k = 1.2$, **(C)** $k = 2.2$; and **(D)** $k = 2.6$.

anomalously strong westerly winds at the west (Zhang, 2005). By triggering Kelvin waves over the western Pacific Ocean, individual MJO events influence the thermocline depth and SST that affect the ocean currents and heat fluxes.

Consequently, we introduced a new term in the delayed oscillatory model to investigate the interaction between the high-frequency atmospheric variation of the MJO and the slow ocean dynamics of ENSO. The last term in Equation 4-7 represents the effect of the MJO-forced Kelvin waves generated at the western Pacific influencing the thermocline depth at the eastern coast. The expression is multiplied by (I) a periodic Gauss function that imitates the seasonal cycle of the MJO with larger amplitudes in boreal winter and spring (Zhang, 2005); and (II) a periodic piecewise function $M(t)$ (Equation 4-8) that determines the overall delayed effect of the MJO-induced ocean waves.

$$\frac{dh(t)}{dt} = c_1 A\left(h\left(t - \frac{L}{2C_K}\right)\right) - c_2 A\left(h\left(t - \frac{L}{2C_r} - \frac{L}{C_K}\right)\right) + c_3 cos(\omega_a t) + c_4 A\left(h\left(t - \frac{L}{C_K}\right)\right)\left[(\alpha - \beta) * exp\left(-\frac{\{[(t+\varphi)\ mod\ N_1] - B\}^2}{2C^2}\right) + \beta\right] * M(t\ mod\ N_2) \tag{4-7}$$

$$M(t) = \begin{cases} -0.8, & if\ t < 25, \\ 1, & if\ 25 \leq t < 45, \\ 0, & if\ t \geq 45, \end{cases} \tag{4-8}$$

The piecewise function $M(t)$ reproduces an idealized effect of an MJO event crossing over the western Pacific Ocean. First, the MJO-induced surface easterlies winds generate an upwelling Kelvin wave. Then, after the transit of the MJO-convective center over the western boundary, the strong surface westerlies winds will induce a downwelling Kelvin wave followed by a period of inactivity. Thus, the net effect of Equation 4-8 represents the sequence of asymmetrical surface wind (usually MJO-induced westerlies are more vigorous than easterlies, Zhang, 2005) followed by a dormancy period. We selected a periodicity of 50 days, although the MJO does not regularly oscillate, being highly episodic or discrete (Salby and Hendon, 1994; Zhang, 2005).

Figure **4-7**-A displays the shape of the periodic Gauss function throughout the time integration with its bell center at the beginning of the year, supposing that t_0 is the beginning of the calendar year. Meanwhile, the idealized cycling nature of the MJO is depicted in Figure **4-7**-B. This was mathematically formulated by adding a seasonally varying frequency of 50 days (Equation 4-8), where the first 25 days correspond to the effects of the easterlies followed by 20 days of stronger westerlies and an inactivity period of 5 days. The complementary numeral values used for the integration of Equation 4-7 are reported in Table **4-2**.

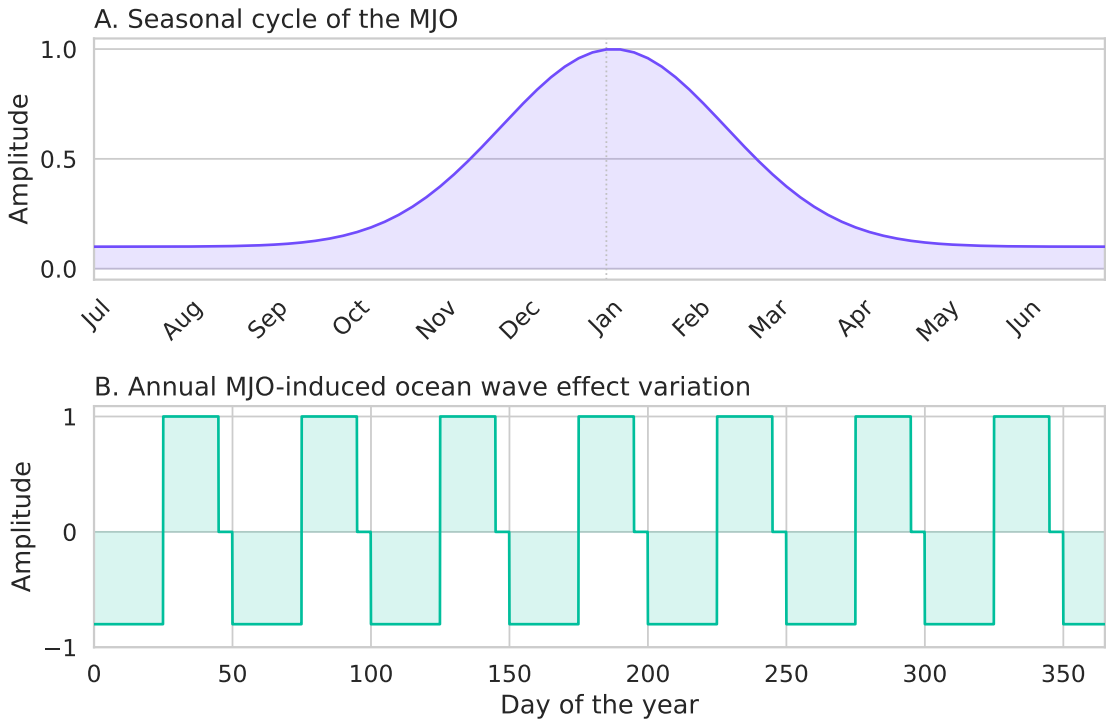

Figure **4-7**.: Idealized MJO seasonal cycle (A) and Annual MJO-induced ocean wave effect variation (B) over the Western Pacific. (A) represents the shape of the Gaussian function multiplying the last term in Equation 4-7. The bell controls the amplitude of the MJO-forced Kelvin wave (c_4) thought out the time integration, supposing that t_0 is the beginning of the calendar year. MJO has larger amplitudes during boreal winter and spring. (B) illustrates the delayed contribution of the MJO-induced ocean waves due to surface wind variability.

Parameter	Description	Numerical value
c_4	Magnitude of the MJO-forced wave's feedback	$c_4 = c_1/2$
φ	Phase-shifting of the Gauss bell (i.e., translation on the time axis)	180 days
N_1	Mod operator parameter. Controls the peridiocity of the gaussian function	365 days
N_2	Mod operator parameter. Controls the peridiocity MJO-induced delayed effect	50 days
α	Gaussian bell amplitude	0.9
β	Vertical-shifting of the Gauss bell (i.e., translation on the y axis)	0.1
B	Gaussian bell center	180 days
C	Gaussian bell width	45 days

Table **4-2**.: Glossary of complementary model's parameter for the MJO interaction.

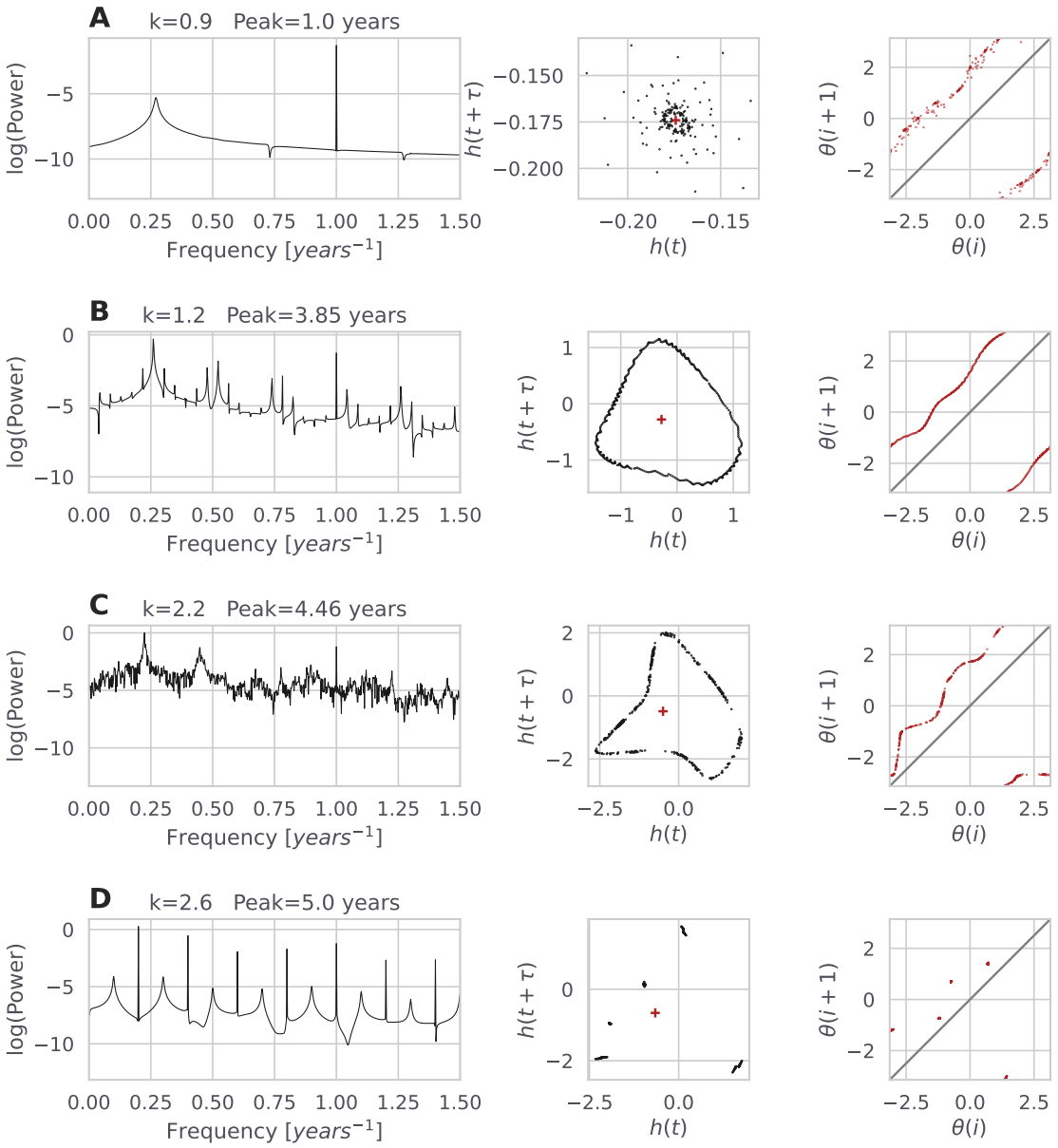

Figure **4-8**.: Same as Figure **4-6** but for the integration of the conceptual model (Equation 4-3) for the selected parameters in Table **4-1**. The four cases shown are **(A)** $k = 0.9$, **(B)** $k = 1.2$, **(C)** $k = 2.2$; and **(D)** $k = 2.6$.

Figure **4-8** shows the results of the integration of Equation 4-7 for the same set of values of k as in Figure **4-6**. In general, the behavior is very similar, although as the non-linearity k increases, the longer the periods are, thus emphasizing lower frequencies. Interestingly, chaotic behavior is obtained for a lower value of the non-linearity parameter ($k = 2.2$) compared to the previous model with a much broader ENSO-related spectral peak. Earlier different authors (Blanke et al., 1997; Chang et al., 1996; Jin et al., 1996), simulating the impact of WWB/MJO as a stochastic forcing to their models, also found spectral peak consistent with the ENSO that becomes chaotic at the higher coupling. Particularly, Blanke et al. (1997) observed a broadening of the ENSO spectral peak in a hybrid coupled model when the stochastic winds stress component was added to the simulation in comparison to the run when noise is absent.

4.5. Chaotic dynamics

One commonly used method for studying chaotic dynamics is the computation of the Lyapunov Exponents (LEs). These quantify the exponential divergence of initially close state-space trajectories and estimate the amount of chaos in a system (Rosenstein et al., 1993). Quantitatively, any two trajectories $x(t) = f^t(x_0)$ and $x(t) + \delta x(t) = f^t(x_0 + \delta x_0)$ in the phase space that start out very close to each other separate exponentially with time. Their sensitivity to initial conditions can be calculated as:

$$\|\delta x(t)\| \approx e^{\lambda t} \|\lambda x_0\| \tag{4-9}$$

where λ, the mean rate of separation of trajectories of the system, is called the leading Lyapunov exponent. Positive LEs indicate exponential divergence of neighboring trajectories, which are the essential attribute of chaotic attractors (Parlitz, 2016). A negative LE indicates that the trajectories are contracting asymptotically along the corresponding orbit; meanwhile, stable points get assigned a $-\infty$. For sufficiently long time series, it is possible to directly assess the local diverge of trajectory segments in the reconstructed state space (Rosenstein et al., 1993; Parlitz, 2016). These direct methods estimate the largest LE and give graphical feedback to confirm the exponential divergence or convergence (Parlitz, 2016).

Here we estimate the largest LE for a range of the coupling parameter k for both models analyzed in this chapter using the technic described by Parlitz (2016). Figure **4-9** shows a comparison of (A) T the dominant periodicity and (B) the LEs for the time series $h(t)$ obtained while we vary the coupling parameter k. We confirm the chaotic behavior for different range windows of k for both models according to the results.

For small values of k, Tziperman et al.'s model is characterized by neutral stability ($\lambda \approx 0$) and an increasingly dominant period. After $k \approx 1.31$, the systems reach a chaotic behavior, and the dominant period stabilized around four years. Henceforward, there is an oscillating window of chaotic and periodic behavior, after which the system reaches a long stable

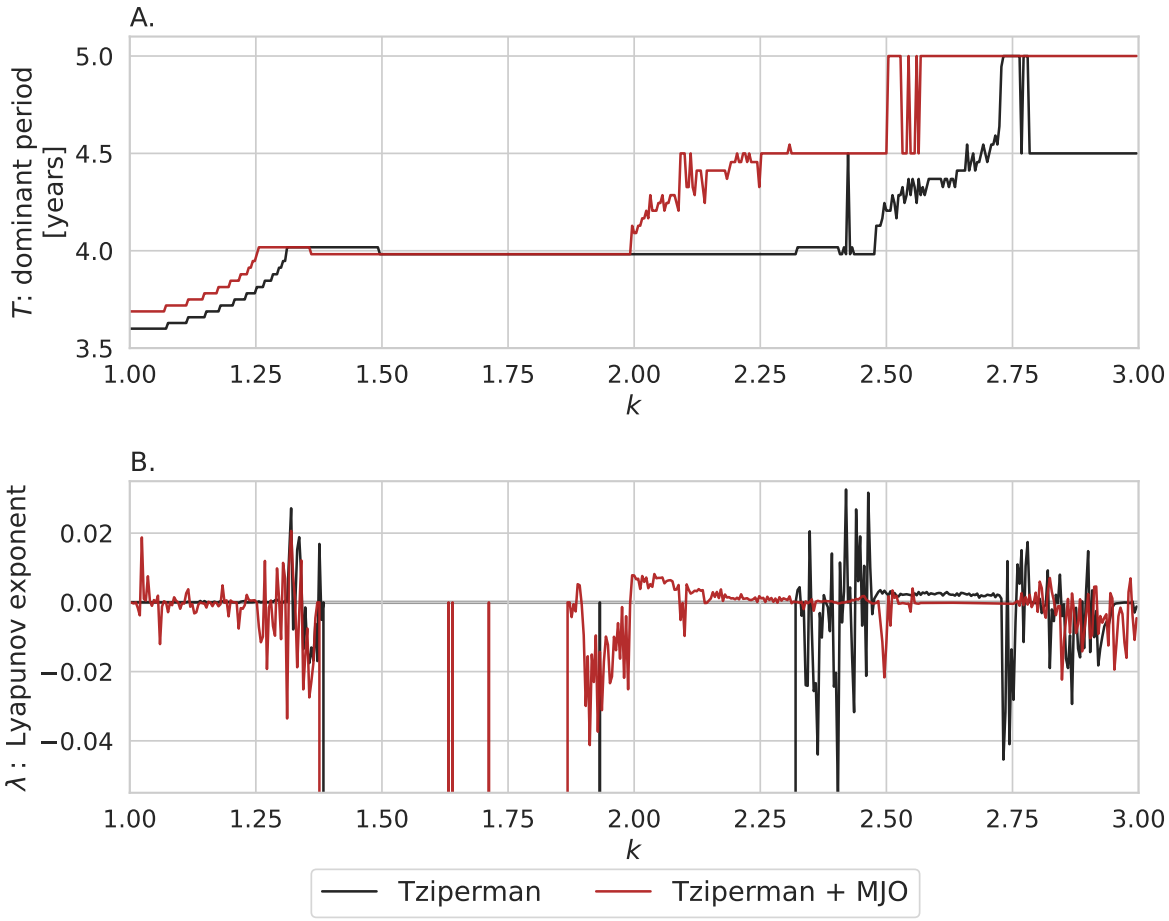

Figure **4-9**.: (A) Dominant periodicity of $h(t)$ time series for different values of the k-parameter. (B) Numerical estimation of the Lyapunov exponent for different values of the k-parameter.

condition window ($\lambda = -\infty$), although the dominant period remains practically constant. Between $2.38 < k < 2.48$, there is a window of alternating chaotic/periodic behavior, where the dominant periodicity does not suffer many alterations besides a particular peak where it reaches 4.5 years. Then, for the range where $2.48 < k < 2.73$, the system arrives at a chaotic window where $\lambda > 0$ and the dominant periodicity rapidly increases. Finally, for $k > 2.73$, there is an alternation between chaotic and periodic behavior, where the de dominant period peaks a maximum of 5 years before settling around 4.5 years.

The MJO-forced conceptual model describes a similar behavior to Tziperman et al.'s model but archives a higher dominant period for lower values of the coupling parameter k, thus emphasizing the lower frequencies as Figure **4-8** also suggested. For small values of k, the system is characterized by alternating chaotic and periodic solutions, which rapidly reach a long stable condition simultaneous with Tziperman et al.'s model. Nevertheless, the system achieves chaotic behavior earlier with a sustained chaotic window ($2 < k < 2.09$),

which slowly drops, alternating between chaotic, neutral, and periodic solutions. After the periodic solution window ($2 < k < 2.5$), the dominant period rapidly increases until it fixes on 4.5 years. Henceforth the dominant period reaches a maximum of five years, and the system describes neutral stability, with some dropback of T at 4.5 years for particular values of k where $\lambda > 0$. Finally, for $k > 2.75$, the model oscillates between chaotic, neutral, and periodic solutions, without altering the dominant periodicity of five years.

Jin et al. (1996), also studying the interaction of ENSO with the seasonal cycle, examined the parameter-space to localize the chaotic and frequency-locked regimes in an intermediate coupled model (refer to Jin et al., 1996, Figure 6). Although their results are strongly model-dependent, they concluded that the frequency-locked solutions dominated most of the space surveyed compared to the chaotic regimes. In agreement with Jin et al. (1996) but for the models and the particular parameter-space analyzed, we also observed the dominance of frequency-locked regimens for both models.

We also performed another experiment where the magnitude of the periodic seasonal forcing (C_3) was set to zero. The goal was to determine if a chaotic behavior would emerge by only exciting the system with the modulation of the idealized MJO-forcing. Our results indicated that for the range of the coupling parameter surveyed ($1 < k < 3$), the system did not achieve chaotic behavior (results not shown).

4.6. Conclusions

In this chapter, we investigated the influence of the seasonal cycle and the contribution of the MJO on the ENSO using a simple nonlinear seasonally forced model that simulates the phenomenon. Previously, numerous studies indicated that ENSO's irregularity might be a result of deterministic large-scale nonlinear dynamics characterized by the quasi-periodicity route to chaos (Tziperman et al., 1994, 1995). Here, by including additional seasonally varying frequency representative of the MJO, we also obtained a quasi-periodicity route to chaos as the ocean-atmosphere coupling parameter increased. Furthermore, the modified model showed the irregularity and interannual time period oscillation. Additionally, the inclusion of the MJO term in the model also modified the dominant periodicity of the numerical solution emphasizing the lower frequencies. Therefore, although ENSO irregularity and oscillatory behavior could be explained by intrinsic elements contained within the tropical Pacific (Zebiak and Cane, 1987; Tziperman et al., 1994; Jin et al., 1994; Tziperman et al., 1995), the inclusion of the phenomena like MJO may affect its timing and its strength. However, in the case of Tziperman et al.'s model, the idealized MJO-forcing is not enough to force a chaotic behavior when the seasonal forcing is absent.

For the parameter space surveyed and similar to Jin et al. (1996)'s discussion, we observed the predominance of the frequency-locked solutions ($\lambda < 0$), representing the 67 and 65.45% for Tziperman et al.'s model and the model that included the MJO-forcing parameter, respectively. Additional experiments can be performed to complete the present study; for

instance, the simultaneous variation of the parameters that intervene in the idealized MJO forcing, such as C_4 and the coupling parameter k, can give further inside into the dynamical behavior of the system. Also, the inclusion of an interannual modulation of the MJO signal, as suggested in Chapter 2, could complement the study of the ENSO sensitivities to the coupling of the subsurface temperature of the Indian and the Pacific Oceans.

Likewise, decadal variations in the state of the ocean-atmosphere coupled mode can also alter the results and favor the phase-locking (Kirtman and Schopf, 1998). In the case of our highly idealized conceptual model, the asymmetric forcing function $A(h)$ is parametrized around a mean constant state of the Pacific system. Thus, changing the mean state can also alter the results. Although, as stated by Zebiak and Cane (1987), the essential elements of the ENSO are contained within the tropical Pacific, teleconnections are possible. And both atmospheric noise and transition to chaos (through the interaction with the seasonal forcing) may contribute to ENSO's irregularity. The results support the hypothesis that intraseasonal variability is not an essential component of ENSO (Zebiak, 1989), though it can interact constructively with the ENSO cycle through nonlinear ocean dynamics (Kessler and Kleeman, 2000). The overall results are significant because the addition of the MJO component to the model can modify the strength of ENSO (compare the second column of Figure **4-6** and Figure **4-8**) and also its periodicity. Furthermore, the use of more comprehensive technics as bifurcation analysis (Keane et al., 2016) and pullback attractors (Chekroun et al., 2018) can provide valuable insight into the dynamic processes involved in its chaotic behavior. Therefore, the study represents the first step for future work in this direction.

5. Conclusions

The present work constitutes an integrated study about the influence of the Indian Ocean on ENSO, where we seek to understand the coupled interaction that could provide information beyond the spring predictability barrier. Our research is grounded on previous investigations that suggested that interannual SST variability over the Indian Ocean (IOBM and/or the IOD) can influence the following year's ENSO, as well as favor its phase transitions (Kug and Kang, 2006; Izumo et al., 2010b, 2014; Ha et al., 2017). Here a variety of data sources, including several reanalyses, satellite databases, and CGCMs historical simulations, were used to study the covariability of the Indian and the Pacific oceans, making a particular emphasis on the subsurface variability.

A composite technic gave us an initial hint about an eastward propagating subsurface signal that originated over the Indian Ocean before the onset of the most significant El Niño events. This idea was supported by lead-lag correlation analysis, which suggested that a signal that is first developed in the subsurface of the eastern Indian Ocean gets amplified over the Western Pacific at interannual time scales. Next, we used an empirical approach to diagnose the leading interannual modes of subsurface variability, which described a close relationship with the ENSO cycle and its phase transition through ocean wave dynamics. This analysis showed that the strong covariability of the Indian and Pacific oceans is closely related to the subsurface ocean variability across the two tropical oceans. Previous investigations proposed that the IOBM/IOD or the combined effect of both phenomenons promotes a systematic ENSO phase transition, thus enhancing ENSO's biennial time scale (Ohba and Ueda, 2009; Okumura et al., 2011; Ohba and Watanabe, 2012; Izumo et al., 2010b, 2014; Jourdain et al., 2016; Wieners et al., 2016, 2017; Ha et al., 2017). Our results suggest that the ENSO phase transition and its biennial tendency are strongly related to the coupled ocean waves dynamics across the two oceans represented by the consecutive alternation of the leading couple EEOF modes.

Moreover, when we compared the ability of state-of-the-art CGCMs in representing the leading modes of subsurface variability with their performance of the CLIVAR ENSO Metrics (CME2021; Planton et al., 2021) we found a significant correlation with the bias metrics of the ENSO life cycle and event duration. For instance, the first metric, also known as the ENSO transition asymmetry (Larkin and Harrison, 2002; Ohba and Ueda, 2009; McPhaden and Zhang, 2009; Okumura and Deser, 2010), describes the tendency of El Niño events to terminate quickly after their mature phase and shift into a cold phase by the following year. In contrast, La Niña tends to persist throughout the second year and reintensifies in winter.

Complementary, the ENSO duration metric assesses the number of months during which El Niño/La Niña SSTA persists. According to Xian et al. (2019) two-thirds of El Niño events terminate after one year, while nearly half of La Niña events last two years or longer. It has been argued that a correct representation of the subsurface covariability between the two ocean basins translates into a better representation of the ENSO's life cycle metrics, as both metrics are closely related to the phase transition.

Previous studies focused on interannual SST variability linked the influence of the Indian Ocean onto ENSO through an atmospheric bridge (Clarke and Van Gorder, 2003; Izumo et al., 2010b, 2014, 2016; Jourdain et al., 2016; Wieners et al., 2016, 2017; Ha et al., 2017; Cai et al., 2019) or an oceanic connection Yuan et al. (2011, 2013). Instead, we choose to investigate a possible atmospheric mechanism coupled with subsurface covariability between the two oceans. First, our results showed that the accumulation of positive subsurface temperature anomalies over the eastern Indian Ocean promotes the intensification of the Walker Circulation, enhancing the low-level convergence over the Indo-Pacific region and the subsequent build-up of heat content. Then, the following expansion of the westerly anomalies from the Indian Ocean into the Western Pacific, in line with previous investigation (Izumo et al., 2010b; Wieners et al., 2016, 2017; Wang et al., 2019; Saji et al., 2018), helped to initiate the following El Niño event.

Also, we used a composting technique to study the atmospheric circulation during periods of maximum variability of the EEOF2, which usually occur 12 months before the mature phase of the El Niño events selected. As a result, the circulation exhibited the migration of enhanced convection from the Warm Pool region over the Indian Ocean, which favors the development of anomalous off-equatorial twin cyclones across the Indian Ocean and the low-level converging anomaly above the Indo-Pacific region. Additionally, the eastward propagation of the velocity potential and zonal divergent wind anomalies from the Indian Ocean onto the Western Pacific coincide with the zonal propagation of the westerlies, leading to favorable preconditioning of the onset of the El Niño event (Yamagata and Masumoto, 1990). It was noted that the strongest El Niño events coincide with periods of significant PCs amplitude, which were all followed by a La Niña event the subsequent year. This highlights the role of the interbasin subsurface coupling between the two basins in favoring the ENSO phase transitions and the tendency of El Niño events to be followed by La Niña during the subsequent year (Larkin and Harrison, 2002; Ohba and Ueda, 2009; McPhaden and Zhang, 2009; Okumura and Deser, 2010).

Additionally, we investigate a possible modulation of the intraseasonal wind variability (ISV) by the Indian Ocean, as suggested by previous investigations (Izumo et al., 2010b,a; Wilson et al., 2013; Benedict et al., 2015; Wieners et al., 2016). Furthermore, a significant fraction of the ISV over the tropics is controlled by the Madden-Julian Oscillation (MJO, Madden and Julian, 1971, 1972; Zhang, 2005), thus representing a possible bridge between the two basins. Our results showed an enhancement of the 20-90day OLR longitudinal power distribution over the Warm Pool during the boreal winter and spring season, coinciding

with periods of maximum variability of the EEOF2. This suggests a possible interannual modulation of the ISV mediated by the strong subsurface covariability across the two oceans. Additionally, following the development of a couple of El Niño events, we showed the well documented contribution of the MJO-induced wind ocean waves over the ENSO (Kessler et al., 1995; Hendon et al., 1999; Yu and Rienecker, 1999; McPhaden, 1999; Kessler and Kleeman, 2000; Lengaigne et al., 2002; Zhang, 2005; Zavala-Garay et al., 2005; Hendon et al., 2007; Levine and McPhaden, 2016).

Finally, using a simple conceptual model (Tziperman et al., 1994), we investigate the repercussions of the MJO-induced wind variability over the Western Pacific for the ENSO dynamical behavior. Previously, ENSO's irregularity has been explained by the nonlinear resonant of the intrinsic ENSO's frequency and the seasonal cycle (Tziperman et al., 1994, 1995; Chang et al., 1994; Jiang et al., 1995; Jin et al., 1994, 1996). In Tziperman et al. (1994) 's model, the nonlinear coupling parameter controls the different dynamic regimens. When we included an idealized MJO-forcing parameter to Tziperman et al. (1994) 's model, we observed the quasi-periodicity route to chaos as the increased the ocean-atmosphere coupling parameter, as well as the enhancement of the lower ENSO's frequencies. Furthermore, it was shown that the frequency-locked regimens dominated the parameter space surveyed for the models analyzed in this investigation.

A. Appendix: Complementary Figures

A.1. Leading subsurface interannual variability modes for different temporal filters

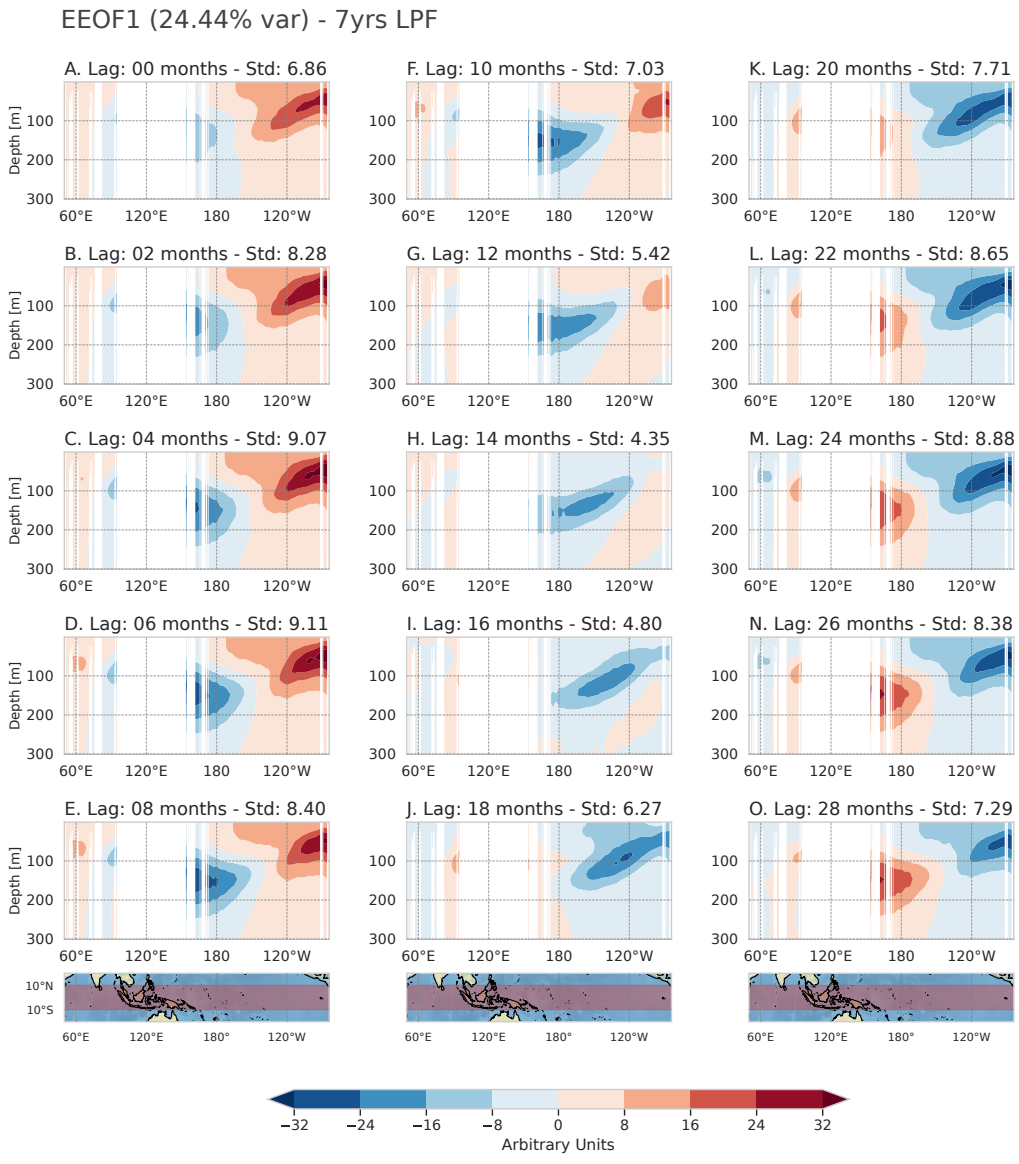

Figure **A-1**.: The spatial pattern of the first mode of the subsurface temperature EEOF from month 0 to month 28 when a 7 years low-pass filter (LPF) was applied. Similar to Figure **2-4** but for a different time filter. Spatial standard deviation (σ_{xy}) of each field is given on the upper-right corner. Dimensionless units.

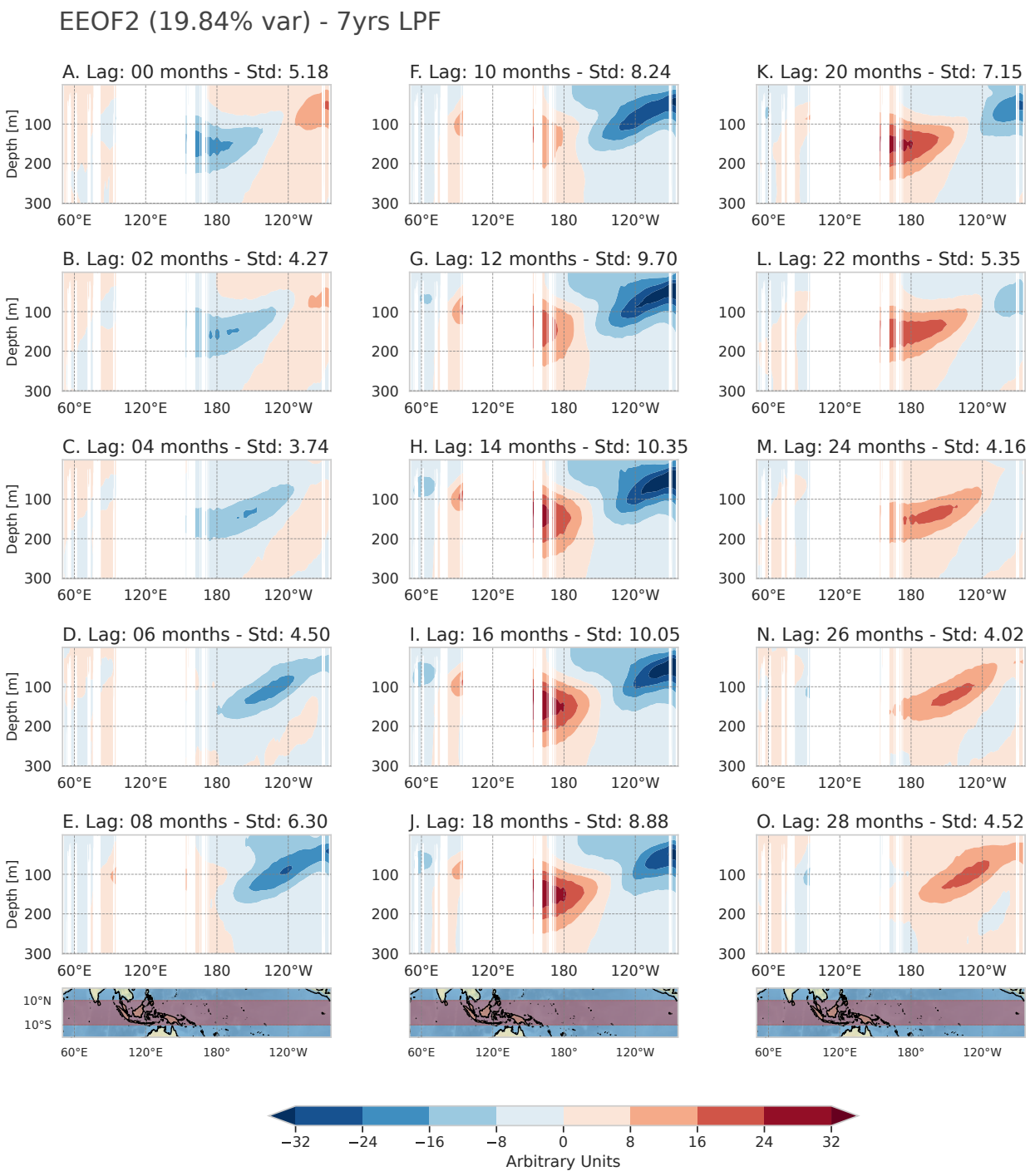

Figure **A-2**.: Similar to Figure **A-1** but for the second mode of the subsurface temperature EEOF when a 7 years low-pass filter (LPF) was applied.

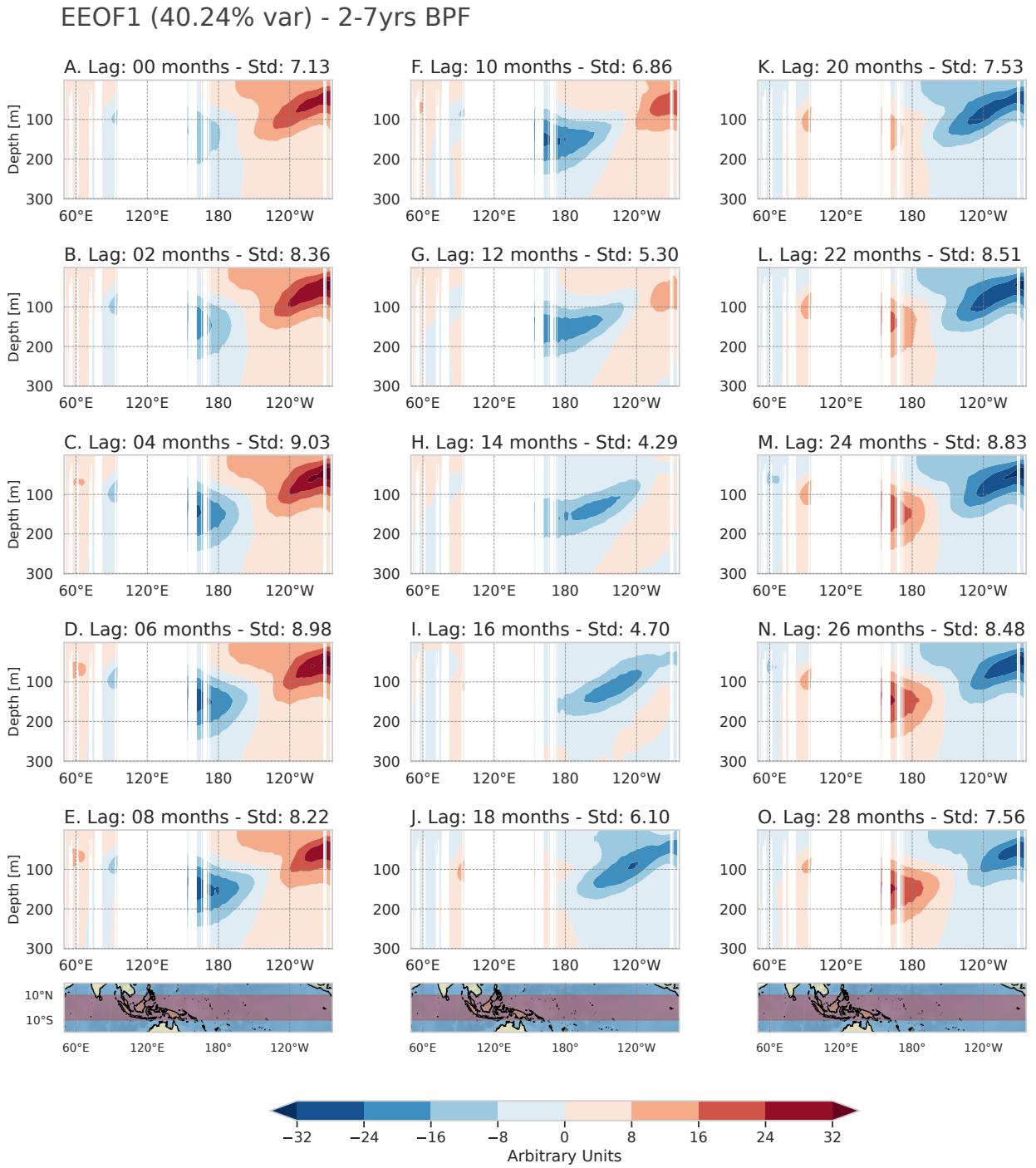

Figure **A-3**.: The spatial pattern of the first mode of the subsurface temperature EEOF from month 0 to month 28 when a 2-7 years band-pass filter (BPF) was applied. Similar to Figure **2-4** but for a different time filter. Spatial standard deviation (σ_{xy}) of each field is given on the upper-right corner. Dimensionless units.

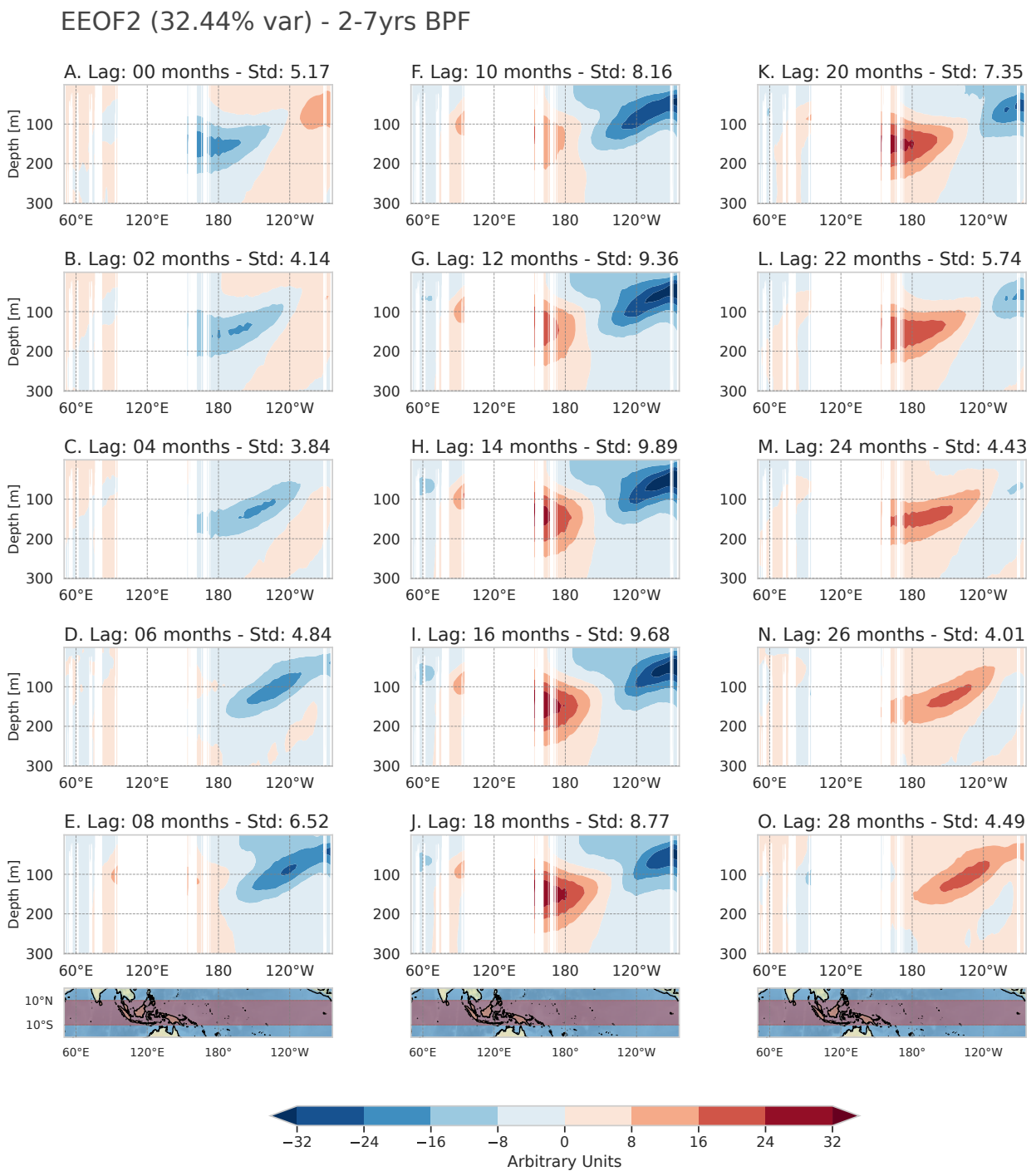

Figure **A-4**.: Similar to Figure **A-3** but for the second mode of the subsurface temperature EEOF when a 2-7 years band-pass filter (BPF) was applied.

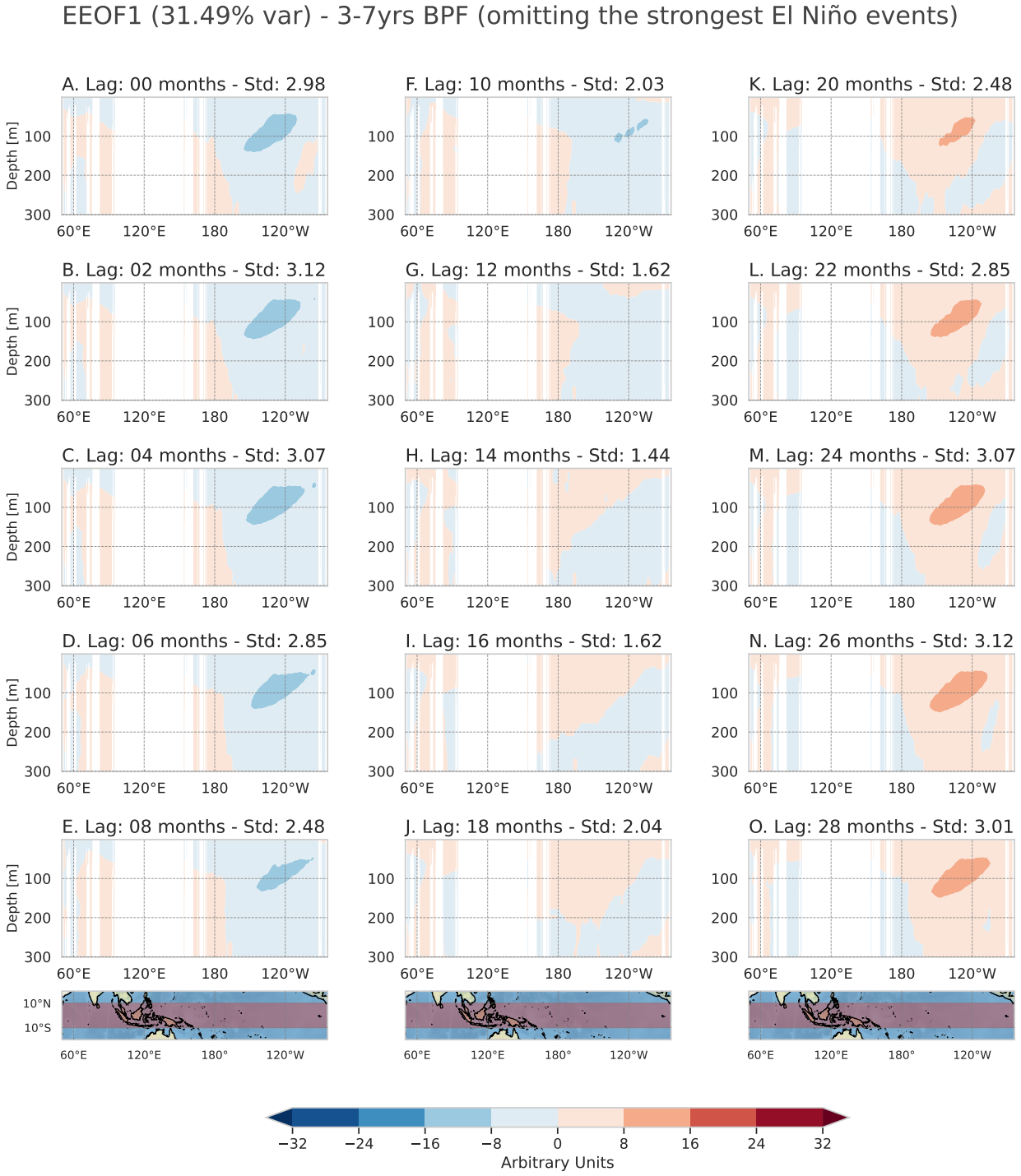

Figure **A-5.**: The spatial pattern of the first mode of the subsurface temperature EEOF from month 0 to month 28 when a 3-7 years band-pass filter (BPF) was applied and the 6 strongest El Niño events were omitted (i.e., 1968-69, 1972-73, 1982-83, 1987-88, 1997-98, and 2015-16). Similar to Figure **2-4**. Spatial standard deviation (σ_{xy}) of each field is given on the upper-right corner. Dimensionless units.

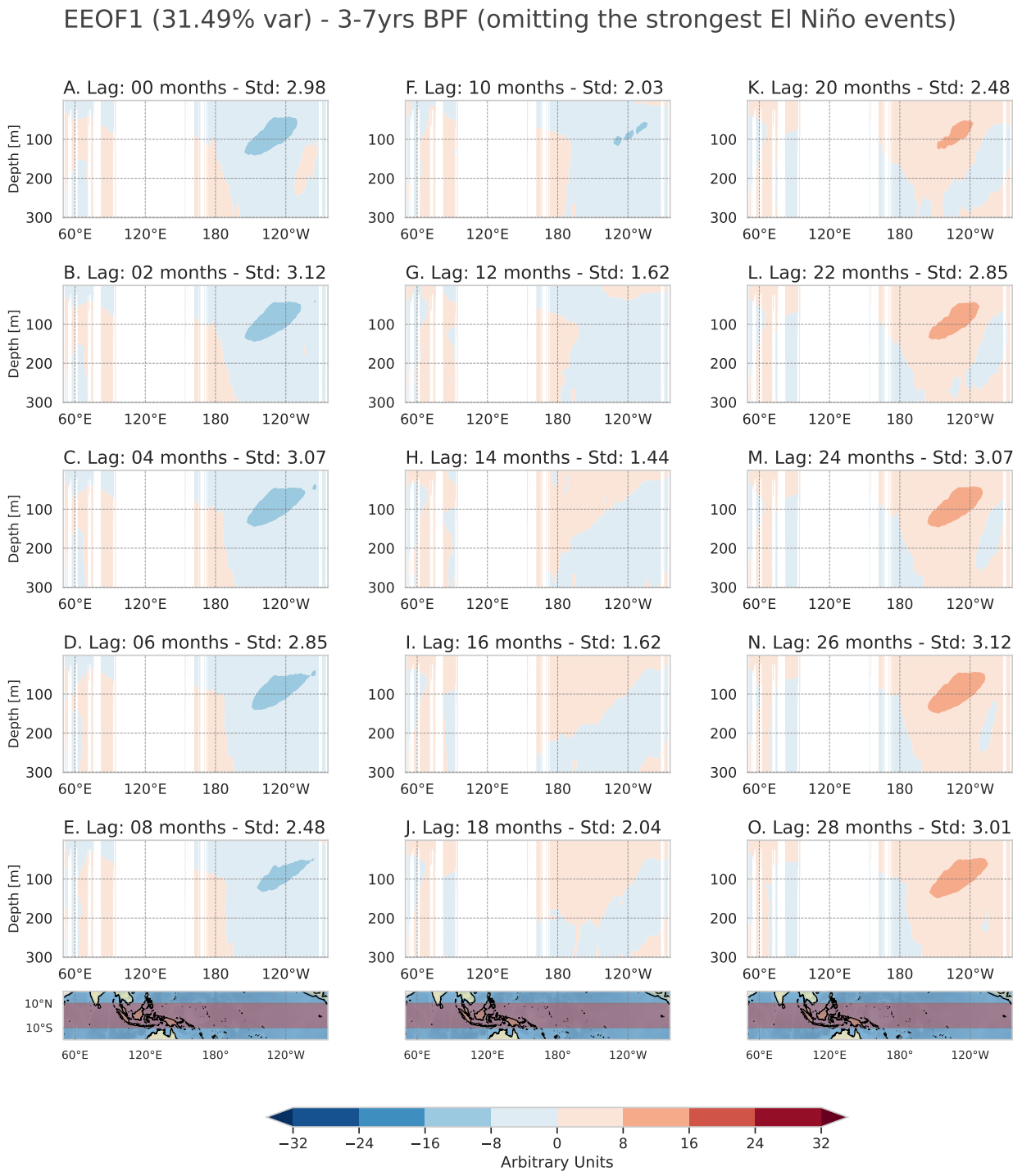

Figure **A-6**.: Similar to Figure **A-5** but for the second mode of the subsurface temperature EEOF when a 3-7 years band-pass filter (BPF) was applied and the 6 strongest El Niño events were omitted (i.e., 1968-69, 1972-73, 1982-83, 1987-88, 1997-98, and 2015-16).

B. Appendix: Complementary Tables

	Short name	Description	Algorithmic definition	Fields	Units
Climatology (light green)	double_ITCZ_bias	Eastern Pacific meridional PR bias ("double ITCZ bias")	RMSE	PR	mm day $^{-1}$
	eq_PR_bias	Equatorial Pacific zonal PR bias	RMSE	PR	mm day $^{-1}$
	eq_SST_bias	Equatorial Pacific zonal SST bias ("cold tongue bias")	RMSE	SST	°C
	eq_Taux_bias	Equatorial Pacific zonal Taux bias	RMSE	Taux	10^{-3} N m^{-2}
	double_ITCZ_sea_cycle	STD of eastern Pacific meridional PR seasonal cycle	RMSE	PR	mm day $^{-1}$
	eq_SST_sea_cycle	STD of equatorial Pacific zonal SST seasonal cycle	RMSE	SST	°C
	eq_Taux_sea_cycle	STD of equatorial Pacific zonal Taux seasonal cycle	RMSE	Taux	10^{-3}N m^{-2}
Basic characteristics (light purple)	ENSO_pattern	NSO pattern: equatorial Pacific zonal SSTA (regression)	RMSE	SST	°C °C^{-1}
	ENSO_life cycle	ENSO life cycle: SSTA evolution in Niño-3.4 (regression)	RMSE	SST	°C °C^{-1}
	ENSO_amplitude	ENSO amplitude: STD of Niño-3.4 SSTA	STD (abs. rel. diff.)	SST	%
	ENSO_seasonality	ENSO seasonal timing: STD of Niño-3.4 SSTA NDJ/MAM	STD (abs. rel. diff.)	SST	%
	ENSO_asymmerty	ENSO asymmetry: Skewness of Niño-3.4 SSTA	SKE (abs. rel. diff.)	SST	%
	ENSO_duration	ENSO event duration: Number of consecutive months with ENSO life cycle >0.25 (Niño-3.4; based on regression)	Number of months (abs. rel. diff.)	SST	%
	ENSO_diversity	ENSO spatial pattern diversity: Interquartile range (IQR) of all EN's (LN's) zonal position of the maximum (minimum) SSTA	IQR (abs. rel. diff.)	SST	%
Telecon. (yellow)	DJF_PR_teleconnection	ENSO PR telecon. pattern in global60 during DJF (based on regression)	RMSE	PR, SST	mm day^{-1} °C^{-1}
	JJA_PR_teleconnection	ENSO PR telecon. pattern in global60 during JJA (based on regression)	RMSE	PR, SST	mm day^{-1} °C^{-1}
	DJF_TS_teleconnection	ENSO TS telecon. pattern in global60 during DJF (based on regression)	RMSE	SST, TS	°C °C^{-1}
	JJA_TS_teleconnection	ENSO TS telecon. pattern in global60 during JJA (based on regression)	RMSE	SST, TS	°C °C^{-1}
Processes (cyan)	SST-Taux_feedback	Atmospheric Bjerknes feedback (Niño-3 SSTA,Niño-4 TauxA)	Slope (abs. rel. diff.)	SST, Taux	%
	Taux-SSH_feedback	Ocean–atmospheric Bjerknes feedback (Niño-4 TauxA, Niño-3 SSHA)	Slope (abs. rel. diff.)	SSH, Taux	%
	SSH-SST_feedback	Oceanic Bjerknes feedback in Niño-3 (SSH, SST)	Slope (abs. rel. diff.)	SSH, SST	%
	SST-NHF_feedback	Total heat flux feedback in Niño-3 (SST, NHF)	Slope (abs. rel. diff.)	SST, NHF	%
	ocean_driven_SST	Ocean-driven SST change in Niño-3 (EN and LN)	dSSToc = dSST - dSSTnhf (abs. rel. diff.)	SST, NHF	%

Table **B-1**.: Description of the CLIVAR 2020 ENSO metrics package, as taken from Planton et al. (2021). "abs. rel. diff." stands for the absolute value of the relative difference, "EN" for El Niño, "LN" La Niña, and "telecon." for teleconnections. Seasons abbreviations MAM, JJA, NDJ, and DJF, correspond to the seasons March-May, June-August, November-January, and December-February, respectively. The fields acronyms correspond to Precipitation (PR), Sea Surface Temperature (SST), Zonal Wind Stress (Taux), Sea Surface Height (SSH), Net heat flux (NHT), and Surface Temperature (TS). A full description of each metric can be found in `https://github.com/CLIVAR-PRP/ENSO_metrics/wiki`.

Bibliography

Achuta Rao, K. and Sperber, K. R. (2006). ENSO simulation in coupled ocean-atmosphere models: Are the current models better? *Climate Dynamics*, 27(1).

Alexander, M. A., Bladé, I., Newman, M., Lanzante, J. R., Lau, N. C., and Scott, J. D. (2002). The atmospheric bridge: The influence of ENSO teleconnections on air-sea interaction over the global oceans. *Journal of Climate*, 15(16):2205–2231.

An, S. I. and Kim, J. W. (2018). ENSO Transition Asymmetry: Internal and External Causes and Intermodel Diversity. *Geophysical Research Letters*, 45(10):5095–5104.

Annamalai, H., Kida, S., and Hafner, J. (2010). Potential Impact of the Tropical Indian Ocean–Indonesian Seas on El Niño Characteristics*. *Journal of Climate*, 23(14):3933–3952.

Annamalai, H., Murtugudde, R., Potemra, J., Xie, S. P., Liu, P., and Wang, B. (2003). Coupled dynamics over the Indian Ocean: Spring initiation of the Zonal Mode. *Deep-Sea Research Part II: Topical Studies in Oceanography*, 50(12-13):2305–2330.

Annamalai, H., Xie, S. P., McCreary, J. P., and Murtugudde, R. (2005). Impact of Indian Ocean Sea Surface Temperature on Developing El Niño*. *Journal of Climate*, 18(2):302–319.

Ashok, K., Guan, Z., and Yamagata, T. (2003). A look at the relationship between the ENSO and the Indian Ocean Dipole. *Journal of the Meteorological Society of Japan*, 81(1):41–56.

Bak, P. (1986). The Devil's staircase. *Physics Today*, 39(12):38–45.

Baquero-Bernal, A., Latif, M., and Legutke, S. (2002). On Dipolelike Variability of Sea Surface Temperature in the Tropical Indian Ocean. *Journal of Climate*, 15(11):1358–1368.

Barnston, A. G., Tippett, M. K., L'Heureux, M. L., Li, S., and Dewitt, D. G. (2012). Skill of real-time seasonal ENSO model predictions during 2002-11: Is our capability increasing? *Bulletin of the American Meteorological Society*, 93(5):631–651.

Battisti, D. S. and Hirst, A. C. (1989). Interannual variability in a tropical atmosphere-ocean model: influence of the basic state, ocean geometry and nonlinearity. *Journal of the Atmospheric Sciences*, 46(12):1687–1712.

Behera, S. K., Luo, J. J., Masson, S., Rao, S. A., Sakuma, H., and Yamagata, T. (2006). A CGCM study on the interaction between IOD and ENSO. *Journal of Climate*, 19(9):1688–1705.

Bellenger, H., Guilyardi, E., Leloup, J., Lengaigne, M., and Vialard, J. (2014). ENSO representation in climate models: From CMIP3 to CMIP5. *Climate Dynamics*, 42(7-8):1999–2018.

Benedict, J. J., Pritchard, M. S., and Collins, W. D. (2015). Sensitivity of MJO propagation to a robust positive Indian Ocean dipole event in the superparameterized CAM. *Journal of Advances in Modeling Earth Systems*, 7(4):1901–1917.

Bjerknes, J. (1969). Atmospheric Teleconnections from the Equatorial Pacific. *Monthly Weather Review*, 97(3):163–172.

Blanke, B., Neelin, J. D., and Gutzler, D. (1997). Estimating the effect of stochastic wind stress forcing on ENSO irregularity. *Journal of Climate*, 10(7):1473–1486.

Bohr, T., Bak, P., and Jensen, M. H. (1984). Transition to chaos by interaction of resonances in dissipative systems. II. Josephson junctions, charge-density waves, and standard maps. *Physical Review A*, 30(4):1970–1981.

Boucher, O., Denvil, S., Levavasseur, G., Cozic, A., Caubel, A., Foujols, M.-A., Meurdesoif, Y., Balkanski, Y., Checa-Garcia, R., Hauglustaine, D., Bekki, S., and Marchand, M. (2020). IPSL IPSL-CM5A2-INCA model output prepared for CMIP6 CMIP historical.

Boucher, O., Denvil, S., Levavasseur, G., Cozic, A., Caubel, A., Foujols, M.-A., Meurdesoif, Y., Balkanski, Y., Checa-Garcia, R., Hauglustaine, D., Bekki, S., and Marchand, M. (2021). IPSL IPSL-CM6A-LR-INCA model output prepared for CMIP6 CMIP historical.

Boucher, O., Denvil, S., Levavasseur, G., Cozic, A., Caubel, A., Foujols, M.-A., Meurdesoif, Y., Cadule, P., Devilliers, M., Ghattas, J., Lebas, N., Lurton, T., Mellul, L., Musat, I., Mignot, J., and Cheruy, F. (2018). IPSL IPSL-CM6A-LR model output prepared for CMIP6 CMIP historical.

Boulanger, J. P., Menkes, C., and Lengaigne, M. (2004). Role of high- and low-frequency winds and wave reflection in the onset, growth and termination of the 1997-1998 El Niño. *Climate Dynamics*, 22(2-3):267–280.

Bracco, A., Kucharski, F., Molteni, F., Hazeleger, W., and Severijns, C. (2005). Internal and forced modes of variability in the Indian Ocean. *Geophysical Research Letters*, 32(12):1–4.

Brown, J. R., Brierley, C. M., An, S. I., Guarino, M. V., Stevenson, S., Williams, C. J., Zhang, Q., Zhao, A., Abe-Ouchi, A., Braconnot, P., Brady, E. C., Chandan, D.,

D'Agostino, R., Guo, C., Legrande, A. N., Lohmann, G., Morozova, P. A., Ohgaito, R., O'Ishi, R., Otto-Bliesner, B. L., Richard Peltier, W., Shi, X., Sime, L., Volodin, E. M., Zhang, Z., and Zheng, W. (2020). Comparison of past and future simulations of ENSO in CMIP5/PMIP3 and CMIP6/PMIP4 models. *Climate of the Past*, 16(5).

Cai, W., Wu, L., Lengaigne, M., Li, T., McGregor, S., Kug, J.-S., Yu, J.-Y., Stuecker, M. F., Santoso, A., Li, X., Ham, Y.-G., Chikamoto, Y., Ng, B., McPhaden, M. J., Du, Y., Dommenget, D., Jia, F., Kajtar, J. B., Keenlyside, N., Lin, X., Luo, J.-J., Martín-Rey, M., Ruprich-Robert, Y., Wang, G., Xie, S.-P., Yang, Y., Kang, S. M., Choi, J.-Y., Gan, B., Kim, G.-I., Kim, C.-E., Kim, S., Kim, J.-H., and Chang, P. (2019). Pantropical climate interactions. *Science (New York, N.Y.)*, 363(6430):eaav4236.

Cane, M. A. and Patton, R. J. (1984). A Numerical Model for Low-Frequency Equatorial Dynamics. *Journal of Physical Oceanography*, 14(12):1853–1863.

Cane, M. A. and Zebiak, S. E. (1985). A theory for El Niño and the Southern Oscillation. *Science*, 228(4703):1085–1087.

Cane, M. A., Zebiak, S. E., and Dolan, S. C. (1986). Experimental forecasts of El Niño. *Nature*, 321(6073):827–832.

Cao, J. and Wang, B. (2019). NUIST NESMv3 model output prepared for CMIP6 CMIP historical.

Capotondi, A., Wittenberg, A. T., Newman, M., Di Lorenzo, E., Yu, J. Y., Braconnot, P., Cole, J., Dewitte, B., Giese, B., Guilyardi, E., Jin, F. F., Karnauskas, K., Kirtman, B., Lee, T., Schneider, N., Xue, Y., and Yeh, S. W. (2015). Understanding enso diversity. *Bulletin of the American Meteorological Society*, 96(6):921–938.

Cashin, P., Mohaddes, K., and Raissi, M. (2017). Fair weather or foul? The macroeconomic effects of El Niño. *Journal of International Economics*, 106.

Chai, Z. (2020). CAS CAS-ESM1.0 model output prepared for CMIP6 CMIP historical.

Chang, P., Ji, L., Li, H., and Flügel, M. (1996). Chaotic dynamics versus stochastic processes in El Niño-Southern Oscillation in coupled ocean-atmosphere models. *Physica D: Nonlinear Phenomena*, 98(2-4):301–320.

Chang, P., Wang, B., Li, T., and Ji, L. (1994). Interactions between the seasonal cycle and the Southern Oscillation - Frequency entrainment and chaos in a coupled ocean-atmosphere model. *Geophysical Research Letters*, 21(25).

Changnon, S. A. (2000). *El Niño 1997-1998: the climate event of the century*. Oxford University Press.

Chekroun, M. D., Ghil, M., and Neelin, J. D. (2018). *Pullback Attractor Crisis in a Delay Differential ENSO Model*, pages 1–33. Springer International Publishing, Cham.

Chen, S., Wu, R., Chen, W., Yu, B., and Cao, X. (2016). Genesis of westerly wind bursts over the equatorial western Pacific during the onset of the strong 2015–2016 El Niño. *Atmospheric Science Letters*, 17(7):384–391.

Chiodi, A. M., Harrison, D. E., and Vecchi, G. A. (2014). Subseasonal atmospheric variability and El Niño waveguide warming: Observed effects of the Madden-Julian oscillation and westerly wind events. *Journal of Climate*, 27(10):3619–3642.

Chowdary, J. S., Gnanaseelan, C., Vaid, B. H., and Salvekar, P. S. (2006). Changing trends in the tropical Indian Ocean SST during La Niña years. *Geophysical Research Letters*, 33(18).

Clarke, A. J. (1991). On the reflection and transmission of low-frequency energy at the irregular western Pacific Ocean boundary. *Journal of Geophysical Research*, 96(S01):3289.

Clarke, A. J. (2008). *An introduction to the dynamics of El Niño and the Southern Oscillation*. Elsevier.

Clarke, A. J. and Van Gorder, S. (2003). Improving El Niño prediction using a space-time integration of Indo-Pacific winds and equatorial Pacific upper ocean heat content. *Geophysical Research Letters*, 30(7).

Danabasoglu, G. (2019a). NCAR CESM2-FV2 model output prepared for CMIP6 CMIP historical.

Danabasoglu, G. (2019b). NCAR CESM2 model output prepared for CMIP6 CMIP historical.

Danabasoglu, G. (2019c). NCAR CESM2-WACCM-FV2 model output prepared for CMIP6 CMIP historical.

Danabasoglu, G. (2019d). NCAR CESM2-WACCM model output prepared for CMIP6 CMIP historical.

Danek, C., Shi, X., Stepanek, C., Yang, H., Barbi, D., Hegewald, J., and Lohmann, G. (2020). AWI AWI-ESM1.1LR model output prepared for CMIP6 CMIP historical.

Ding, H., Keenlyside, N. S., and Latif, M. (2012). Impact of the Equatorial Atlantic on the El Niño Southern Oscillation. *Climate Dynamics*, 38(9-10):1965–1972.

Dix, M., Bi, D., Dobrohotoff, P., Fiedler, R., Harman, I., Law, R., Mackallah, C., Marsland, S., O'Farrell, S., Rashid, H., Srbinovsky, J., Sullivan, A., Trenham, C., Vohralik, P., Watterson, I., Williams, G., Woodhouse, M., Bodman, R., Dias, F. B., Domingues, C., Hannah, N., Heerdegen, A., Savita, A., Wales, S., Allen, C., Druken, K., Evans, B., Richards, C., Ridzwan, S. M., Roberts, D., Smillie, J., Snow, K., Ward, M., and Yang, R. (2019). CSIRO-ARCCSS ACCESS-CM2 model output prepared for CMIP6 CMIP historical.

Dommenget, D., Semenov, V., and Latif, M. (2006). Impacts of the tropical Indian and Atlantic Oceans on ENSO. *Geophysical Research Letters*, 33(11).

Dong, L. and McPhaden, M. J. (2017). Why has the relationship between Indian and Pacific Ocean decadal variability changed in recent decades? *Journal of Climate*, 30(6):1971–1983.

EC-Earth, E.-E. C. (2019a). EC-Earth-Consortium EC-Earth3 model output prepared for CMIP6 CMIP historical.

EC-Earth, E.-E. C. (2019b). EC-Earth-Consortium EC-Earth3-Veg model output prepared for CMIP6 CMIP historical.

EC-Earth, E.-E. C. (2020a). EC-Earth-Consortium EC-Earth3-AerChem model output prepared for CMIP6 CMIP historical.

EC-Earth, E.-E. C. (2020b). EC-Earth-Consortium EC-Earth3-Veg-LR model output prepared for CMIP6 CMIP historical.

EC-Earth, E.-E. C. (2021). EC-Earth-Consortium EC-Earth-3-CC model output prepared for CMIP6 CMIP historical.

Eckert, C. and Latif, M. (1997). Predictability of a stochastically forced hybrid coupled model of El Niño. *Journal of Climate*, 10(7):1488–1504.

Eisenman, I., Yu, L., and Tziperman, E. (2005). Westerly wind bursts: ENSO's tail rather than the dog? *Journal of Climate*, 18(24):5224–5238.

Eyring, V., Bony, S., Meehl, G. A., Senior, C. A., Stevens, B., Stouffer, R. J., and Taylor, K. E. (2016). Overview of the Coupled Model Intercomparison Project Phase 6 (CMIP6) experimental design and organization. *Geoscientific Model Development*, 9(5):1937–1958.

Fasullo, J. T. (2020). Evaluating simulated climate patterns from the CMIP archives using satellite and reanalysis datasets using the Climate Model Assessment Tool (CMATv1). *Geoscientific Model Development*, 13(8):3627–3642.

Fasullo, J. T., Phillips, A. S., and Deser, C. (2020). Evaluation of Leading Modes of Climate Variability in the CMIP Archives. *Journal of Climate*, 33(13):5527–5545.

Fei-Fei Jin and Neelin, J. D. (1993). Modes of interannual tropical ocean-atmosphere interaction - a unified view. Part III: analytical results in fully coupled cases. *Journal of the Atmospheric Sciences*, 50(21):3523–3540.

Feng, M. and Meyers, G. (2003). Interannual variability in the tropical Indian Ocean: A two-year time-scale of Indian Ocean Dipole. *Deep-Sea Research Part II: Topical Studies in Oceanography*, 50(12-13):2263–2284.

Feng, M., Meyers, G., and Wijffels, S. (2001). Interannual upper ocean variability in the tropical Indian Ocean. *Geophysical Research Letters*, 28(21):4151–4154.

Fischer, A. S., Terray, P., Guilyardi, E., Gualdi, S., and Delecluse, P. (2005). Two Independent Triggers for the Indian Ocean Dipole/Zonal Mode in a Coupled GCM. *Journal of Climate*, 18(17):3428–3449.

Flato, G., Marotzke, J., Abiodun, B., Braconnot, P., Chou, S. C., Collins, W., Cox, P., Driouech, F., Emori, S., Eyring, V., and Others (2013). Climate change 2013: the physical science basis. contribution of working group i to the fifth assessment report of the intergovernmental panel on climate change. *Evaluation of Climate Models, eds TF Stocker, D. Qin, G.-K. Plattner, M. Tignor, SK Allen, J. Boschung, et al.(Cambridge: Cambridge University Press)*.

Gadgil, S., Joseph, P. V., and Joshi, N. V. (1984). Ocean-atmosphere coupling over monsoon regions. *Nature*, 312(5990).

Garric, G., Parent, L., Greiner, E., Drévillon, M., Hamon, M., Lellouche, J.-M., Régnier, C., Desportes, C., Le Galloudec, O., Bricaud, C., Drillet, Y., Hernandez, F., Le Traon, P.-Y., Garric, G., Parent, L., Greiner, E., Drévillon, M., Hamon, M., Lellouche, J.-M., Régnier, C., Desportes, C., Le Galloudec, O., Bricaud, C., Drillet, Y., Hernandez, F., and Le Traon, P.-Y. (2017). Performance and quality assessment of the global ocean eddy-permitting physical reanalysis GLORYS2V4. *Eguga*, page 18776.

Gebbie, G., Eisenman, I., Wittenberg, A., and Tziperman, E. (2007). Modulation of westerly wind bursts by sea surface temperature: A semistochastic feedback for ENSO. *Journal of the Atmospheric Sciences*, 64(9):3281–3295.

Godfrey, J. S. (1975). On Ocean Spindown I: A Linear Experiment. *Journal of Physical Oceanography*, 5(3):399–409.

Gualdi, S., Guilyardi, E., Navarra, A., Masina, S., and Delecluse, P. (2003). The interannual variability in the tropical Indian Ocean as simulated by a CGCM. *Climate Dynamics*, 20(6):567–582.

Guilyardi, E., Cai, W., Collins, M., Fedorov, A., Jin, F. F., Kumar, A., Sun, D. Z., and Wittenberg, A. (2012). New strategies for evaluating ENSO process es in climate models. *Bulletin of the American Meteorological Society*, 93(2):235–238.

Guilyardi, E., Capotondi, A., Lengaigne, M., Thual, S., and Wittenberg, A. T. (2020). ENSO Modeling: History, Progress, and Challenges. *El Niño Southern Oscillation in a Changing Climate*, pages 199–226.

Guilyardi, E., Wittenberg, A., Balmaseda, M., Cai, W., Collins, M., McPhaden, M. J., Watanabe, M., and Yeh, S. W. (2016). Fourth clivar workshop on the evaluation of enso processes in climate models: Enso in a changing climate. *Bulletin of the American Meteorological Society*, 97(5).

Guo, H., John, J. G., Blanton, C., McHugh, C., Nikonov, S., Radhakrishnan, A., Rand, K., Zadeh, N. T., Balaji, V., Durachta, J., Dupuis, C., Menzel, R., Robinson, T., Underwood, S., Vahlenkamp, H., Bushuk, M., Dunne, K. A., Dussin, R., Gauthier, P. P. G., Ginoux, P., Griffies, S. M., Hallberg, R., Harrison, M., Hurlin, W., Lin, P., Malyshev, S., Naik, V., Paulot, F., Paynter, D. J., Ploshay, J., Reichl, B. G., Schwarzkopf, D. M., Seman, C. J., Shao, A., Silvers, L., Wyman, B., Yan, X., Zeng, Y., Adcroft, A., Dunne, J. P., Held, I. M., Krasting, J. P., Horowitz, L. W., Milly, P. C. D., Shevliakova, E., Winton, M., Zhao, M., and Zhang, R. (2018). NOAA-GFDL GFDL-CM4 model output historical.

Ha, K. J., Chu, J. E., Lee, J. Y., and Yun, K. S. (2017). Interbasin coupling between the tropical Indian and Pacific Ocean on interannual timescale: observation and CMIP5 reproduction. *Climate Dynamics*, 48(1-2):459–475.

Ham, Y.-G., Choi, J.-Y., and Kug, J.-S. (2017). The weakening of the ENSO–Indian Ocean Dipole (IOD) coupling strength in recent decades. *Climate Dynamics*, 49(1-2):249–261.

Ham, Y. G., Kug, J. S., and Park, J. Y. (2013). Two distinct roles of Atlantic SSTs in ENSO variability: North Tropical Atlantic SST and Atlantic Niño. *Geophysical Research Letters*.

Harrison, D. E. and Larkin, N. K. (1998). El Nino-Southern Oscillation sea surface temperature and wind anomalies, 1946-1993. *Reviews of Geophysics*, 36(3):353–399.

Harrison, D. E. and Schopf, P. S. (1984). Kelvin-wave-induced anomalous advection and the onset of surface warming in El Nino events. *Monthly Weather Review*, 112(5):923–933.

Harrison, D. E. and Vecchi, G. A. (1997). Westerly wind events in the tropical pacific, 1986-95. *Journal of Climate*, 10(12):3131–3156.

Hendon, H. H., Wheeler, M. C., and Zhang, C. (2007). Seasonal dependence of the MJO-ENSO relationship. *Journal of Climate*, 20(3):531–543.

Hendon, H. H., Zhang, C., and Glick, J. D. (1999). Interannual variation of the Madden-Julian oscillation during austral summer. *Journal of Climate*, 12(8 PART 2):2538–2550.

Hersbach, H., Bell, B., Berrisford, P., Biavati, G., Horányi, A., Muñoz Sabater, J., Nicolas, J., Peubey, C., Radu, R., Rozum, I., Schepers, D., Simmons, A., Soci, C., Dee, D., and Thépaut, J.-N. (2019). ERA5 monthly averaged data on single levels from 1979 to present. Copernicus Climate Change Service (C3S) Climate Data Store (CDS).

Hong, C. C., Li, T., LinHo, and Chen, Y. C. (2010). Asymmetry of the Indian Ocean basinwide SST anomalies: Roles of ENSO and IOD. *Journal of Climate*, 23(13).

Horii, T., Hase, H., Ueki, I., and Masumoto, Y. (2008). Oceanic precondition and evolution of the 2006 Indian Ocean dipole. *Geophysical Research Letters*, 35(3).

Hsiang, S. M., Meng, K. C., and Cane, M. A. (2011). Civil conflicts are associated with the global climate. *Nature*, 476(7361):438–441.

Huang, B., Thorne, P. W., Banzon, V. F., Boyer, T., Chepurin, G., Lawrimore, J. H., Menne, M. J., Smith, T. M., Vose, R. S., and Zhang, H. M. (2017). Extended reconstructed Sea surface temperature, Version 5 (ERSSTv5): Upgrades, validations, and intercomparisons. *Journal of Climate*, 30(20):8179–8205.

Huang, W. (2019). THU CIESM model output prepared for CMIP6 CMIP historical.

Inness, P. M., Slingo, J. M., Guilyardi, E., and Cole, J. (2003). Simulation of the Madden-Julian oscillation in a coupled general circulation model. Part II: The role of the basic state. *Journal of Climate*, 16(3):365–382.

Izumo, T., Lengaigne, M., Vialard, J., Luo, J. J., Yamagata, T., and Madec, G. (2014). Influence of Indian Ocean Dipole and Pacific recharge on following year's El Niño: Interdecadal robustness. *Climate Dynamics*, 42(1-2):291–310.

Izumo, T., Masson, S., Vialard, J., de Boyer Montegut, C., Behera, S. K., Madec, G., Takahashi, K., and Yamagata, T. (2010a). Low and high frequency Madden-Julian oscillations in austral summer: Interannual variations. *Climate Dynamics*, 35(4):669–683.

Izumo, T., Vialard, J., Dayan, H., Lengaigne, M., and Suresh, I. (2016). A simple estimation of equatorial Pacific response from windstress to untangle Indian Ocean Dipole and Basin influences on El Niño. *Climate Dynamics*, 46(7-8):2247–2268.

Izumo, T., Vialard, J., Lengaigne, M., de Boyer Montegut, C., Behera, S. K., Luo, J.-J., Cravatte, S., Masson, S., and Yamagata, T. (2010b). Influence of the state of the Indian Ocean Dipole on the following year's El Niño. *Nature Geoscience*, 3(3):168–172.

Jensen, M. H., Bak, P., and Bohr, T. (1984). Transition to chaos by interaction of resonances in dissipative systems. I. Circle maps. *Physical Review A*, 30(4):1960–1969.

Jia, F., Cai, W., Wu, L., Gan, B., Wang, G., Kucharski, F., Chang, P., and Keenlyside, N. (2019). Weakening Atlantic Niño–Pacific connection under greenhouse warming. *Science Advances*, 5(8).

Jiang, N., Neelin, J. D., and Ghil, M. (1995). Quasi-quadrennial and quasi-biennial variability in the equatorial Pacific. *Climate Dynamics*, 12(2):101–112.

Jin, F. F. (1997a). An equatorial ocean recharge paradigm for ENSO. Part I: Conceptual model. *Journal of the Atmospheric Sciences*, 54(7):811–829.

Jin, F. F. (1997b). An equatorial ocean recharge paradigm for ENSO. Part II: A stripped-down coupled model. *Journal of the Atmospheric Sciences*, 54(7):830–847.

Jin, F. F., Lin, L., Timmermann, A., and Zhao, J. (2007). Ensemble-mean dynamics of the ENSO recharge oscillator under state-dependent stochastic forcing. *Geophysical Research Letters*, 34(3).

Jin, F. F., Neelin, J. D., and Ghil, M. (1994). El Niño on the devil's staircase: Annual subharmonic steps to chaos. *Science*, 264(5155):70–72.

Jin, F. F., Neelin, J. D., and Ghil, M. (1996). El Niño/Southern Oscillation and the annual cycle: Subharmonic frequency-locking and aperiodicity. *Physica D: Nonlinear Phenomena*, 98(2-4).

Jourdain, N. C., Lengaigne, M., Vialard, J., Izumo, T., and Gupta, A. S. (2016). Further insights on the influence of the Indian Ocean dipole on the following year's ENSO from observations and CMIP5 models. *Journal of Climate*, 29(2).

Jungclaus, J., Bittner, M., Wieners, K.-H., Wachsmann, F., Schupfner, M., Legutke, S., Giorgetta, M., Reick, C., Gayler, V., Haak, H., de Vrese, P., Raddatz, T., Esch, M., Mauritsen, T., von Storch, J.-S., Behrens, J., Brovkin, V., Claussen, M., Crueger, T., Fast, I., Fiedler, S., Hagemann, S., Hohenegger, C., Jahns, T., Kloster, S., Kinne, S., Lasslop, G., Kornblueh, L., Marotzke, J., Matei, D., Meraner, K., Mikolajewicz, U., Modali, K., Müller, W., Nabel, J., Notz, D., Peters-von Gehlen, K., Pincus, R., Pohlmann, H., Pongratz, J., Rast, S., Schmidt, H., Schnur, R., Schulzweida, U., Six, K., Stevens, B., Voigt, A., and Roeckner, E. (2019). MPI-M MPI-ESM1.2-HR model output prepared for CMIP6 CMIP historical.

Kajtar, J. B., Santoso, A., England, M. H., and Cai, W. (2015). Indo-pacific climate interactions in the absence of an Indonesian throughflow. *Journal of Climate*, 28(13):5017–5029.

Kalnay, E., Kanamitsu, M., Kistler, R., Collins, W., Deaven, D., Gandin, L., Iredell, M., Saha, S., White, G., Woollen, J., Zhu, Y., Chelliah, M., Ebisuzaki, W., Higgins, J., Janowiak, K., Ropelewski, C., Wang, J., Leetmaa, A., Reynolds, R., Jenne, R., and Joseph, D. (1996). 40-Year Reanalysis Project. *Bull. Am. Met. Soc.*, 77(3):437–470.

Keane, A., Krauskopf, B., and Postlethwaite, C. (2016). Investigating irregular behavior in a model for the EI Niño Southern oscillation with positive and negative delayed feedback. *SIAM Journal on Applied Dynamical Systems*, 15(3):1656–1689.

Kessler, W. S. (2002). Is ENSO a cycle or a series of events? *Geophysical Research Letters*, 29(23).

Kessler, W. S. and Kleeman, R. (2000). Rectification of the Madden-Julian Oscillation into the ENSO cycle. *Journal of Climate*, 13(20):3560–3575.

Kessler, W. S., McPhaden, M. J., and Weickmann, K. M. (1995). Forcing of intraseasonal Kelvin waves in the equatorial Pacific. *Journal of Geophysical Research*, 100(C6):10613.

Kirtman, B. P. and Schopf, P. S. (1998). Decadal variability in ENSO predictability and prediction. *Journal of Climate*, 11(11):2804–2822.

Kleeman, R. and Moore, A. M. (1997). A theory for the limitation of ENSO predictability due to stochastic atmospheric transients. *Journal of the Atmospheric Sciences*, 54(6):753–767.

Klein, S. A., Soden, B. J., and Lau, N. C. (1999). Remote sea surface temperature variations during ENSO: Evidence for a tropical atmospheric bridge. *Journal of Climate*, 12(4):917–932.

Krasting, J. P., John, J. G., Blanton, C., McHugh, C., Nikonov, S., Radhakrishnan, A., Rand, K., Zadeh, N. T., Balaji, V., Durachta, J., Dupuis, C., Menzel, R., Robinson, T., Underwood, S., Vahlenkamp, H., Dunne, K. A., Gauthier, P. P. G., Ginoux, P., Griffies, S. M., Hallberg, R., Harrison, M., Hurlin, W., Malyshev, S., Naik, V., Paulot, F., Paynter, D. J., Ploshay, J., Reichl, B. G., Schwarzkopf, D. M., Seman, C. J., Silvers, L., Wyman, B., Zeng, Y., Adcroft, A., Dunne, J. P., Dussin, R., Guo, H., He, J., Held, I. M., Horowitz, L. W., Lin, P., Milly, P. C. D., Shevliakova, E., Stock, C., Winton, M., Wittenberg, A. T., Xie, Y., and Zhao, M. (2018). NOAA-GFDL GFDL-ESM4 model output prepared for CMIP6 CMIP historical.

Krishnaswamy, J., Vaidyanathan, S., Rajagopalan, B., Bonell, M., Sankaran, M., Bhalla, R. S., and Badiger, S. (2015). Non-stationary and non-linear influence of ENSO and Indian Ocean Dipole on the variability of Indian monsoon rainfall and extreme rain events. *Climate Dynamics*, 45(1-2).

Kug, J. S. and Ham, Y. G. (2012). Indian ocean feedback to the ENSO transition in a multimodel ensemble. *Journal of Climate*, 25(20):6942–6957.

Kug, J. S. and Kang, I. S. (2006). Interactive feedback between ENSO and the Indian Ocean. *Journal of Climate*, 19(9):1784–1801.

Kug, J.-S., Kirtman, B. P., Kang, I.-S., Kug, J.-S., Kirtman, B. P., and Kang, I.-S. (2006a). Interactive Feedback between ENSO and the Indian Ocean in an Interactive Ensemble Coupled Model. *Journal of Climate*, 19(24):6371–6381.

Kug, J. S., Li, T., An, S. I., Kang, I. S., Luo, J. J., Masson, S., and Yamagata, T. (2006b). Role of the ENSO-Indian Ocean coupling on ENSO variability in a coupled GCM. *Geophysical Research Letters*, 33(9).

Kug, J.-S., Vialard, J., Ham, Y.-G., Yu, J.-Y., and Lengaigne, M. (2020). ENSO Remote forcing: influence of climate variability outside the tropical Pacific. *El Niño Southern Oscillation in a Changing Climate*, pages 247–265.

Larkin, N. K. and Harrison, D. E. (2002). ENSO warm (El Niño) and cold (La Niña) event life cycles: Ocean surface anomaly patterns, their symmetries, asymmetries, and implications. *Journal of Climate*, 15(10):1118–1140.

Latif, M., Anderson, D., Barnett, T., Cane, M., Kleeman, R., Leetmaa, A., O'Brien, J., Rosati, A., and Schneider, E. (1998). A review of the predictability and prediction of ENSO. *Journal of Geophysical Research: Oceans*, 103(C7).

Latif, M., Barnett, T. P., Cane, M. A., Flügel, M., Graham, N. E., von Storch, H., Xu, J. S., and Zebiak, S. E. (1994). A review of ENSO prediction studies. *Climate Dynamics*, 9(4-5):167–179.

Latif, M., Barnett, T. P., Latif, M., and Barnett, T. P. (1995). Interactions of the Tropical Oceans. *Journal of Climate*, 8(4):952–964.

Lau, N. C. and Nath, M. J. (2000). Impact of ENSO on the variability of the Asian-Australian Monsoons as simulated in GCM experiments. *Journal of Climate*, 13(24):4287–4309.

Lau, N. C. and Nath, M. J. (2003). Atmosphere-ocean variations in the Indo-Pacific sector during ENSO episodes. *Journal of Climate*, 16(1):3–20.

Lee, J., Planton, Y. Y., Gleckler, P. J., Sperber, K. R., Guilyardi, E., Wittenberg, A. T., McPhaden, M. J., and Pallotta, G. (2021). Robust Evaluation of ENSO in Climate Models: How Many Ensemble Members Are Needed? *Geophysical Research Letters*, 48(20).

Lee, W.-L. and Liang, H.-C. (2020). AS-RCEC TaiESM1.0 model output prepared for CMIP6 CMIP historical.

Lellouche, J.-M., Le Galloudec, O., Drévillon, M., Régnier, C., Greiner, E., Garric, G., Ferry, N., Desportes, C., Testut, C.-E., Bricaud, C., Bourdallé-Badie, R., Tranchant, B., Benkiran, M., Drillet, Y., Daudin, A., and De Nicola, C. (2013). Evaluation of global monitoring and forecasting systems at Mercator Océan. *Ocean Science*, 9(1):57–81.

Lengaigne, M., Boulanger, J.-P., Menkes, C., Masson, S., Madec, G., and Delecluse, P. (2002). Ocean response to the March 1997 Westerly Wind Event. *Journal of Geophysical Research: Oceans*, 107(C12):SRF 16–1–SRF 16–20.

Levine, A. F. Z. and McPhaden, M. J. (2016). How the July 2014 easterly wind burst gave the 2015–2016 El Niño a head start. *Geophysical Research Letters*, 43(12):6503–6510.

Li, T., Wang, B., Chang, C. P., and Zhang, Y. (2003). A theory for the Indian Ocean dipole-zonal mode. *Journal of the Atmospheric Sciences*, 60(17).

Liang, Y. and Fedorov, A. V. (2021). Linking the Madden–Julian Oscillation, tropical cyclones and westerly wind bursts as part of El Niño development. *Climate Dynamics*, pages 1–22.

Liebmann, B. (1996). Description of a complete (interpolated) outgoing longwave radiation dataset. *Bulletin of the American Meteorological Society*, 77:1275–1277.

Lorenz, S., Jungclaus, J., Schmidt, H., Haak, H., Reick, C., Schupfner, M., Wachsmann, F., Gayler, V., de Vrese, P., Raddatz, T., Mauritsen, T., von Storch, J.-S., Brovkin, V., Claussen, M., Crueger, T., Fiedler, S., Hagemann, S., Hohenegger, C., Jahns, T., Kinne, S., Kornblueh, L., Marotzke, J., Mikolajewicz, U., Modali, K., Müller, W., Nabel, J., Notz, D., Pincus, R., Pohlmann, H., Rast, S., Schnur, R., Schulzweida, U., Six, K., Stevens, B., Roeckner, E., Wieners, K.-H., Esch, M., Giorgetta, M., and Ilyina, T. (2021). MPI-M ICON-ESM-LR model output prepared for CMIP6 CMIP historical.

Losada, T., Rodríguez-Fonseca, B., Polo, I., Janicot, S., Gervois, S., Chauvin, F., and Ruti, P. (2010). Tropical response to the Atlantic Equatorial mode: AGCM multimodel approach. *Climate Dynamics*, 35(1):45–52.

Lovato, T. and Peano, D. (2020). CMCC CMCC-CM2-SR5 model output prepared for CMIP6 CMIP historical.

Lovato, T., Peano, D., and Butenschön, M. (2021). CMCC CMCC-ESM2 model output prepared for CMIP6 CMIP historical.

Luo, J. J., Behera, S., Masumoto, Y., Sakuma, H., and Yamagata, T. (2008). Successful prediction of the consecutive IOD in 2006 and 2007. *Geophysical Research Letters*, 35(14):L14S02.

Luo, J. J., Zhang, R., Behera, S. K., Masumoto, Y., Jin, F. F., Lukas, R., and Yamagata, T. (2010). Interaction between El Niño and extreme Indian Ocean dipole. *Journal of Climate*, 23(3):726–742.

Madden, R. A. and Julian, P. R. (1971). Detection of a 40–50 Day Oscillation in the Zonal Wind in the Tropical Pacific. *Journal of the Atmospheric Sciences*, 28(5).

Madden, R. A. and Julian, P. R. (1972). Description of Global-Scale Circulation Cells in the Tropics with a 40–50 Day Period. *Journal of the Atmospheric Sciences*, 29(6).

Martín-Rey, M., Polo, I., Rodríguez-Fonseca, B., and Kucharski, F. (2012). Cambios en la Variabilidad Interanual del Pacífico Tropical Como Respuesta a un Forzamiento del Atlántico Ecuatorial. *Scientia Marina*, 76(SUPPL.1):105–116.

Martín-Rey, M., Rodríguez-Fonseca, B., Polo, I., and Kucharski, F. (2014). On the Atlantic–Pacific Niños connection: a multidecadal modulated mode. *Climate Dynamics*, 43(11):3163–3178.

McCreary, J. (1976). Eastern Tropical Ocean Response to Changing Wind Systems: with Application to El Niño. *Journal of Physical Oceanography*, 6(5):632–645.

McPhaden, M. J. (1992). The response of the western equatorial Pacific Ocean to westerly wind bursts during November 1989 to January 1990. *Journal of Geophysical Research*, 97(C9).

McPhaden, M. J. (1999). Genesis and evolution of the 1997-98 El Niño.

McPhaden, M. J. (2004). Evolution of the 2002/03 El Niño. *Bulletin of the American Meteorological Society*, 85(5):677–695.

McPhaden, M. J., Freitag, H. P., Hayes, S. P., Taft, B. A., Chen, Z., and Wyrtki, K. (1988). The response of the equatorial Pacific Ocean to a westerly wind burst in May 1986. *Journal of Geophysical Research*, 93(C9):10589.

McPhaden, M. J., Zebiak, S. E., and Glantz, M. H. (2006a). ENSO as an integrating concept in earth science.

McPhaden, M. J. and Zhang, X. (2009). Asymmetry in zonal phase propagation of ENSO sea surface temperature anomalies. *Geophysical Research Letters*, 36(13).

McPhaden, M. J., Zhang, X., Hendon, H. H., and Wheeler, M. C. (2006b). Large scale dynamics and MJO forcing of ENSO variability. *Geophysical Research Letters*, 33(16):L16702.

Meinen, C. S. and McPhaden, M. J. (2000). Observations of warm water volume changes in the equatorial Pacific and their relationship to El Nino and La Nina. *Journal of Climate*, 13(20):3551–3559.

Menkes, C. E., Lengaigne, M., Vialard, J., Puy, M., Marchesiello, P., Cravatte, S., and Cambon, G. (2014). About the role of Westerly Wind Events in the possible development of an El Niño in 2014. *Geophysical Research Letters*, 41(18):6476–6483.

Merle, J. (1980). Variabilité thermique annuelle et interannuelle de l'océan Atlantique équatorial Est. L'hypothèse d'un "El Niño" Atlantique. *Oceanologica Acta*, 3(2):209–220.

Meyers, G. (1996). Variation of Indonesian throughflow and the El Niño - Southern Oscillation. *Journal of Geophysical Research C: Oceans*, 101(C5):12255–12263.

Moore, A. M. and Kleeman, R. (1999). Stochastic forcing of ENSO by the intraseasonal oscillation. *Journal of Climate*, 12(5 I):1199–1220.

Munnich, M., Cane, M. A., and Zebiak, S. E. (1991). A study of self-excited oscillations of the tropical ocean- atmosphere system. Part II: nonlinear cases. *Journal of the Atmospheric Sciences*, 48(10):1238–1248.

Murtugudde, R. and Busalacchi, A. J. (1999). Interannual variability of the dynamics and thermodynamics of the tropical Indian Ocean. *Journal of Climate*, 12(8 PART 1):2300–2326.

Murtugudde, R., McCreary, J. P., and Busalacchi, A. J. (2000). Oceanic processes associated with anomalous events in the Indian Ocean with relevance to 1997-1998.

N. H. Saji (2018). The Indian Ocean Dipole. *Oxford Research Encyclopedia of Climate Science*, 1(March):1–35.

NASA/GISS, N. G. I. f. S. S. (2018). NASA-GISS GISS-E2.1G model output prepared for CMIP6 CMIP historical.

Neelin, J. D., Battisti, D. S., Hirst, A. C., Jin, F. F., Wakata, Y., Yamagata, T., and Zebiak, S. E. (1998). ENSO theory. *Journal of Geophysical Research: Oceans*, 103(C7):14261–14290.

Neubauer, D., Ferrachat, S., Siegenthaler-Le Drian, C., Stoll, J., Folini, D. S., Tegen, I., Wieners, K.-H., Mauritsen, T., Stemmler, I., Barthel, S., Bey, I., Daskalakis, N., Heinold, B., Kokkola, H., Partridge, D., Rast, S., Schmidt, H., Schutgens, N., Stanelle, T., Stier, P., Watson-Parris, D., and Lohmann, U. (2019). HAMMOZ-Consortium MPI-ESM1.2-HAM model output prepared for CMIP6 CMIP historical.

Nidheesh, A. G., Lengaigne, M., Vialard, J., Izumo, T., Unnikrishnan, A. S., and Krishnan, R. (2019). Natural decadal sea-level variability in the Indian Ocean: lessons from CMIP models. *Climate Dynamics*, 53(9-10):5653–5673.

Ohba, M. and Ueda, H. (2005). Basin-wide Warming in the Equatorial Indian Ocean Associated with El Nino. *Sola*, 1:89–92.

Ohba, M. and Ueda, H. (2007). An impact of SST anomalies in the Indian Ocean in acceleration of the El Niño to La Niña transition. *Journal of the Meteorological Society of Japan*, 85(3):335–348.

Ohba, M. and Ueda, H. (2009). Role of nonlinear atmospheric response to SST on the asymmetric transition process of ENSO. *Journal of Climate*, 22(1):177–192.

Ohba, M. and Watanabe, M. (2012). Role of the Indo-Pacific interbasin coupling in predicting asymmetric ENSO transition and duration. *Journal of Climate*, 25(9):3321–3335.

Okumura, Y. M. and Deser, C. (2010). Asymmetry in the duration of El Niño and la Niña. *Journal of Climate*, 23(21):5826–5843.

Okumura, Y. M., Ohba, M., Deser, C., and Ueda, H. (2011). A proposed mechanism for the asymmetric duration of El Niño and La Niña. *Journal of Climate*, 24(15):3822–3829.

Park, S. and Shin, J. (2019). SNU SAM0-UNICON model output prepared for CMIP6 CMIP historical.

Parlitz, U. (2016). Estimating lyapunov exponents from time series. *Chaos detection and predictability*, pages 1–34.

Penland, C. and Sardeshmukh, P. D. (1995). The optimal growth of tropical sea surface temperature anomalies. *Journal of Climate*, 8(8):1999–2024.

Picaut, J., Loualalen, M., Menkes, C., Delcroix, T., and McPhaden, M. J. (1996). Mechanism of the zonal displacements of the Pacific warm pool: Implications for ENSO. *Science*, 274(5292):1486–1489.

Picaut, J., Masia, F., and Du Penhoat, Y. (1997). An advective-reflective conceptual model for the oscillatory nature of the ENSO. *Science*, 277(5326):663–666.

Planton, Y. Y., Guilyardi, E., Wittenberg, A. T., Lee, J., Gleckler, P. J., Bayr, T., McGregor, S., McPhaden, M. J., Power, S., Roehrig, R., Vialard, J., and Voldoire, A. (2021). Evaluating Climate Models with the CLIVAR 2020 ENSO Metrics Package. *Bulletin of the American Meteorological Society*, 102(2):E193–E217.

Polo, I., Martin-Rey, M., Rodriguez-Fonseca, B., Kucharski, F., and Mechoso, C. R. (2015). Processes in the Pacific La Niña onset triggered by the Atlantic Niño. *Climate Dynamics*, 44(1-2):115–131.

Puy, M., Vialard, J., Lengaigne, M., and Guilyardi, E. (2016). Modulation of equatorial Pacific westerly/easterly wind events by the Madden–Julian oscillation and convectively-coupled Rossby waves. *Climate Dynamics*, 46(7-8):2155–2178.

Rao, S. A. and Behera, S. K. (2005). Subsurface influence on SST in the tropical Indian Ocean: Structure and interannual variability. *Dynamics of Atmospheres and Oceans*, 39(1-2 SPEC. ISS.):103–135.

Rao, S. A., Behera, S. K., Masumoto, Y., and Yamagata, T. (2002). Interannual subsurface variability in the tropical Indian Ocean with a special emphasis on the Indian Ocean Dipole. *Deep-Sea Research Part II: Topical Studies in Oceanography*, 49(7-8):1549–1572.

Rao, S. A. and Yamagata, T. (2004). Abrupt termination of Indian Ocean dipole events in response to intraseasonal disturbances. *Geophysical Research Letters*, 31(19):L19306.

Rasmusson, E. M. and Carpenter, T. H. (1982). Variations in tropical sea surface temperature and surface wind fields associated with the Southern Oscillation/ El Nino (Pacific) . *Monthly Weather Review*, 110(5):354–384.

Reason, C., Allan, R., Lindesay, J., and Ansell, T. (2000). ENSO and climatic signals across the Indian Ocean Basin in the global context: part I, interannual composite patterns. *International Journal of Climatology*, 20(11):1285–1327.

Rodríguez-Fonseca, B., Polo, I., García-Serrano, J., Losada, T., Mohino, E., Mechoso, C. R., and Kucharski, F. (2009). Are Atlantic Niños enhancing Pacific ENSO events in recent decades? *Geophysical Research Letters*, 36(20).

Rong, X. (2019). CAMS CAMS_CSM1.0 model output prepared for CMIP6 CMIP historical.

Rosenstein, M. T., Collins, J. J., and De Luca, C. J. (1993). A practical method for calculating largest Lyapunov exponents from small data sets. *Physica D: Nonlinear Phenomena*, 65(1-2).

Saji, N. H., Goswami, B. N., Vinayachandran, P. N., and Yamagata, T. (1999). A dipole mode in the tropical Indian ocean. *Nature*, 401(6751):360–363.

Saji, N. H., Jin, D., and Thilakan, V. (2018). A model for super El Niños. *Nature Communications*, 9(1).

Saji, N. H. and Yamagata, T. (2003). Possible impacts of Indian Ocean Dipole mode events on global climate. *Climate Research*, 25(2):151–169.

Salby, M. L. and Hendon, H. H. (1994). Intraseasonal Behavior of Clouds, Temperature, and Motion in the Tropics. *Journal of the Atmospheric Sciences*, 51(15):2207–2224.

Santoso, A., England, M. H., and Cai, W. (2012). Impact of indo-pacific feedback interactions on ENSO dynamics diagnosed using ensemble climate simulations. *Journal of Climate*, 25(21):7743–7763.

Scoccimarro, E., Bellucci, A., and Peano, D. (2020). CMCC CMCC-CM2-HR4 model output prepared for CMIP6 CMIP historical.

Seiki, A., Nagura, M., Hasegawa, T., and Yoneyama, K. (2016). Seasonal onset of the Madden–Julian oscillation and its relation to the Southeastern Indian Ocean cooling. *Journal of the Meteorological Society of Japan*, 93A:139–156.

Seiki, A. and Takayabu, Y. N. (2007). Westerly wind burst and their relationship with intraseasonal variations and ENSO. Part I: Statistics. *Monthly Weather Review*, 135(10):3325–3345.

Semmler, T., Danilov, S., Rackow, T., Sidorenko, D., Barbi, D., Hegewald, J., Sein, D., Wang, Q., and Jung, T. (2018). AWI AWI-CM1.1MR model output prepared for CMIP6 CMIP historical.

Shi, L., Alves, O., Hendon, H. H., Wang, G., and Anderson, D. (2009). The role of stochastic forcing in ensemble forecasts of the 1997/98 El Niño. *Journal of Climate*, 22(10).

Shinoda, T. and Hendon, H. H. (2001). Upper-ocean heat budget in response to the Madden-Julian oscillation in the Western Equatorial Pacific. *Journal of Climate*, 14(21):4147–4165.

Shinoda, T., Hendon, H. H., and Alexander, M. A. (2004). Surface and subsurface dipole variability in the Indian Ocean and its relation with ENSO. *Deep-Sea Research Part I: Oceanographic Research Papers*, 51(5):619–635.

Singh, P., Chowdary, J. S., and Gnanaseelan, C. (2013). Impact of prolonged La Niña events on the Indian Ocean with a special emphasis on southwest Tropical Indian Ocean SST. *Global and Planetary Change*, 100.

Song, Z., Qiao, F., Bao, Y., Shu, Q., Song, Y., and Yang, X. (2019). FIO-QLNM FIO-ESM2.0 model output prepared for CMIP6 CMIP historical.

Stein, K., Schneider, N., Timmermann, A., and Jin, F. F. (2010). Seasonal synchronization of ENSO events in a linear stochastic model. *Journal of Climate*, 23(21).

Stein, K., Timmermann, A., and Schneider, N. (2011). Phase synchronization of the El Niño-Southern Oscillation with the annual cycle. *Physical Review Letters*, 107(12).

Stouffer, R. (2019). UA MCM-UA-1-0 model output prepared for CMIP6 CMIP historical.

Stuecker, M. F., Timmermann, A., Jin, F. F., Chikamoto, Y., Zhang, W., Wittenberg, A. T., Widiasih, E., and Zhao, S. (2017). Revisiting ENSO/Indian Ocean Dipole phase relationships. *Geophysical Research Letters*, 44(5).

Suarez, M. J. and Schopf, P. S. (1988). A delayed action oscillator for ENSO. *Journal of the Atmospheric Sciences*, 45(21):3283–3287.

Swart, N. C., Cole, J. N. S., Kharin, V. V., Lazare, M., Scinocca, J. F., Gillett, N. P., Anstey, J., Arora, V., Christian, J. R., Jiao, Y., Lee, W. G., Majaess, F., Saenko, O. A., Seiler, C., Seinen, C., Shao, A., Solheim, L., von Salzen, K., Yang, D., Winter, B., and Sigmond, M. (2019). CCCma CanESM5 model output prepared for CMIP6 CMIP historical.

Tang, Y., Zhang, R. H., Liu, T., Duan, W., Yang, D., Zheng, F., Ren, H., Lian, T., Gao, C., Chen, D., and Mu, M. (2018). Progress in ENSO prediction and predictability study.

Tatebe, H. and Watanabe, M. (2018). MIROC MIROC6 model output prepared for CMIP6 CMIP historical.

Taylor, K. E. (2001). Summarizing multiple aspects of model performance in a single diagram. *Journal of Geophysical Research: Atmospheres*, 106(D7):7183–7192.

Timmermann, A., An, S. I., Kug, J. S., Jin, F. F., Cai, W., Capotondi, A., Cobb, K., Lengaigne, M., McPhaden, M. J., Stuecker, M. F., Stein, K., Wittenberg, A. T., Yun, K. S., Bayr, T., Chen, H. C., Chikamoto, Y., Dewitte, B., Dommenget, D., Grothe, P., Guilyardi, E., Ham, Y. G., Hayashi, M., Ineson, S., Kang, D., Kim, S., Kim, W. M., Lee, J. Y., Li, T., Luo, J. J., McGregor, S., Planton, Y., Power, S., Rashid, H., Ren, H. L., Santoso, A., Takahashi, K., Todd, A., Wang, G., Wang, G., Xie, R., Yang, W. H., Yeh, S. W., Yoon, J., Zeller, E., and Zhang, X. (2018). El Niño–Southern Oscillation complexity.

Tozuka, T., Luo, J. J., Masson, S., and Yamagata, T. (2007). Decadal modulations of the Indian Ocean dipole in the SINTEX-F1 coupled GCM. *Journal of Climate*, 20(13):2881–2894.

Trenberth, K. E., Branstator, G. W., Karoly, D., Kumar, A., Lau, N.-C., and Ropelewski, C. (1998). Progress during TOGA in understanding and modeling global teleconnections associated with tropical sea surface temperatures. *Journal of Geophysical Research: Oceans*, 103(C7):14291–14324.

Tziperman, E., Cane, M. A., and Zebiak, S. E. (1995). Irregularity and locking to the seasonal cycle in an ENSO prediction model as explained by the quasi-periodicity route to chaos. *Journal of the Atmospheric Sciences*, 52(3):293–306.

Tziperman, E., Stone, L., Cane, M. A., and Jarosh, H. (1994). El Niño chaos: Overlapping of resonances between the seasonal cycle and the pacific ocean-atmosphere oscillator. *Science*, 264(5155):72–74.

Ueda, H. and Matsumoto, J. (2000). A possible triggering process of east-west asymmetric anomalies over the Indian Ocean in relation to 1997/98 El Niño. *Journal of the Meteorological Society of Japan*, 78(6):803–818.

Vecchi, G. A. and Harrison, D. E. (2000). Tropical Pacific sea surface temperature anomalies, El Nino, and equatorial westerly wind events. *Journal of Climate*, 13(11):1814–1830.

Vecchi, G. A. and Wittenberg, A. T. (2010). El Niño and our future climate: Where do we stand? *Wiley Interdisciplinary Reviews: Climate Change*, 1(2):260–270.

Venzke, S., Latif, M., and Villwock, A. (2000). The coupled GCM ECHO-2. Part II: Indian Ocean response to ENSO. *Journal of Climate*, 13(8):1371–1383.

Waliser, D. E. and Graham, N. E. (1993). Convective cloud systems and warm-pool sea surface temperatures: coupled interactions and self-regulation. *Journal of Geophysical Research*, 98(D7).

Wang, B., Wu, R., and Fu, X. (2000). Pacific-East Asian teleconnection: How does ENSO affect East Asian climate? *Journal of Climate*, 13(9):1517–1536.

Wang, C. (2001). A Unified Oscillator Model for the El Nino-Southern oscillation. *Journal of Climate*, 14(1):98–115.

Wang, C. (2006). An overlooked feature of tropical climate: Inter-Pacific-Atlantic variability. *Geophysical Research Letters*, 33(12).

Wang, C. (2018). A review of ENSO theories.

Wang, H., Kumar, A., Murtugudde, R., Narapusetty, B., and Seip, K. L. (2019). Covariations between the Indian Ocean dipole and ENSO: a modeling study. *Climate Dynamics*, 53(9-10):5743–5761.

Wang, W., Chen, M., Kumar, A., and Xue, Y. (2011). How important is intraseasonal surface wind variability to real-time ENSO prediction? *Geophysical Research Letters*, 38(13).

Weare, B. C. and Nasstrom, J. S. (1982). Examples of extended empirical orthogonal function analyses. *Monthly Weather Review*, 110(6):481–485.

Weare, B. C., Navato, A. R., and Newell, R. E. (1976). Empirical Orthogonal Analysis of Pacific Sea Surface Temperatures. *Journal of Physical Oceanography*, 6(5):671–678.

Webster, P. (2020). *Dynamics of The Tropical Atmosphere and Oceans*. John Wiley & Sons.

Webster, P. J. (1995). The annual cycle and the predictability of the tropical coupled ocean-atmosphere system. *Meteorology and Atmospheric Physics*, 56(1-2).

Webster, P. J. and Hoyos, C. D. (2010). Beyond the spring barrier? *Nature Geoscience*, 3(3):152–153.

Webster, P. J., Moore, A. M., Loschnigg, J. P., and Leben, R. R. (1999). Coupled ocean-atmosphere dynamics in the Indian Ocean during 1997-98. *Nature*, 401(6751):356–360.

Webster, P. J. and Yang, S. (1992). Monsoon and ENSO. *Quarterly Journal of the Royal Meteorological Society*, 118:877–926.

Weisberg, R. H. and Wang, C. (1997). A western Pacific oscillator paradigm for the El Niño-Southern Oscillation. *Geophysical Research Letters*.

Wheeler, M. and Kiladis, G. N. (1999). Convectively Coupled Equatorial Waves: Analysis of Clouds and Temperature in the Wavenumber-Frequency Domain. *Journal of the Atmospheric Sciences*, 56(3):374–399.

White, W. B. and Cayan, D. R. (2000). A global El Niño-Southern Oscillation wave in surface temperature and pressure and its interdecadal modulation from 1900 to 1997.

Wieners, C. E., de Ruijter, W. P. M., Ridderinkhof, W., von der Heydt, A. S., and Dijkstra, H. A. (2016). Coherent Tropical Indo-Pacific Interannual Climate Variability. *Journal of Climate*, 29(11):4269–4291.

Wieners, C. E., Dijkstra, H. A., and de Ruijter, W. P. (2017). The influence of atmospheric convection on the interaction between the Indian Ocean and ENSO. *Journal of Climate*, 30(24):10155–10178.

Wieners, K.-H., Giorgetta, M., Jungclaus, J., Reick, C., Esch, M., Bittner, M., Legutke, S., Schupfner, M., Wachsmann, F., Gayler, V., Haak, H., de Vrese, P., Raddatz, T., Mauritsen, T., von Storch, J.-S., Behrens, J., Brovkin, V., Claussen, M., Crueger, T., Fast, I., Fiedler, S., Hagemann, S., Hohenegger, C., Jahns, T., Kloster, S., Kinne, S., Lasslop, G., Kornblueh, L., Marotzke, J., Matei, D., Meraner, K., Mikolajewicz, U., Modali, K., Müller, W., Nabel, J., Notz, D., Peters-von Gehlen, K., Pincus, R., Pohlmann, H., Pongratz, J., Rast, S., Schmidt, H., Schnur, R., Schulzweida, U., Six, K., Stevens, B., Voigt, A., and Roeckner, E. (2019). MPI-M MPI-ESM1.2-LR model output prepared for CMIP6 CMIP historical.

Wilson, E. A., Gordon, A. L., and Kim, D. (2013). Observations of the madden julian oscillation during Indian ocean dipole events. *Journal of Geophysical Research Atmospheres*, 118(6):2588–2599.

Wu, R. and Kirtman, B. P. (2004). Understanding the impacts of the Indian ocean on ENSO variability in a coupled GCM. *Journal of Climate*, 17(20):4019–4031.

Wu, T., Chu, M., Dong, M., Fang, Y., Jie, W., Li, J., Li, W., Liu, Q., Shi, X., Xin, X., Yan, J., Zhang, F., Zhang, J., Zhang, L., and Zhang, Y. (2018). BCC BCC-CSM2MR model output prepared for CMIP6 CMIP historical.

Wyrtki, K. (1975). El Niño—The Dynamic Response of the Equatorial Pacific Oceanto Atmospheric Forcing. *Journal of Physical Oceanography*, 5(4):572–584.

Wyrtki, K. (1985). Water displacements in the Pacific and the genesis of El Nino cycles. *Journal of Geophysical Research*, 90(C4).

Xian, W. U., Okumura, Y. M., and Dinezio, P. N. (2019). What controls the duration of El Niño and La Niña events? *Journal of Climate*, 32(18):5941–5965.

Xie, S. P., Annamalai, H., Schott, F. A., and McCreary, J. P. (2002). Structure and mechanisms of South Indian Ocean climate variability. *Journal of Climate*, 15(8):864–878.

Xie, S. P., Hu, K., Hafner, J., Tokinaga, H., Du, Y., Huang, G., and Sampe, T. (2009). Indian Ocean capacitor effect on Indo-Western pacific climate during the summer following El Niño. *Journal of Climate*, 22(3):730–747.

Xie, S. P., Kosaka, Y., Du, Y., Hu, K., Chowdary, J. S., and Huang, G. (2016). Indo-western Pacific ocean capacitor and coherent climate anomalies in post-ENSO summer: A review. *Advances in Atmospheric Sciences*, 33(4):411–432.

Yamagata, T., Behera, S. K., Luo, J. J., Masson, S., Jury, M. R., and Rao, S. A. (2004). Coupled ocean-atmosphere variability in the tropical Indian ocean. In *Geophysical Monograph Series*, volume 147, pages 189–211. Blackwell Publishing Ltd.

Yamagata, T. and Masumoto, Y. (1990). A simple ocean-atmosphere coupled model for the origin of a warm El Nino Southern Oscillation event. *The dynamics of the coupled atmosphere and ocean. Proc. Royal Society meeting, 1988*, 329(1604):71–82.

Yasunari, T. (1985). Zonally Propagating Modes of the Global East-West Circulation Associated with the Southern Oscillation. *Journal of the Meteorological Society of Japan. Ser. II*, 63(6):1013–1029.

Yeh, S. W., Cai, W., Min, S. K., McPhaden, M. J., Dommenget, D., Dewitte, B., Collins, M., Ashok, K., An, S. I., Yim, B. Y., and Kug, J. S. (2018). ENSO Atmospheric Teleconnections and Their Response to Greenhouse Gas Forcing. *Reviews of Geophysics*, 56(1).

Yu, J. Y. and Lau, K. M. (2005). Contrasting Indian Ocean SST variability with and without ENSO influence: A coupled atmosphere-ocean GCM study. *Meteorology and Atmospheric Physics*, 90(3-4).

Yu, L. and Rienecker, M. M. (1999). Mechanisms for the Indian Ocean warming during the 1997-98 El Niño. *Geophysical Research Letters*, 26(6):735–738.

Yuan, D., Wang, J., Xu, T., Xu, P., Hui, Z., Zhao, X., Luan, Y., Zheng, W., and Yu, Y. (2011). Forcing of the Indian Ocean Dipole on the Interannual Variations of the Tropical Pacific Ocean: Roles of the Indonesian Throughflow. *Journal of Climate*, 24(14):3593–3608.

Yuan, D., Zhou, H., and Zhao, X. (2013). Interannual climate variability over the tropical pacific ocean induced by the indian ocean dipole through the Indonesian Throughflow. *Journal of Climate*, 26(9):2845–2861.

Yuan, Y., Chan, C. L., Zhou, W., and Li, C. (2008a). Decadal and interannual variability of the Indian Ocean Dipole. *Advances in Atmospheric Sciences*, 25(5):856–866.

Yuan, Y., Hui, Y., and Chong-Yin, L. (2014). Possible influences of the tropical indian ocean dipole on the eastward propagation of mjo. *Journal of Tropical Meteorology*, 20(2):173–180.

Yuan, Y., Zhou, W., Yang, H., and Li, C. (2008b). Warming in the northwestern Indian Ocean associated with the El Niño event. *Advances in Atmospheric Sciences*, 25(2).

Yukimoto, S., Koshiro, T., Kawai, H., Oshima, N., Yoshida, K., Urakawa, S., Tsujino, H., Deushi, M., Tanaka, T., Hosaka, M., Yoshimura, H., Shindo, E., Mizuta, R., Ishii, M., Obata, A., and Adachi, Y. (2019). MRI MRI-ESM2.0 model output prepared for CMIP6 CMIP historical.

Zang, X., Fu, L. L., and Wunsch, C. (2002). Observed reflectivity of the western boundary of the equatorial Pacific Ocean. *Journal of Geophysical Research: Oceans*, 107(10).

Zavala-Garay, J., Zhang, C., Moore, A. M., and Kleeman, R. (2005). The linear response of ENSO to the Madden-Julian Oscillation. *Journal of Climate*, 18(13):2441–2459.

Zebiak, S. E. (1985). *Tropical Atmosphere - Ocean Interaction and the El Nino/southern Oscillation Phenomenon.* PhD thesis, MASSACHUSETTS INSTITUTE OF TECHNOLOGY.

Zebiak, S. E. (1989). On the 30–60 Day Oscillation and the Prediction of El Niño. *Journal of Climate*, 2(11):1381–1387.

Zebiak, S. E. (1993). Air-sea interaction in the equatorial Atlantic region. *Journal of Climate*, 6(8):1567–1586.

Zebiak, S. E. and Cane, M. A. (1987). A Model El Niño–Southern Oscillation. *Monthly Weather Review*, 115(10):2262–2278.

Zhang, C. (2005). Madden-Julian Oscillation.

Zhang, C., Dong, M., Gualdi, S., Hendon, H. H., Maloney, E. D., Marshall, A., Sperber, K. R., and Wang, W. (2006). Simulations of the Madden-Julian oscillation in four pairs of coupled and uncoupled global models. *Climate Dynamics*, 27(6):573–592.

Zhang, C. and Gottschalck, J. (2002). SST anomalies of ENSO and the Madden-Julian oscillation in the equatorial Pacific. *Journal of Climate*, 15(17):2429–2445.

Zhang, J., Wu, T., Shi, X., Zhang, F., Li, J., Chu, M., Liu, Q., Yan, J., Ma, Q., and Wei, M. (2018). BCC BCC-ESM1 model output prepared for CMIP6 CMIP historical.

Zhang, W., Wang, Y., Jin, F. F., Stuecker, M. F., and Turner, A. G. (2015). Impact of different El Niño types on the El Niño/IOD relationship. *Geophysical Research Letters*, 42(20):8570–8576.

Zhao, Y. and Nigam, S. (2015). The Indian ocean dipole: A monopole in SST. *Journal of Climate*, 28(1):3–19.

Ziehn, T., Chamberlain, M., Lenton, A., Law, R., Bodman, R., Dix, M., Wang, Y., Dobrohotoff, P., Srbinovsky, J., Stevens, L., Vohralik, P., Mackallah, C., Sullivan, A., O'Farrell, S., and Druken, K. (2019). CSIRO ACCESS-ESM1.5 model output prepared for CMIP6 CMIP historical.

Zuo, H., Balmaseda, M. A., Tietsche, S., Mogensen, K., and Mayer, M. (2019). The ECMWF operational ensemble reanalysis-analysis system for ocean and sea ice: A description of the system and assessment. *Ocean Science*, 15(3):779–808.